Titre: Title:	Stochastic Ice Accretion Model for Aircraft Icing
Auteur: Author:	Hélène Papillon Laroche
Date:	2022
Type:	Mémoire ou thèse / Dissertation or Thesis
Référence: Citation:	Papillon Laroche, H. (2022). Stochastic Ice Accretion Model for Aircraft Icing [Mémoire de maîtrise, Polytechnique Montréal]. PolyPublie. https://publications.polymtl.ca/10277/

POLYTECHNIQUE MONTRÉAL
affiliée à l'Université de Montréal

Stochastic Ice Accretion Model for Aircraft Icing

HÉLÈNE PAPILLON LAROCHE
Département de génie mécanique

Mémoire présenté en vue de l'obtention du diplôme de *Maîtrise ès sciences appliquées*
Génie aérospatial

Avril 2022

POLYTECHNIQUE MONTRÉAL
affiliée à l'Université de Montréal

Ce mémoire intitulé :

Stochastic Ice Accretion Model for Aircraft Icing

présenté par **Hélène PAPILLON LAROCHE**
en vue de l'obtention du diplôme de *Maîtrise ès sciences appliquées*
a été dûment accepté par le jury d'examen constitué de :

Marcelo REGGIO, président
Éric LAURENDEAU, membre et directeur de recherche
David VIDAL, membre

DEDICATION

À Romy.

ACKNOWLEDGEMENTS

I would like to thank my supervisor, Prof. Éric Laurendeau, for his guidance, his humanity, and his understanding. Throughout my project, he was always available to discuss scientific subjects, and he gave just enough insights for me to trace my own path into the research field. I am grateful for the opportunities he provided me and his support in the completion of an internship in Toulouse, France.

I am also very grateful for the welcoming and guidance of Emmanuel Radenac during and after my internship under his supervision at the ONERA in Toulouse. All our scientific discussions were insightful and this international experience was very appreciated.

I would also like to thank Simon Bourgault-Côté for listening to my multiple questions, for his time, and for his feedback. His support was constant and our discussions over coffee and/or waffles were always appreciated. I want to thank also Vincent, Reda, Maxime, and Frédéric for their friendship (and for the waffle Thursdays) in the lab.

I am thankful for the constant support of my family and Olivier throughout my Master's degree, helping me to reach my objectives.

Finally, I want to acknowledge the support of the Natural Sciences and Engineering Research Council of Canada (NSERC) and the Fonds de recherche du Québec Nature et Technologies (FRQNT).

RÉSUMÉ

L'accrétion de glace en vol est un risque important dans le domaine de l'aviation car elle entraîne une dégradation des performances. Ce phénomène est une partie importante des processus de conception et de certification. Il représente un domaine de recherche actif car les mécanismes sous-jacents ne sont pas encore bien compris. Les simulations numériques sont utilisées comme alternatives aux essais expérimentaux, permettant de traiter une variété de conditions de givrage à moindre coût. Les fondements mathématiques des principaux logiciels de givrage, tels que LEWICE3D, IGLOO3D et FENSAP-ICE, sont majoritairement basés sur des méthodes algébriques et des systèmes d'équations différentielles partielles. Le phénomène d'accrétion de la glace est donc représenté du façon continue et déterministe, dans laquelle la densité de la glace est traitée comme une variable indépendante. Cependant, les structures de glace discrètes et aléatoires observées dans les essais expérimentaux, telles que les plumes de glace, qui peuvent mener à des formes de glace significatives et à une dégradation sévère des performances ne sont pas capturées par ces méthodes. De plus, les logiciels à l'état de l'art ne modélisent pas la variabilité observée dans la forme de la glace obtenue pour de multiples essais des mêmes conditions de givrage. Des alternatives aux outils numériques traditionnels ont donc été proposées pour surmonter ces limitations et améliorer la compréhension du phénomène de givrage.

L'objectif principal de ce travail est de fournir un cadre numérique original, bidimensionnel, discret et stochastique pour modéliser le phénomène d'accrétion de glace, basé sur de récents travaux présents dans la littérature. Les développements sont implémentés dans CHAMPS, un logiciel interne de dynamique des fluides numérique.

Tout d'abord, le domaine d'accrétion est discrétisé en utilisant un algorithme d'avance de front non-structuré, habituellement utilisé pour la génération de maillage. La technique est basée sur la création d'éléments de glace à partir de gouttelettes d'eau. Des éléments triangulaires sont générés à mesure que le front de glace avance dans l'espace. Les gouttelettes d'eau sont traitées une par une, et leur trajectoire est extraite du champ de vitesse obtenu à partir d'un solveur de gouttelettes eulérien. Les gouttelettes sont rassemblées en amas pour réduire le coût de calcul, et ces derniers sont injectés à une position initiale aléatoire, sur un plan d'injection, en amont de la géométrie étudiée. La stochasticité est également introduite dans la taille des gouttelettes, en les échantillonnant de manière aléatoire à partir de la distribution expérimentale de taille. Le point d'impact correspond à l'intersection entre la trajectoire des gouttelettes et le front de glace. À partir de là, selon l'état thermodynamique

calculé avec un modèle de Messinger itératif, la goutte peut soit geler au point d'impact, soit former un film d'eau, ruisselant sur la surface selon la direction de l'écoulement d'air à la surface, et geler plus loin en aval. Lors de la congélation, un nouvel élément de glace est créé avec l'algorithme d'avance de front. La méthode développée correspond à un cadre monocouche, c'est-à-dire que l'écoulement d'air, le champ de vitesse des gouttelettes et les échanges thermodynamiques ne sont résolus qu'une seule fois avant la méthode stochastique. Cependant, l'effet de la croissance de la glace sur les trajectoires est pris en compte d'une manière plus fine que dans le cadre multicouche, grâce à la technique d'avance de front et à la représentation discrète de la glace. Cela conduit au traitement de la densité de la glace comme une variable dépendante et à une meilleure représentation des zones d'ombre observées derrière les cornes de glace, par exemple.

Ensuite, la vérification des calculs de la trajectoire des gouttelettes est effectuée en comparant l'efficacité de captation obtenue pour deux cas tests aux résultats déterministes de CHAMPS, montrant un bon accord entre les deux méthodes. De plus, l'effet de la taille de l'élément généré avec l'algorithme d'avance de front sur la densité de la glace est évalué par une étude de convergence en espace, montrant la convergence de la méthode développée en espace.

Finalement, la méthode est validée sur quatre cas tests. Les formes de glace obtenues sont en bon accord avec les résultats expérimentaux. La variabilité dans la forme de la glace est observée pour plusieurs essais du même cas, et des plumes de glace discrètes sont capturées. De plus, des cornes de glace sont modélisées, bien que le cadre soit monocouche.

Pour conclure, la méthode développée conduit à une meilleure modélisation des structures de glace discrètes et variables, ainsi qu'à une représentation plus fine des zones d'ombre, tout en traitant la densité de la glace comme un résultat du processus. Les résultats suggèrent qu'une extension du modèle en trois dimensions est nécessaire pour bien représenter la densité variable de la glace et les mécanismes de givrage sous-jacents. En outre, des simulations multicouches sont nécessaires pour mieux modéliser la croissance de cornes de glace.

ABSTRACT

In-flight ice accretion is a significant hazard in aviation as it leads to performance degradation. The phenomenon is an important part of the design and certification processes and represents an active field of research as the underlying mechanisms are still not well understood. Numerical simulations are used as alternatives to experimental trials, allowing to treat a variety of icing conditions at a lower cost. The mathematical foundations of leading icing software, such as LEWICE3D, IGLOO3D, and FENSAP-ICE, are mainly based on algebraic methods and partial differential equations systems. This leads to a continuous and deterministic representation of the ice accretion phenomenon, in which the ice density is treated as an independent variable. However, discrete and random ice structures observed in experimental frameworks, such as ice feathers, leading to significant ice shapes and severe performance degradation are not captured by these methods. Additionally, state-of-the-art software do not model the variability observed in the ice shape obtained for multiple trials of the same icing conditions. Alternatives to the traditional numerical tools are thus proposed to overcome these limitations and further the understanding of the icing phenomenon.

The main objective of this work is to provide an original two-dimensional, discrete and stochastic numerical framework to model the ice accretion phenomenon, based on recent works of the literature. The developments are implemented in CHAMPS, an in-house computational fluid dynamic software.

First, the accretion domain is discretized using an unstructured advancing front algorithm, usually used for mesh generation. The technique is based on the creation of elements of ice from incoming water droplets. In a building block manner, triangular elements are generated as the ice front advances in space. The water droplets are treated one at a time, and their trajectory is extracted from the velocity field obtained with an Eulerian droplet solver. The droplets are gathered in clusters to reduce the computational cost, and the latter are seeded at random initial positions, on a seeding plane, upstream of the studied geometry. Stochasticity is also introduced in the droplet size, randomly sampling it from the experimental size distribution, using the inverse transform sampling method. The impingement location corresponds to the intersection between the droplet trajectory and the ice front. From there, according to the thermodynamic state computed with an Iterative Messinger model, the droplet can either freeze at the impingement location or form a water film, flowing on the surface according to the direction of the shear stress at the wall, and freeze further downstream. Upon freezing, a new element of ice is created with the unstructured advancing front

algorithm. The developed method corresponds to a single-layer framework, i.e., the airflow, the droplet velocity field, and the thermodynamic exchanges are resolved only once before the stochastic method. However, the effect of the ice growth on the trajectories is taken into account in a finer way than the state-of-the-art multi-layer framework due to the advancing front technique and the discrete representation of the ice. This leads to the treatment of the ice density as a dependent variable and to a better representation of the shadow zones observed, for example, behind ice horns.

Second, the verification of the droplet trajectory computations is performed with the comparison of the obtained collection efficiency for two test cases to the deterministic results of CHAMPS, leading to good agreement between the two methods. Additionally, the effect of the element size generated with the unstructured advancing front algorithm on the ice density is assessed through a space convergence study, showing the space convergence of the implemented method.

Finally, the method is validated against four test cases. The obtained ice shapes are in good agreement with the experimental results. Variability is observed for multiple trials of the same test case in the ice shape, and discrete ice feathers are captured. Furthermore, ice horns are modeled, although the framework is single-layer.

To conclude, the developed method leads to better modeling of the discrete and variable ice feathers, as well as a finer representation of the shadow zones, while treating the ice density as a result of the process. The results suggest that an extension of the model in three dimensions is needed to well capture the variable ice density and underlying icing mechanisms in the spanwise direction. Furthermore, multi-layer simulations are required to better model the growth of ice horns.

TABLE OF CONTENTS

LIST OF TABLES

LIST OF FIGURES

LIST OF SYMBOLS AND ACRONYMS

c	Chord length	m
$\vec{C}_f$	Skin friction coefficient	-
f_{fr}	Freezing fraction	-
k_s	Equivalent sand grain roughness	m
m	Mass	kg
$\dot{m}$	Mass rate	kg/s
$M_{total,ice}$	Total mass of ice	kg
n	Number of surface elements	-
N	Number of volume elements	-
$\vec{n}$	Unit normal vector	-
P	Coordinate point	m
p_{seed}	Seeding plane position on the x-axis	m
$\dot{Q}$	Energy rate	W
T_{fus}	Fusion temperature	K
T_s	Surface temperature	K
u	Uniform random variable	-
$\vec{u}$	Velocity vector	m/s
U	Velocity magnitude	m/s
V	Volume	m^2
x, y, z	Cartesian coordinates	-

Greek Symbols

β	Droplet collection efficiency	-
δ	Element size	m
Δt_{icing}	Icing time	s
Δs_i	Surface element length	m
$\rho_{bulk,ice}$	Bulk ice density	kg/m^3

Subscripts

0	Initial
cluster	Cluster related
cond	Conduction
conv	Convection

d	Droplet
element	Element related
entry	Entry point related
ev,sub	Evaporation/sublimation
exit	Exit point related
f	Friction
facet	Facet
i	Increment
ice	Ice
in	Inflow
inf	Free stream related
imp	Impingement
kin	Kinetic
opt	Optimal
out	Outflow
stoch	Stochastic
rad	Radiation

Acronyms

AoA	Angle of attack
CDF	Cumulative distribution function
CHAMPS	CHApel Multi-Physics Simulation
FAR	Federal Airworthiness Regulations
HTC	Convective heat transfer coefficient
ICI	Ice Crystal Icing
IPW	Ice Prediction Workshop
LE	Leading edge
MVD	Median volume diameter
LWC	Liquid water content
PDE	Partial differential equations
PDF	Probability density function
PRN	Pseudo-random number
RANS	Reynolds Averaged Navier-Stokes
SLD	Supercooled Large Droplets
SSD	Supercooled Standard Droplets
TE	Trailing edge

LIST OF APPENDICES

CHAPTER 1 INTRODUCTION

1.1 Context

Ice accretion, often referred as icing, is a common issue in various engineering applications. Accretion due to the impingement and freezing of supercooled water droplets can be observed on exposed surfaces of aircrafts, helicopters, wind turbines, ships, offshore facilities, and power lines. The accreted ice increases the mass of the systems which can lead to higher fuel consumption and crash for aircrafts, capsizing of ships, and collapse of power lines [8]. This thesis focuses on aircraft applications, although the method developed can be used in other fields.

1.1.1 Effects of Aircraft Icing

Ice accretion on aircraft wings (or rotor blades) leads to changes in the geometry of the airfoil. These changes can affect the aerodynamic performances by decreasing the maximum lift and the stall angle and increasing the drag [4]. Ice can also accumulates on measuring probes, such as the Pitot tube, and leads to a false lecture of the flight instruments, which is a major safety issue [4, 8, 9]. Degradation of the engine performances or its failure are also possible impacts of in-flight ice accretion [9].

The worst-case scenario is when the ice buildup leads to the crash of an aircraft, which can cause fatalities. Since the first reported fatal event due to icing in the 1920s, the icing phenomenon is investigated, and manufacturers are required to certify the capacity of the aircraft to operate in specific icing conditions since 1964 [3]. These conditions are stated in the Federal Airworthiness Regulations (FAR), part 25 Appendix C for Supercooled Standard Droplets (SSD) [10]. Following incidents involving Supercooled Large Droplets (SLD) and Ice Crystal Icing (ICI) [3, 4], regulations have been added to the FAR: part 25 Appendix O for SLD [11] and part 33 for ICI [12].

1.2 Theoretical Framework

Aircraft icing is due to the impingement and freezing of supercooled water droplets, or ice crystals, when an aircraft passes through a cloud of droplets. The airflow carries the droplets and drives the impingement map on the exposed surface. Upon impingement and according to the thermodynamic exchanges at the surface, the droplets can either freeze at their impact

location or form a water film and flow downstream on the substrate. The icing conditions, driving the impact conditions and thermodynamic exchanges, govern how and when the freezing of supercooled water droplets happens [13].

1.2.1 Icing Conditions and Ice Geometries

The different icing conditions result in various ice accretion shapes [8] and lead to various impacts on the degradation of the aerodynamic performances [14]. The different ice morphologies are illustrated in Figure 1.1.

Ice Roughness

At the beginning of the process, before any significant alteration of the airfoil shape, the ice tends to accumulate as an initial surface roughness [14]. The thin rime ice layer is formed of a smooth zone in the stagnation region, which transitions into a rough zone, and ends with an area where ice feathers are observed [3, 14], as shown in Figure 1.1(a). In addition to the increase of skin friction, ice roughness can cause early boundary layer transition [14] and modify the convective heat transfer [15, 16].

It is worth mentioning that after the accumulation of the initial layer of ice, the surface of the ice shape is rough, no matter the type of accretion [14].

Rime Icing Conditions

Streamwise ice is observed at rime icing conditions (Figure 1.1(b)), which occurs at lower temperatures, where the water supercooling is greater. Droplets freeze upon impingement, resulting in an ice shape that initially forms following the geometry shape. Therefore, streamwise ice can be interpreted as an extension of the leading edge (LE) [14], resulting in little effects on the airflow. The rime ice tends to have a lower density due to air trapped in the ice at the droplet impingement [3, 13].

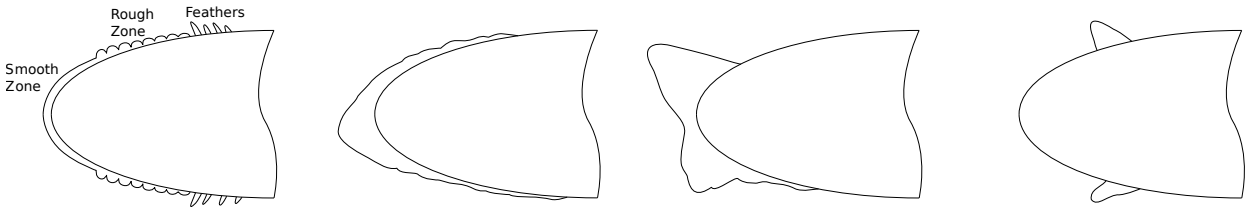

(a) Ice roughness (b) Streamwise ice (c) Horn ice (d) Spanwise-ridged ice

Figure 1.1 Ice geometries

Glaze Icing Conditions

Glaze conditions are characterized by warmer temperatures at which the impinging droplets do not freeze entirely upon impact. The unfrozen water forms a water film, known as runback water, flowing downstream of the stagnation region, driven by the airflow shear stress [3, 4]. Denser ice can form further downstream in complex shapes, such as ice horns (Figure 1.1(c)) and spanwise ridges (Figure 1.1(d)), resulting in larger separation regions and performance degradations [14].

Mixed Ice Conditions

The observed ice geometries often feature different types of ice, mainly due to the local variations in the flow field [13]. Therefore, a combination of rime and glaze ice shapes can be observed on the same exposed surface.

Discrete Ice Structures

Ice feathers Ice structures known as ice feathers, shown in Figure 1.2, can grow at discrete locations, away from the main ice accretion, or be part of the latter, depending on the icing conditions. In the early stages of their formation, the feathers grow as individual elements from small surface roughness. Later on, they can lead to the formation of horns, ridges, or scallops, especially for SLD conditions [2, 17]. The mechanisms behind the growth of ice feathers, and their development into significant ice structures are yet to be understood [17].

Ice Scallops Accretion on swept wings can lead to the formation of highly 3D structures referred to as scallops or lobster tails [18], mainly in glaze icing conditions. They are formed from glaze ice feathers [2, 19]. Scallops are complex, discontinuous, and periodic, and lead to large voids within the ice accretion [19, 20]. Furthermore, taking into account their highly 3D characteristics, the perturbations of the scallops on the flow are significant [3].

1.2.2 Stochasticity of the Ice Geometries

The ice accretion is random by nature [17]. Indeed, the ice geometries obtained in experimental setups are highly variable [3, 6]. Case 242, presented at the 1st Ice Prediction Workshop (IPW) [1], illustrates well this variability. As presented in Figure 1.3(a), at the same icing conditions, several experimental trials lead to different ice shapes. Additionally, within the same trial, the ice shape can vary in the spanwise direction (Figure 1.3(b)), even for pseudo-2D cases, which are tested on full 3D wings with spanwise invariant geometries. Symmetrical

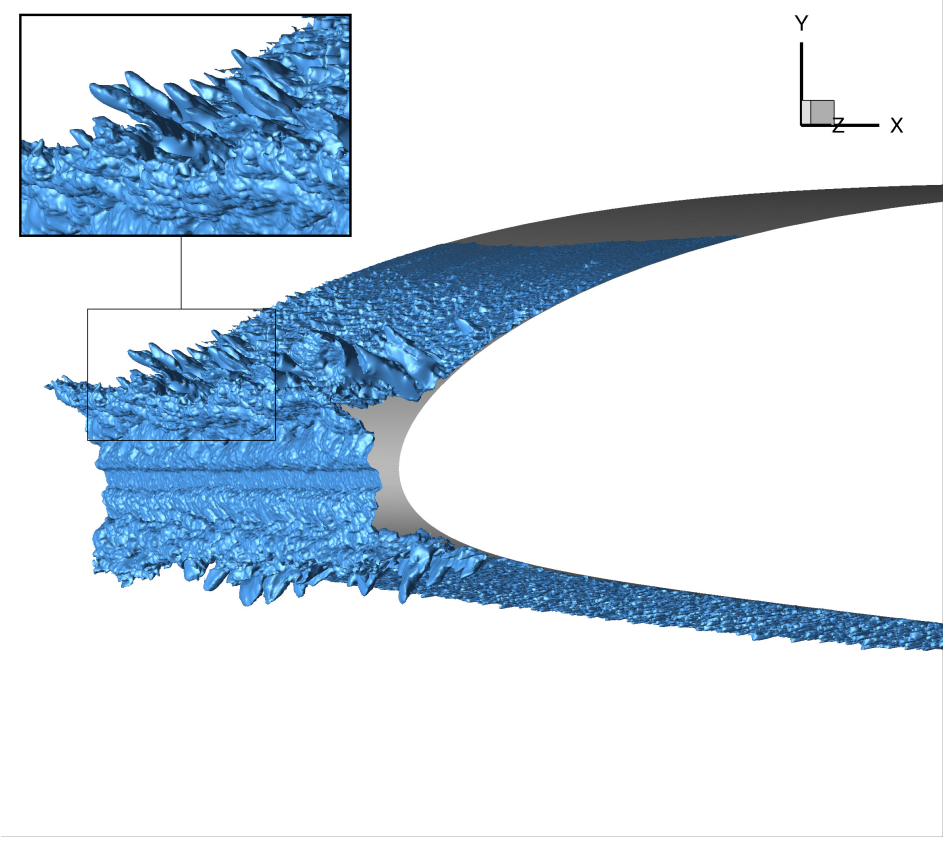

Figure 1.2 Scan of the ice shape for case 251 [1]

airfoils at 0° of angle of attack (AOA) also present differences in the ice shapes of the upper and lower surfaces, and the variability is similar to the one occurring in multiple experimental trials for the same icing conditions [17].

Furthermore, roughness elements and feathers appear at random positions [17]. Figure 1.2 presents the scan of the experimental ice shape obtained for case 251 of the IPW [1]. Feathers, highlighted in the zoom of Figure 1.2, are observed at different locations and their size varies randomly.

A common way to represent the experimental ice shape variations in the spanwise direction is the extraction of the maximum combined cross section (MCCS) [1]. This process consists of identifying the outer-most ice contour obtained from the combinations of multiple cuts of the experimental ice scan in the spanwise direction.

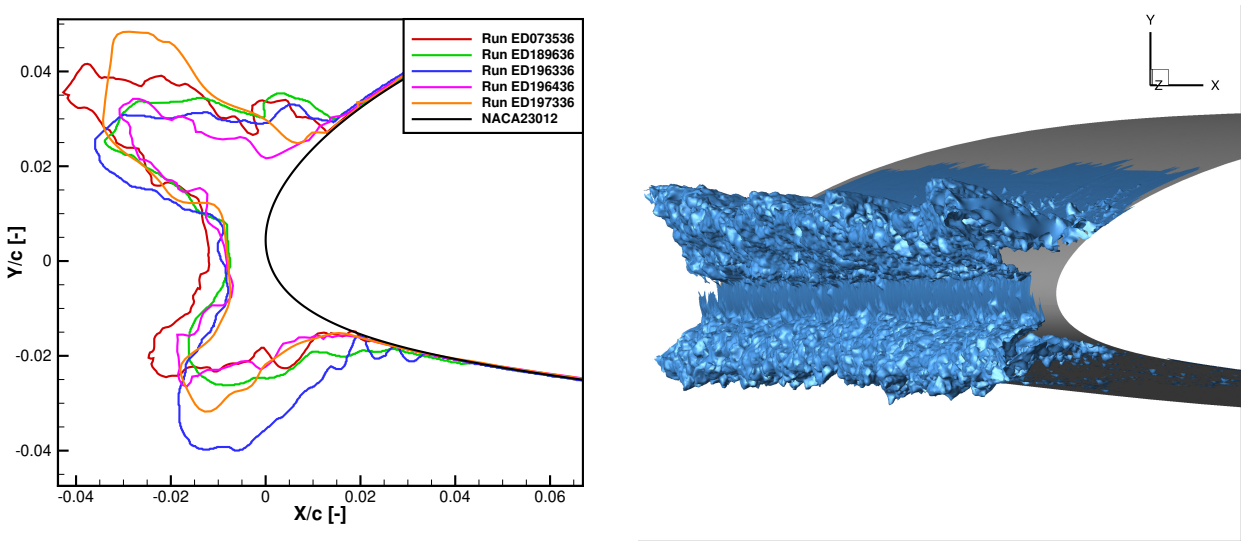

(a) Ice shape tracings - five trials

(b) Scan of the ice shape - one trial

Figure 1.3 Experimental results of case 242 [1]

Sources of Stochasticity

One of the significant sources of randomness comes from the cloud of supercooled droplets [13], which is known to have a stochastic structure [21]. Two main aspects are considered here: the spatial distribution of the droplets and their size distribution.

First, the position of the droplet in the cloud is random. Additionally, the probability of finding a droplet at a specific position can be considered as constant within the cloud, i.e.,the spatial distribution follows a uniform probability density function (PDF) [22]. Second, the droplet size varies throughout the cloud. Typically, the distribution of sizes is described in terms of :

- the median volume diameter (MVD), representing the diameter at which half of the water mass loading is contained in the smaller droplets and half in the larger [23];
- the liquid water content (LWC) fraction, representing the fraction of the total water mass loading in a given volume (i.e.,the cloud) coming from droplets in a given diameter range.

As for the other sources of randomness, one can note :

- the random distribution of surface imperfections, acting as nuclei for the freezing process [3];

- the stochastic nucleation at the liquid/subtrate interface [8].

1.3 Problem Statement

While ice accretion is a well-known problem, it is still not entirely understood [3, 8]. The effect of the stochasticity and the mechanisms at the microscopic and mesoscopic scales on the macroscopic phenomenon, i.e.,what we observe, are yet to be completely assessed [8]. There are two main active fields of research to further the understanding of these underlying processes [13]:

- Experimental tests;
- Numerical simulations.

The experimental tests include in-flight tests and icing wind tunnel experiments. While these tests allow studying the actual icing phenomenon, they are expensive, hazardous, and restrictive [3, 13]. On one hand, in-flight tests can compromise the safety of the flight crew. On the other, icing wind tunnels, due to their limited size, require to match the actual scale of the studied cases; in most cases, it is not possible to fit the full-scale wing. This involves the design of alternative geometries that are small enough to fit in the wind tunnel, while keeping the flow field constant at the LE compared to the full-scale conditions, i.e.,the leading edge radius, the droplet diameter and the non-dimensional numbers, such as the Reynolds and Mach numbers, are kept constant [3]. Therefore, numerical simulations are used to study a large variety of icing conditions at a lower cost. Additionally, they are used in the design of de-icing systems and in the certification process to predict the ice shape resulting from the icing conditions stated in the FAR. Wind tunnel experiments are still needed to validate the numerical models, but the need for these tests is reduced [3].

The state-of-the-art of icing software typically involves the resolution of the following modules:

1. flow field;
2. droplet trajectories;
3. thermodynamic exchanges;
4. geometry evolution.

Typically, partial differential equations (PDE) are the mathematical foundations of these computational models. This numerical framework is based on the assumption that the icing process is a quasi-steady phenomenon. However, the real icing phenomenon is a dynamic process that evolves in time. Multiple time scales are involved, such as the freezing time of a single droplet or the global icing time in which the macroscopic phenomenon of the ice growth is observed. To increase the accuracy in the latter time scale, the previously mentioned modules are resolved in a time loop, which allows taking into account the effect of the newly iced geometry on the rest of the process [3,13]. The flow field, droplet trajectories, and thermodynamic exchanges are therefore resolved in steady-state for a fraction of the icing time, then the geometry is morphed, and the process is restarted until reaching the total icing time, requiring to re-discretize the computational domain after each evolution of the geometry (new mesh generation). This method is known as multi-layer [3].

The Reynolds Averaged Navier-Stokes (RANS) equations are resolved to obtain the flow field around the studied geometry. The droplet trajectories are computed using a Lagrangian particles tracking or an Eulerian representation of the droplet equation of motion [24]. The thermodynamic exchanges resolution is based on the iterative resolution of an algebraic formulation of the mass and energy balances or PDE systems. The iced geometry is typically obtained from an algebraic method, which moves the vertices of the surface according to the ice accretion mass rate [3].

This state-of-the-art framework is continuous and deterministic (i.e.,always leads to the same solution). Thus, it is not possible to capture the accretion of the discrete and stochastic ice morphologies mentioned in Section 1.2.2 [25]. Furthermore, the time step required to keep a reasonable computational time in the multi-layer framework can be too large to capture the initiation of those morphologies. For example, ice feathers can grow immediately at the initiation of the icing process [17] from small scale ice roughness elements [2], as illustrated in Figure 1.4. Additionally, the ice density is typically lower than the bulk ice due to air pockets trapped into the ice. However, it is treated, most of the time, as an independent variable in those models.

1.4 Research Objectives

Icing software can help to increase the understanding of the icing phenomenon. Underlying mechanisms, such as the formations of ice feathers, must be studied and their modeling requires to break with the determinist and continuous framework. Therefore, the current research project aims to model the stochastic ice shapes and the discrete ice structures within a non-determinist framework. Specific objectives are proposed :

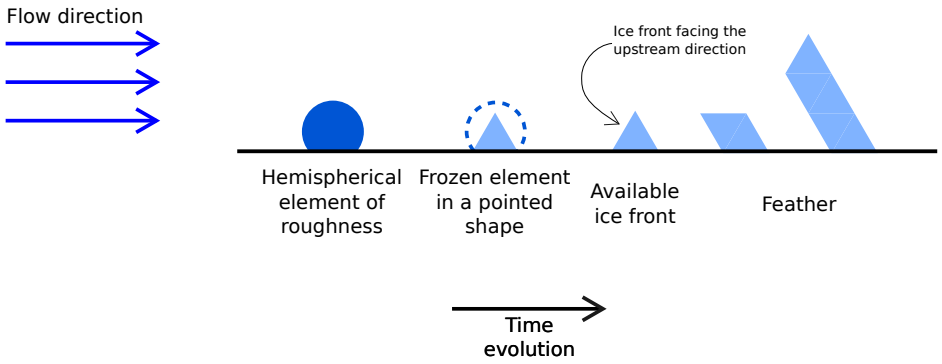

Figure 1.4 Schematic formation of ice feathers. Adapted from [2]

1. Model the ice shape in various icing conditions (rime and glaze);
2. Model the variability within the ice shape for multiple trials of the same conditions;
3. Investigate the model capacities to capture variable ice density and discrete ice structures.

Previous works, presented by Szilder and Lozowski [25] and Bourgault-Côté [3, 5], introduce stochasticity in the impingement and freezing processes to model the accretion of random and discrete structures. Both approaches, based on a discretization of the accretion domain using a Cartesian grid, lead to variable ice density and capture discrete and stochastic ice structures. Bourgault-Côté's approach, developed at Polytechnique Montréal, successfully simulates rime ice conditions. However, glaze ice shapes are not well captured, limiting the applicability of the model to simpler ice conditions [3, 5], far from the current state-of-the-art icing software requirements. Therefore, the current research project focuses on the development of a stochastic and discrete ice accretion model in the extension of Bourgault-Côté's work [3, 5].

1.5 Thesis Outline

Chapter 2 presents the state-of-the-art icing software, combined with a literature review of the existing alternatives to the deterministic and continuous frameworks. More specifically, stochastic and Lagrangian approaches are described. Chapter 3 proposes a complete original icing framework introducing randomness in the icing process to reproduce the stochastic structure of the cloud, thus breaking with the multi-layer determinist approach. Results are presented in Chapter 4, including test cases in rime and glaze icing conditions on 2D and

2.5D (i.e., swept wing) geometries. The conclusion completes the thesis in Chapter 5, along with the limitations of the proposed method and recommendations for future work.

CHAPTER 2 LITERATURE REVIEW

This chapter presents the framework typically used for the numerical simulation of the in-flight icing phenomenon, which is deterministic and continuous. An overview of alternative approaches is then presented, focusing on stochastic and discrete frameworks.

2.1 Deterministic Approach

The deterministic framework is the current state-of-the-art approach for icing software. At the first IPW, the results of nineteen participants out of twenty were obtained from deterministic solvers [1]. In general, the simulations follow the workflow illustrated in Figure 2.1.

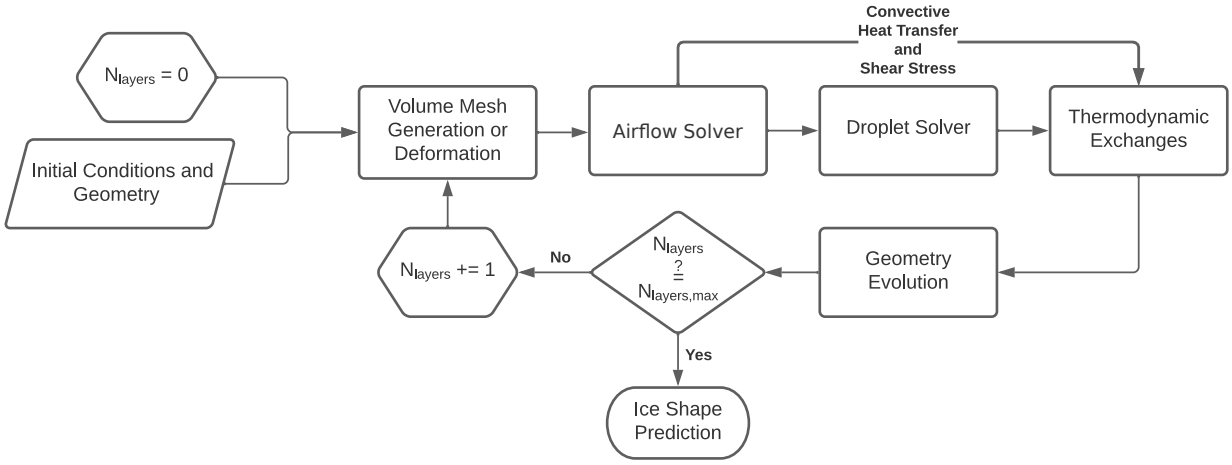

Figure 2.1 Typical deterministic workflow

As illustrated, the different models are solved sequentially, meaning that the icing phenomenon is treated in an one-way coupled fashion. Furthermore, even if the icing phenomenon is unsteady, the modules are resolved in a steady-state framework [3]. The icing process is considered as a quasi-steady phenomenon: the total icing time is split into intervals, referred to as layers of ice. After each layer, the obtained iced geometry is used as the studied geometry for the next layer. This process is represented by the loop in Figure 2.1 and requires generating a new volume mesh at the end each layer to discretize the new computational domain. To that end, for the resolution of the RANS equations, elliptic or hyperbolic mesh generators are typically used [3].

Each module is described in the following sections.

2.1.1 Airflow Solver

The flow resolution is required to simulate icing conditions as it drives the convective heat transfer and the droplet impingement on the airfoil surface. To that end, two main flow solvers are used in icing software: i) inviscid resolution with the potential method or Euler equations and ii) viscous resolution with the RANS equations.

The inviscid solver (either the panel method or the Euler solver) is coupled with a boundary layer method to resolve the heat transfer [4, 6, 26]. Although this method leads to fast resolution of the flow field, it is limited by the impossibility to compute the flow separation and the associated recirculation zones found behind horns [3, 6]. This framework is typical of the first generation of icing software [3, 4].

The resolution of the RANS equations enables the treatment of a wider range of geometries and scenarios, taking into account the viscous effects. It is also used to assess the performance degradation resulting from the ice accretion. This framework is typical of the second generation of icing software [3, 4], such as LEWICE3D [20], FENSAP-ICE [27] and IGLOO3D [28]. The convective heat transfer coefficient (HTC), one of the most important terms involved in the thermodynamic exchanges, is directly obtained from the resolution of the RANS equations with Newton's law of cooling, using either one flow field solutions [27], or two [29].

2.1.2 Droplet Solver

Once the flow field is obtained, the droplet impingement map on the surface is computed. One of the main simplifying assumptions associated with the droplet trajectory resolution is that the droplets do not affect the airflow due to their small mass loading, allowing for a one-way coupled resolution [3, 6, 24]. Here, the droplet cloud is referred to as the disperse phase.

The droplets are driven mainly by the drag, which depends on their velocity and shape, and the gravity. The associated trajectories are obtained from the resolution of the droplet equations of motion. The problem is described in either a Lagrangian or an Eulerian framework. Both methods result in the computation of the collection efficiency, which can be interpreted as the non-dimensional water impingement rate at the wall.

Lagrangian Method The Lagrangian description of the problem involves the discretization of the disperse phase by numerical particles, enabling the simulations of splashing, rebound, and break-up phenomena [3]. The equations of motion of each particle are resolved from a seeding point and the process stops when the particle reaches the geometry wall or leaves the computational domain [6]. The system is solved using an integration scheme, such as backward difference schemes or Runge-Kutta solvers [6, 30]. The time step is selected to ensure the stability of the integration scheme (if it is explicit). While the original Lagrangian description is a gridless method, Rendall and Allen [30], among others, proposed to resolve Newton's second law for finite volume framework using the RANS volume mesh, enabling the droplet to cross each RANS cell in a single time step. The method is based on the intersections between the droplet trajectories and the RANS mesh facets.

Eulerian Method Instead of the particle representation of the droplets, Bourgault [24] proposed to represent them as a continuous flow, based on the assumption that their concentration in the airflow is high enough [3, 31]. Therefore, the volume fraction, i.e.,the density, and the velocity field of the droplets are computed from the continuity and momentum equations, which form a PDE system. The resolution can be performed on the same mesh as the RANS equations, and the Eulerian approach simplifies and generalizes the droplet trajectory resolution [3, 24].

2.1.3 Thermodynamic Exchanges

With the HTC and the impingement map, the ice mass rate on the surface is computed from the thermodynamic exchanges. The mass and energy balances, performed on a control volume at the geometry surface, are illustrated in Figure 2.2, based on the work of Messinger [32]. Here, the balances are resolved with the assumption that the mass and energy exchanges reach the steady-state. More details on the formulation of the heat fluxes can be found in [4]. The control volume corresponds to the surface discretization of the RANS mesh.

An important parameter in Messinger work is the freezing fraction, which corresponds to the ratio between the ice mass rate and the sum of the incoming mass rates [32]:

$$f_{fr} = \frac{\dot{m}_{ice}}{\dot{m}_{in} + \dot{m}_{imp} - \dot{m}_{ev,sub}} \tag{2.1}$$

For glaze cases, $f_{fr} < 1.0$, meaning that there is water flowing out of the volume control; the runback water mass rate $\dot{m}_{out} \neq 0.0$. The ice mass rate $\dot{m}_{ice}$ and the runback water rate $\dot{m}_{out}$ are found with respectively the energy and the mass balances, posing $T_s = T_{fus}$, where T_s is

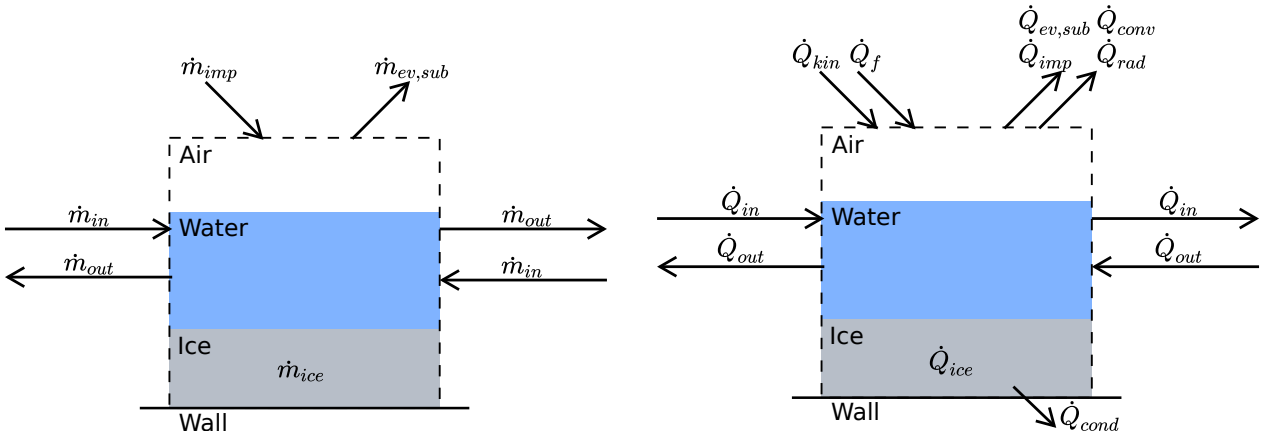

(a) Mass balance (b) Energy balance

Figure 2.2 Mass and energy balances on a control volume. Adapted from [3, 4].

the surface temperature [33]. For rime cases, $f_{fr} = 1.0$, meaning that all the incoming water freezes. The ice mass rate $\dot{m}_{ice}$ corresponds to the incoming mass rate $(\dot{m}_{in} + \dot{m}_{imp} - \dot{m}_{ev,sub})$ and T_s is found posing $\dot{m}_{out} = 0.0$.

The thermodynamic state is resolved for each surface element of the mesh from the stagnation point, where $\dot{m}_{in}$ is set to 0.0, to the trailing edge (TE), assuming that the water flows in the same direction, following the airflow streamlines [33,34]. This corresponds to the limitation of the Messinger model: it depends on the stagnation point [3] and is not suitable for complex geometries having multiple stagnation points [34]. Other models have been developed to overcome this limitation [33], such as the Iterative Messinger model [34] described briefly in the following section, the Extended Messinger model [35] and the Shallow Water Icing model [4, 36].

Iterative Messinger Model The Iterative Messinger model, developed by Zhu *et al.* [34], is based on the mass and energy balances of the Messinger model. However, the inflow mass rate $\dot{m}_{in}$ is treated as a system unknown. The runback direction is found using the shear stress direction at the geometry wall. The inflow mass rate is initialized at 0.0 in every surface element and the balances are resolved within an iterative loop, updating the values of $\dot{m}_{in}$ at each resolution, until reaching convergence.

2.1.4 Geometry Evolution

The state-of-the-art geometry evolution algorithms model the ice growth as a normal displacement of the surface vertices from the study geometry, such as the algebraic, level-set

and hyperbolic methods [3]. The distance of the displacement corresponds to the ice thickness and is associated with the ice mass rate, found with the thermodynamic model, and the icing time. One of the drawbacks of these methods is that the ice growth is treated as a normal extrusion of the studied geometry, instead of an accumulation phenomenon. Another challenging aspect is to ensure mass conservation while keeping a valid and well-discretized geometry in concave/convex regions [3].

2.2 Non-Deterministic Approaches

While the deterministic approaches are the state-of-the-art of icing software, underlying phenomena are neglected and discrete ice structures are missed, as presented in Section 1.3. Therefore, alternative approaches are proposed by different authors to further the understanding of the icing phenomenon. An overview of four methods is presented in the following sections. Other alternatives, such as the application of the lattice Boltzmann [37], the volume of fluid and moment of fluid [38] methods, are not discussed, but represent active research fields.

2.2.1 Morphogenetic Model

The Morphogenetic model, developed by Szilder and Lozowski [25,39], is a Lagrangian framework modeling the ice accretion by computing the thermodynamic state of individual fluid elements (liquid or frozen), represented by the cells of a Cartesian grid. It aims to predict at once discrete structures, namely rime ice feathers, and the water film encountered in glaze ice conditions. Furthermore, it leads to a variable ice density, which is known to be a shortcoming of the deterministic frameworks as the density is treated as an independent variable.

The method was initially developed in 2D for the simulations of the accretion of ice over cylinders exposed to freezing rain, such as power transmission lines [40]. Then, it was extended to in-flight icing on 2D cases, approximating the airfoil LE to a half-cylinder and using empirical relations to compute the mass and energy balances. The most recent developments allow the treatment of 3D geometries, namely swept wings [18, 41].

Cartesian Grid Discretization

The core of the Morphogenetic model is the use of a Cartesian grid to discretize the accretion domain. A complete rectangular lattice is overlaid on a portion of the geometry, as

represented in Figure 2.3. Each cell of the grid represents a single fluid element. The ice is accumulated in this grid in a building block manner, one element at a time [41].

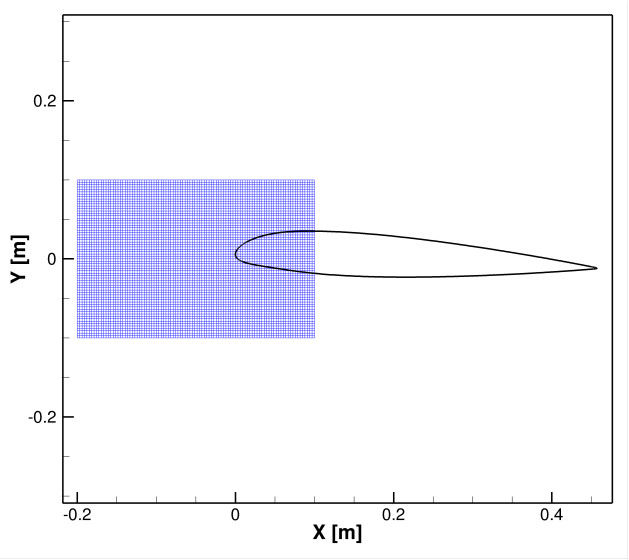

Figure 2.3 Representation of the rectangular lattice used in the Morphogenetic model

To reduce the computational cost, each cell of the grid represents a cluster of water droplets. This leads to the assumption that the gathered droplets follow exactly the same evolution; their trajectory, impinging location, and thermodynamic state are the same. The mass of the cluster is related to the size of the Cartesian grid cells, which is denoted by δ and corresponds to the cell side length.

The elements move into the Cartesian grid by successively visiting empty cells of the lattice, referred to as sites, from a random impingement location, which corresponds to an empty cell in the neighborhood of a frozen cell or on the clean surface. The visited sites are also on the surface of the current clean/iced geometry: at least one of their neighbor is either a frozen cell or a geometry wall. In this way, the method models the fluid motion on the surface to enable glaze ice simulation.

Random Impingement

The fluid element impinges the clean or iced surface randomly, respecting the collection efficiency distribution on the clean geometry [41]. The latter is given as an input to the Morphogenetic model and is obtained from a Lagrangian droplet trajectory solver performed for the clean airfoil using a monodisperse droplet size distribution. The collection efficiency is constant throughout the process and the impingement location of a fluid element is randomly

selected from the generation of a pseudo-random number (PRN), using a heuristic process [42]. It is not obtained directly from the trajectories of the fluid elements. The water mass distribution in impinged elements on the surface is limited by the distribution of the collection efficiency on the clean surface.

In an optimization of the Morphogenetic model, Burtnarasu *et al.* proposed to obtain the droplet trajectories by integrating the streamlines of an Eulerian droplet velocity field [42,43]. However, the integration is performed for each Cartesian cell visited using a Runge-Kutta scheme from the far-field to the airfoil surface, and the local droplet velocity is interpolated from the Eulerian field. While leading to a better representation of the trajectories than the original Morphogenetic model, the method is presented without much details on its implementation and the computation of the impingement locations. Additionally, since the integration is computed for each Cartesian cell visited, the associated computational costs are assumed to be significant.

Random Walk Model and Freezing

Upon impingement, a fluid element can either freeze or continue its motion to the next available site [41]. A random walk model controls the motion of each fluid element from its randomly selected impingement site: at each site along the surface a freezing probability P_{fr} is compared to a uniform PRN to determine the state of the fluid element at this site.

The Morphogenetic model uses Messinger's formulation of the steady-state mass and energy balances [32] to establish, at each visited site along the surface, the freezing probability, which corresponds to the definition of the freezing fraction on the clean geometry [25, 41]. The freezing probability at a site is locally computed using empirical relations for the heat flux formulations [25, 41].

There are two possible outcomes of the freezing probability comparison to the generated PRN [41]:

1. **If** $P_{fr} >$ PRN, the entire fluid element freezes at this site;
2. **Else**, the entire fluid element continues its motion to the next site.

The next treated site is the immediate neighbor site in the same orientation as the shear stress, based on the assumption that the airflow drives the water motion on the surface.

In the case of rime ice conditions ($P_{fr} = 1.0$), the fluid element freezes upon impact enabling the formation of ice feathers, while for glaze ice conditions ($P_{fr} < 1.0$), it can move further downstream on a significant distance [41].

Cradle Search

Szilder and Lozowski proposed a method, named the cradle search, to obtain relatively compact ice by modeling the tendency of the water to fill gaps due to its surface tension [25]. The cradle search is performed when a fluid element freezes, and consists of finding a cradle location, i.e.,the final resting position of the fluid element, within a given radius of the freezing cell: respectively 5δ and δ for glaze and rime ice, where δ is the element size. The final freezing position corresponds to the empty cell in this neighborhood which has the highest number of ice neighbors. If there is more than one site respecting this condition, the cradle location is randomly selected using a PRN. The choice of 5δ and δ for the neighborhood radius is arbitrary and only supported by the fact that the model results are within a reasonable range [25].

Extension to Multi-Layer

Burtnarasu *et al.* proposed an extension of the original Morphogenetic model to perform multi-layer simulations [42, 43]. At the end of each layer computation, the contour of the obtained ice shape is extracted from the Cartesian grid, and the next volume mesh is generated from this new geometry. However, it is unclear how the extraction of the ice boundaries is performed, and how it is processed to obtain a valid volume mesh.

2.2.2 Cartesian Advancing Front Algorithm

Bourgault-Côté proposed a stochastic alternative to the Morphogenetic model, replacing the complete Cartesian grid with a Cartesian advancing front technique [3, 5]. The accretion domain is limited to the ice front, reducing the computational requirements due to its minimal size. The flow and droplet fields, as well as the thermodynamic exchanges, are resolved before the stochastic method, using respectively the RANS and Eulerian droplet solvers and the Iterative Messinger model.

The initial front, formed of Cartesian cells, is created around the studied geometry wall, as presented at Figure 2.4(a). Two layers of halo cells are also created around the initial front to ease the advancing process. The cells are referred to as pixels. As proposed by Szilder [25], each pixel represents a fluid element.

To identify the pixels available to receive water, the collection efficiency and the droplet velocity, obtained from the Eulerian droplet solver in the RANS mesh, are interpolated to obtain the values in each Cartesian pixel. The impingement of a front pixel is possible only if the interpolated droplet velocity vector points towards it. In that case, the pixel status is

switched to active, represented in red in Figure 2.4(b). As proposed by Szilder [25], the active pixels are randomly impinged by the generation of a PRN, and the interpolated collection efficiency limits the impingement process. The impinging water mass is directly seeded in the front (active) pixels, the droplet trajectories are not computed.

Once an active pixel is randomly selected to be impinged, the latter can either freeze at the receiving pixel position (rime ice state) or flow downstream on the ice front (glaze ice state), following the same rationale proposed by Szilder [25]. However, the freezing probability is directly converted from the freezing fraction computed by the Iterative Messinger model. To that end, the freezing fraction is interpolated in the same manner as for the collection efficiency and droplet velocity. If a pixel freezes, it receives the status of frozen, and the front is updated and advances (new pixels are created), as illustrated in Figure 2.4(c). Although the process models successfully rime ice conditions, the glaze ice conditions are yet to be modeled [5].

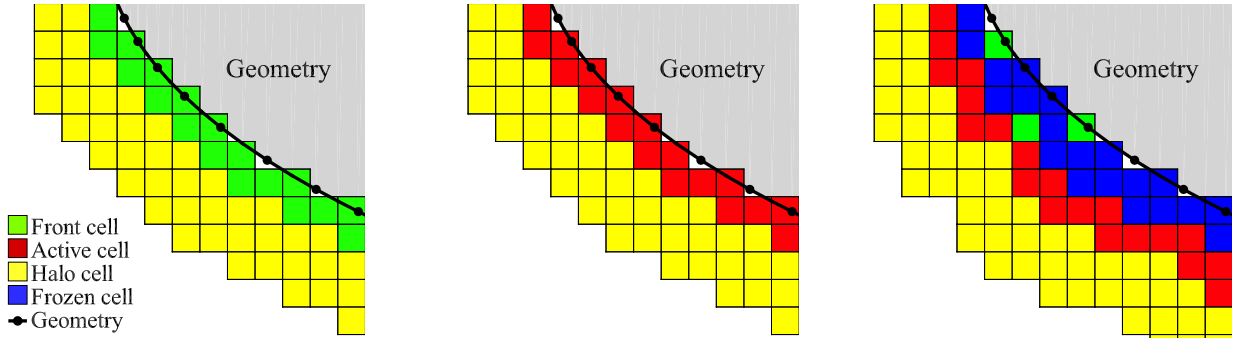

(a) Created front (b) Initial front (c) Updated front

Figure 2.4 Cartesian advancing front process [5]

The framework proposed by Bourgault-Côté also enables multi-layer simulations. To extract the ice contour at the end of each layer, a heuristic process is used to identify the frozen pixels located at the boundary of the ice and the air. Then, the coordinates of these pixels are converted to an ordered data set, and the corresponding new geometry is generated using a B-spline formulation to enable a robust multi-layer framework [44]. The following ice layer computations then starts with the re-meshing of this new geometry.

The results for this method on a rime case are presented in Figure 2.5 [5]. Figure 2.5(a) shows the stochastic ice mesh obtained from a single-layer simulation and the final ice front, represented by the active pixels in red. The B-spline extracted from the latter is represented in black, and the new geometry is smooth, contrary to the final ice front. Figure 2.5(b) presents the results for different numbers of layers. The single-layer result presents the

typical bubble-like ice shape [4], meaning that the random impingement process leads to water being seeded behind the ice front, i.e.,the shadow zones are not completely captured. The multi-layer results are in good agreement with the experimental ice shape.

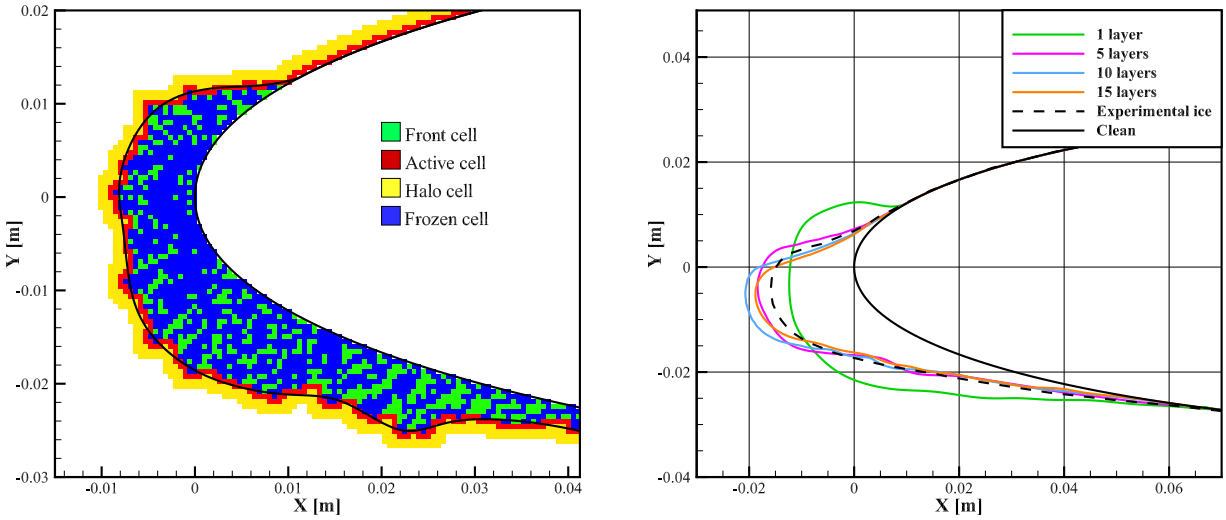

(a) Details of the Cartesian ice mesh created and the B-spline extraction. The B-spline is represented in black.

(b) Results for different number of layers

Figure 2.5 Results on rime case 01 [6] for the method of Bourgault-Côté [5]

2.2.3 Particle-Based Methods

Particle-based frameworks are also of interest for icing simulations, as they alleviate the restrictions imposed by the use of grids. Among others, two are presented here.

Spherical Element Framework

In a similar way to Szilder and Bourgault-Côté, Leroy developed a Lagrangian framework in which the fluid elements are represented by spherical particles of the same diameter as the treated droplets [45]. The method aims to reproduce the formation of ice scallops on swept cylinders in a 3D framework. The droplets are treated sequentially and they are seeded in the computational domain at a random position on a seeding plane upstream of the studied cylinder. The flow field is resolved beforehand with the panel method, and empirical relations are used to obtain the HTC. The trajectories are obtained from a Lagrangian solver. The droplets can either impinge on the clean geometry or previously frozen spheres. From there, the local freezing fraction is computed using Messinger's formulation of the mass and energy

balances. An empirical HTC model is proposed to include its variation depending on the position of the droplet on the ice front: if the droplet is on a local summit, the HTC is increased, while if it is in a local valley, the HTC is decreased. This variation is taken into account in the local freezing fraction computation. If $f_{fr} = 1.0$, the droplet performs one or two rotations on the ice front to reach a more stable resting position, which has a similar effect to the cradle search in Szilder's framework [25, 39]. If $f_{fr} < 1.0$, the runback water is modeled by the rolling motion of the individual spheres on the clean geometry or the previously frozen spheres. At each rotation, the local freezing fraction is computed to obtain the mass of ice to be accumulated, and a sphere of the corresponding diameter is left at this location to represent the frozen fluid element. The remaining mass flows downstream: a new sphere of the associated diameter rotates to the next runback site and the process is repeated until the remaining mass is negligible. Therefore, contrary to Szilder's framework [25, 39], partial freezing of the fluid elements is allowed.

Droplet-Scale Framework

Yuki and Yamamoto applied the moving particle semi-implicit (MPS) method, initially developed by [46] for nuclear applications, to the icing phenomenon [47]. In this approach, the water droplets are discretized as clusters of small numerical particles, enabling the modeling of droplet rebound and splashing phenomena [47]. The method aims to compute the phase change of each numerical particle from liquid to solid. This means that a single droplet can be constituted, at the same time, of liquid and solid numerical particles. The governing equations are the Navier-Stokes and the continuity equations, and they are resolved for the numerical particles. The droplets are inserted from a random initial location in the computational domain. The initial method only accounts for rime ice conditions and successfully reproduces ice feathers. However, the flow influence on the droplets is neglected, i.e.,they are traveling in a straight line. In a recent extension of the model, Toba *et al.* proposed a hybrid grid- and particle-based method to take into account the flow and heat transfer effects at the airfoil wall to simulate glaze ice cases [48]. To that end, the flow field is obtained from the RANS equations resolution with a finite difference method (grid-based), and the droplet trajectories are obtained within a Lagrangian framework (particle-based). The phase change of the numerical particles is then resolved using the MPS method, adding the resolution of the heat conduction equations to compute the heat transfer between the particles and the wall (particle-particle and particle-wall heat exchanges). Although the method leads to plausible ice shapes, it has yet to be validated on real icing conditions [48].

A comparison between the fluid element representation of the Cartesian grid methods and the particle-based frameworks is illustrated in Figure 2.6.

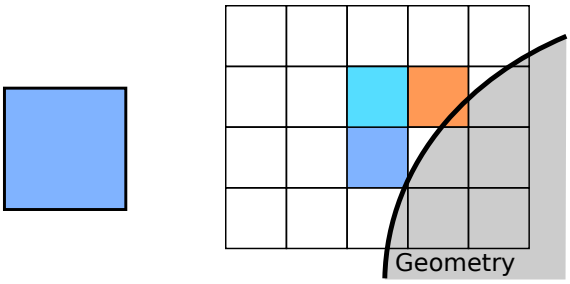

(a) Cartesian grid representation (Szilder [25] and Bourgault-Côté [3, 5])

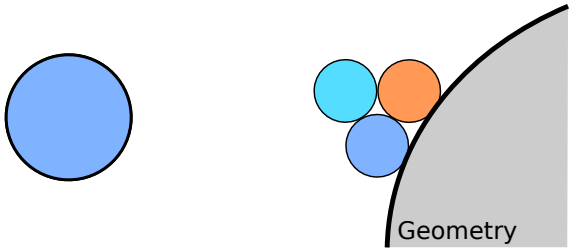

(b) Spherical element representation (Leroy [45])

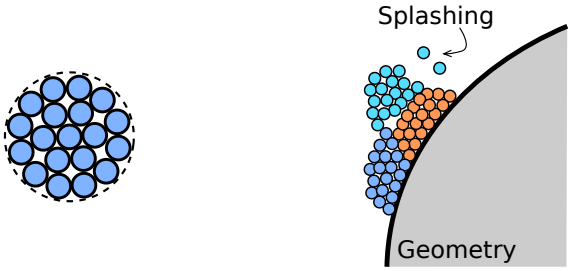

(c) MPS representation (Yuki and Yamamoto [47])

Figure 2.6 Comparison of the element representations. A single fluid element is represented on the left for each method. On the right, a simplified representation of the ice accumulation on the geometry is illustrated.

CHAPTER 3 NUMERICAL MODELING

This chapter presents an original and complete stochastic model. The Computational Fluid Dynamic software in which it is implemented is first presented. The methodology developed is then described in detail, including the modeling of the accretion of individual elements of ice, the droplet trajectory computations, and the thermodynamic exchanges to enable the simulations of glaze icing conditions. The verification of the process is then presented, followed by the proposition of an extension of the 2D model to improve the obtained results.

3.1 CHApel Multi-Physics Simulation

CHApel Multi-Physics Simulation (CHAMPS) is the new Computational Fluid Dynamic (CFD) solver developed using the Chapel programming language [49] at Polytechnique Montréal in professor Éric Laurendeau's team [50]. It is a 2D, 2.5D and 3D unstructured cell-centered finite volume framework solving the RANS equations, which are closed with Spalart-Allmaras [51,52] or the K-ωSST-V [53] turbulence models. The convective fluxes are discretized using Roe [54] or AUSM [55] schemes. The second-order of accuracy is achieved through Green-Gauss or Weighted Least Square formulations [55] for the gradients computations of the flow variables, and Barth-Jespersen [56], Venkatakrishnan [57], Van Leer or Van Albada [55] methods for their limiters. Time integration is performed using either the hybrid multi-stage Runge-Kutta scheme [58], or the implicit Lower-Upper Symmetric-Gauss-Seidel and Generalized Minimal Residual schemes. The solver is parallelized over shared and distributed memory, natively supported by Chapel.

The droplet trajectories are obtained from the resolution of the Eulerian equations [24]. The convective fluxes are computed using an upwind scheme and the gradient and limiter formulations are re-used from the flow solver. The thermodynamic exchanges on the geometry surface are resolved with an Iterative Messinger model [34]. To that end, the convective heat transfer coefficient (HTC) is obtained from the flow solver using Newton's law of cooling [4,27].

For the evolution of the geometry in the deterministic framework, a Lagrangian (or algebraic) method, or a hyperbolic scheme [3] are used to move the vertices of surface mesh following a normal extrusion. Then, to achieve multi-layer icing simulations, the computational domain is re-meshed to take into account the geometry evolution using a hyperbolic mesh generation [59].

3.2 Rationale

In order to represent the accretion domain, the original Morphogenetic model [25, 39] uses a complete rectangular lattice, while Bourgault-Côté [3, 5] proposed a Cartesian advancing front technique to reduce the computational cost. However, both approaches are not body-conforming and required post-processing to extract the ice front. To that end, heuristic rules are used to treat problematic features of the ice front, such as holes in the grid [3], leading to a possible lack of robustness in both methods.

The present work proposed an alternative that uses an unstructured advancing front algorithm instead of the Cartesian advancing front technique proposed by [3], to model the growth of the ice. This body-conforming approach allows representing the ice front as a valid surface mesh throughtout the process. Each element of the unstructured mesh corresponds to an element of ice, generated accordingly to the impingement location and the thermodynamic state, thus keeping the Lagrangian framework proposed in [3, 5, 25, 39]. In addition to the accretion domain discretization, the proposed method aims to better model :

- the droplet trajectory;
- the thermodynamic state;
- the runback water (displacement on the geometry and/or ice front).

Furthermore, the proposed method aims to account for the evolution of the geometry in a finner way than the multi-layer approach. This is the reason why the ice accretion is treated in a piecewise manner, using a stochastic and Lagrangian framework. The concept of droplet clusters is introduced in the same way as in the Morphogenetic model [25].

3.3 Global Process

Before the stochastic accretion process, the flow and droplet fields are resolved on the RANS volume mesh using respectively the RANS and Eulerian equations, as presented in the deterministic framework, described in Section 2.1. The thermodynamic exchanges are also computed in a deterministic manner on the RANS surface mesh, using the Iterative Messinger model, described in Section 2.1.3.

The global process, illustrated in Figure 3.1, goes as follows:

1. Insertion of a droplet cluster upstream of the studied geometry at a random location;

2. Resolution of the trajectory of the cluster :

   (a) **If** there is an intersection between the trajectory and the geometry, computation of the thermodynamic state;

   (b) **Else**, return to step 1.

3. Depending of the thermodynamic state, i. e. the freezing fraction f_{fr}, determination of the fraction of the cluster to be frozen :

   (a) **If** $f_{fr} = 1.0$, the cluster completely freezes;

   (b) **Else if** $f_{fr} < 1.0$, a fraction of the cluster freezes. The remaining mass moves downstream of the impingement location, on the clean and/or iced geometry;

      - Determination of the thermodynamic state at the new location of the cluster. Return to step 3a.

4. Return to step 1 until the targeted mass of the accumulated ice is reached.

In the process, each droplet is treated sequentially. The ice elements are created when a cluster freezes using an unstructured advancing front mesh generator, and the geometry is updated after the generation of each new element. Stochasticity is introduced through the insertion of the cluster in the computational domain. First, the cluster initial position is randomly generated on a seeding plane, upstream of the geometry, using a PRN. Second, the diameter of the droplets in the cluster is obtained randomly from the droplet size distribution, which is treated as a cumulative distribution function (CDF).

The main difference between the proposed alternative and the deterministic geometry evolution methods lies in the way to model the ice growth: in the latter, the ice is generated as a normal extrusion of the surface, while in the former, the ice is accreted on the surface in building block manner.

3.4 Unstructured Advancing Front Algorithm

The unstructured advancing front algorithm is a mesh generation technique in which elements (triangles in 2D or tetrahedra in 3D) are generated successively from the initial discretization of the boundary conditions, namely the initial front. The method is based on the dynamic evolution of this front and its update to generate a complete mesh.

To ease the description of the process, the definition of the following topological elements are required :

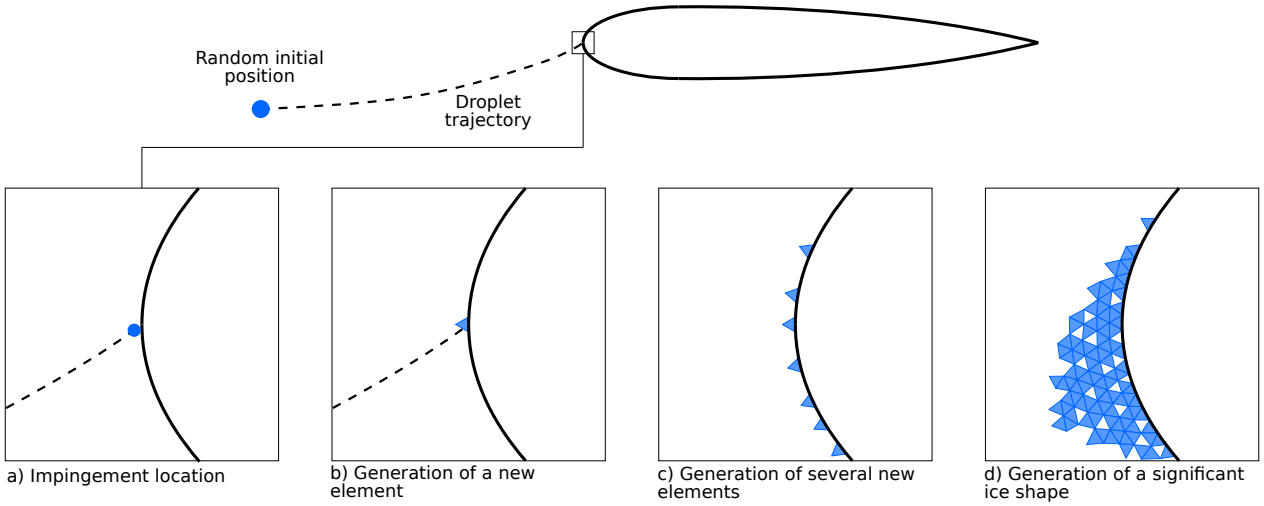

Figure 3.1 Global stochastic process

- A **node** is a 0D element, described by a single coordinate.
- A **facet** represents a surface and is formed by two nodes in 2D and at least three in 3D. In 2D, it is geometrically a line.
- An **element** represents a volume and is formed by at least three facets in 2D and four in 3D. In the present 2D framework, it is geometrically a triangle.
- The **front** is formed of the facets available to generate new elements.

The key components of the use of this mesh generator in the present icing context are:

- the initial front, which is the studied geometry;
- the order of treatment of the front facets;
- the stop criterion.

The usual implementation of the technique is first presented, then its application to the icing process is developed.

3.4.1 General Process

The unstructured advancing front technique implemented in the present work is based on the methodologies proposed by Lohner and Parikh [60], Peraire *et al.* [61] and Jin and Tanner [62].

The process goes as follows [63]:

1. Discretization of the boundaries, which form the initial front, as presented in Figure 3.2(a) in red;
2. Selection of the next front facet based on the predefined order of treatment.
3. Generation of the next element from the selected front facet, as illustrated in Figure 3.2(b);
   (a) Selection of an existing node or creation of a new node;
   (b) Validation of the new element (check intersections with existing elements), if invalid, return to step (2a);
4. Update of the front by removing the treated facet and adding the created facets (Figure 3.2(b), in red);
5. Repeat steps 2 to 4 until reaching the stop criterion (Figure 3.2(c)), which is usually when the front is empty.

Generation of an Element

The generation of a new element starts with the selected front facet. Then, an existing front node, or a new one, is selected to have the required number of nodes to form a complete element. This selection is based on a search of the neighboring front nodes.

It is performed around an optimal node position, which is (Figure 3.3):

$$P_{opt} = P_{facet} + \frac{\delta\sqrt{3}}{2}\vec{n}_{facet} \tag{3.1}$$

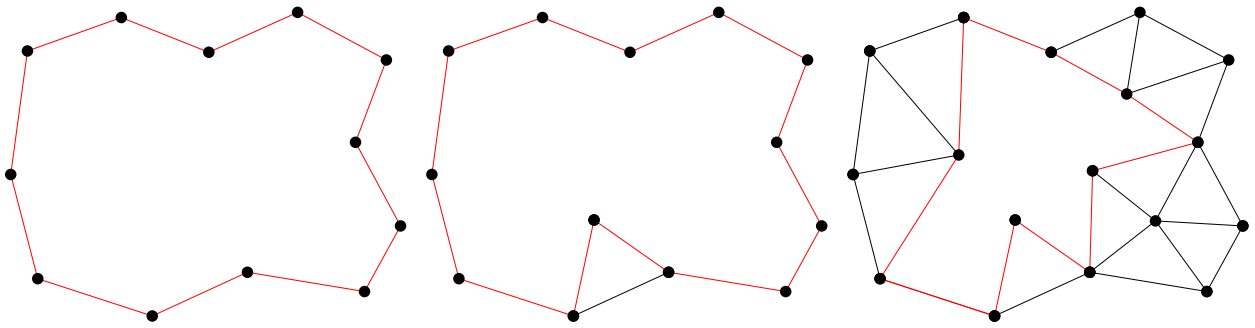

(a) Initial front (b) Generation of one element and update of the front (c) Front and mesh after several iterations

Figure 3.2 Unstructured advancing front process. The front is represented in red.

where P_{facet} and $\vec{n}_{facet}$ are respectively the center of the selected front facet and its unit normal, and δ is the targeted element size. The term $\delta\sqrt{3}/2$ is the height of an equilateral triangle with a side length of δ. The existing front nodes within a radius of 0.75δ of the optimal node are tested to assess if they form a valid element with the selected front facet.

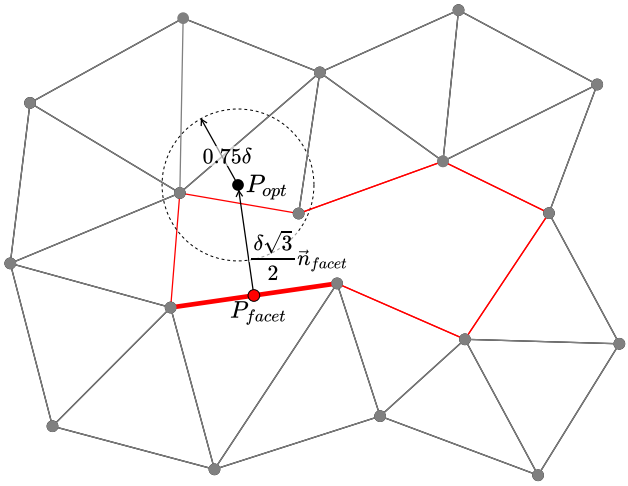

Figure 3.3 Optimal node position

The validity tests consist of checking if there is an intersection between existing elements of the mesh and the potential new element. If there is more than one valid potential element, the most regular one (i.e.,equilateral triangle) is selected. The validity and *well-shapeness* tests are well described in [60–62]. If no existing node forms a valid element, then a new node is created at the optimal node position (only if the corresponding element is valid).

The algorithm is converged when for each front facet treated, a valid element is generated. A complete and valid mesh then results from the process. In the case that no valid element can be formed for any remaining front facets, it is not converged and the generated mesh is incomplete.

3.4.2 Application to Icing

The interest of this method of generation of elements in the icing framework is related to three aspects of the advancing front process, namely :

- the order of treatment of the front facet;
- the creation of a new node;
- the selection of an existing node.

Before addressing these aspects, it is important to specify how the front and the element size are treated.

Initial front

As presented in Figure 3.2(a), the unstructured advancing front algorithm requires the discretization of the boundary conditions to initialize the mesh generation. In the present icing framework, it is the surface discretization of the studied airfoil. To ensure the regularity of the surface discretization, required for the convergence of the algorithm, the surface discretization of the RANS mesh is not used. Instead, a uniform surface mesh is used, based on the same geometry as the RANS mesh, as presented in Figure 3.4. It allows controlling the targeted element size of the ice mesh, independently of the volume mesh discretization. As a result, the surface mesh is generally an over-discretization of the RANS surface mesh. To simplify the following sections, the uniform surface mesh and the ice mesh generated by the unstructured advancing front are respectively referred to as the initial front and the stochastic mesh.

Active front

The active front is made of the facets that are available for the generation of a new element. In the present framework, these facets are the ones available for impingement. Throughout the generation of new ice elements, the active front becomes the ice front that "advances" in space, as the ice would grow in an experimental (or in-flight) context.

Element Size and Stop Criterion

Due to the droplets being gathered in clusters, the targeted element size must be linked to the mass of the cluster and the stop criterion to be consistent with the mass conservation.

In 2D, the volume of an element V_{element}, in m^2, is the area of a triangle. Since the process aims to generate regular elements (i.e.,equilateral triangles), the cluster mass m_{cluster}, in kg/m, is set to correspond to the mass of a regular element :

$$V_{\text{element, reg}} = \frac{\delta^2\sqrt{3}}{4} \tag{3.2}$$

$$m_{\text{cluster}} = V_{\text{element, reg}} \cdot \rho_{bulk,ice} \tag{3.3}$$

where $\rho_{bulk,ice}$ is the bulk ice density, $\rho_{bulk,ice} = 917$ kg/m^3. It is important to note that the mass is expressed in unit of span due to the present framework being in 2D.

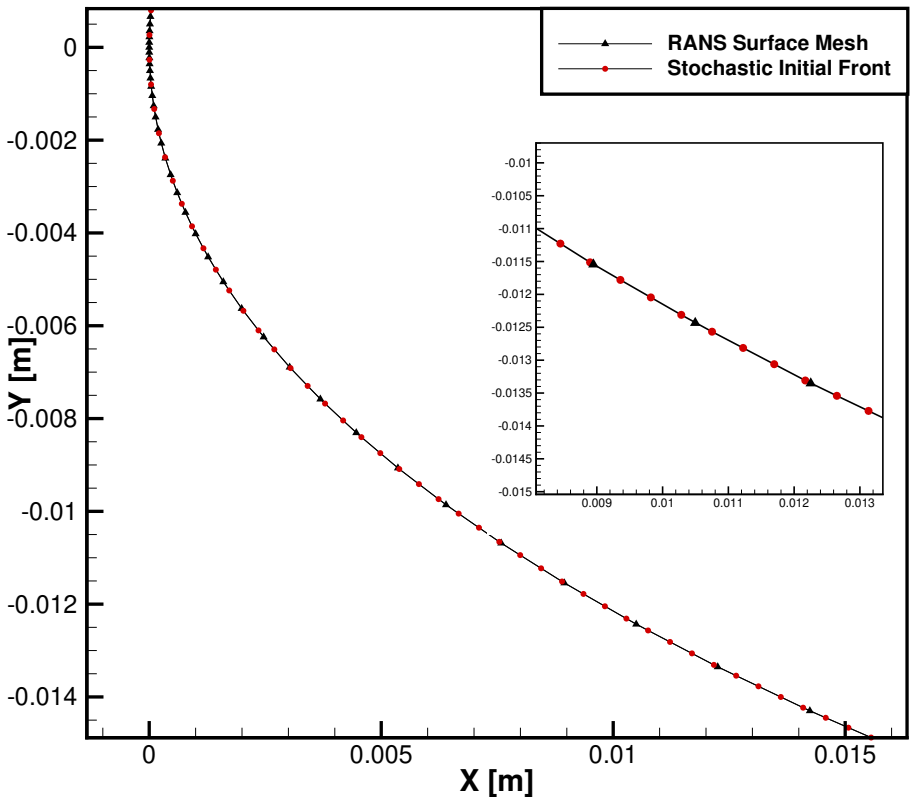

Figure 3.4 Comparison of the initial front and RANS surface mesh on the lower surface of a NACA0012

Throughout the process, even if it aims to generate regular elements, little variations are introduced in the element mass when an existing node is selected to form a new element. Therefore, the real element mass m_{element} is computed after its generation to be consistent with the mass conservation. Thus, the distinction between m_{cluster} and m_{element} is important for the stop criterion of the process, but also for the thermodynamic model presented at Section 3.6.

With the knowledge of the element mass, the accumulated mass of ice can be monitored. The process stops when it reaches the targeted mass, which is derived from the ice mass rate on the clean surface of the studied geometry, $\dot{m}_{ice}$ in kg/s, obtained from the deterministic thermodynamic model. This choice was made to respect the mass conservation.

The model used is the Iterative Messinger, presented in Section 2.1.3. The main assumption in this approach is that the system reaches the steady state; meaning that the thermodynamic exchanges are solved in terms of mass rate. Thus, the total ice mass to accumulate, $M_{total,ice}$,

is expressed according to :

$$M_{total,ice} = \Delta t_{icing} \cdot \sum_{i=1}^{n} \dot{m}_{ice,i} \tag{3.4}$$

where Δt_{icing} is the accretion time in seconds and n the number of surface elements of the RANS mesh. The process stops when :

$$\sum_{i=1}^{N} m_{\text{element}} = M_{total,ice} \tag{3.5}$$

where N is the number of ice elements in the stochastic mesh.

Order of Treatment of the Front Facets

Usually, the order of treatment of the front facet is based on their area [60–62]. In the present application of the unstructured advancing front technique, it depends on the droplet trajectories. Their computations are described in Section 3.5. For a given cluster of droplets, the intersection between its trajectory and the active front is computed to obtain the impingement location and the next front facet to be treated. For rime ice cases, the impingement location corresponds to the freezing location. Thus, a new element of ice is generated with the intersected front facet. For glaze ice cases, the thermodynamic state is checked upon impingement to assess the state of the cluster at this location, as described in Section 3.6. Therefore the intersected facet is not necessarily the next front facet to be treated. Indeed, if there is runback water, a fraction of the cluster is moved downstream on the ice front, requiring additional considerations to respect the mass conservation and thermodynamic state.

While the ice accumulates (i.e., elements are generated), the front advances creating a boundary to the droplet trajectories, as illustrated in Figure 3.5. Therefore, the proposed method allows accounting for the shadowing effect of the ice, which is not considered in the approach of Bourgault-Côté [3, 5] or in single-layer deterministic approaches.

Creation of a New Node

At the beginning of the process, the front corresponds to the clean geometry. The first elements of ice are generated with new nodes since no existing nodes are available. The creation of these new nodes allows reproducing the dynamic growth of the ice, thus supporting the choice of the advancing front technique.

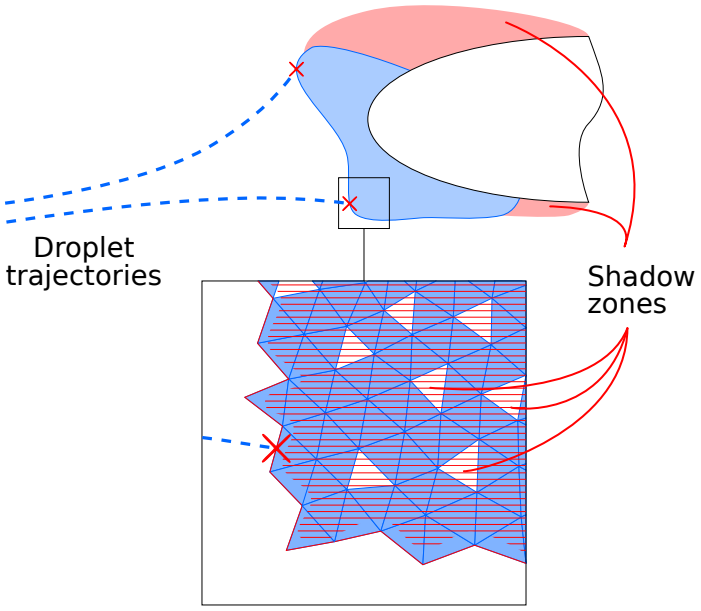

Figure 3.5 Shadow zones

Selection of an Existing Node

The order of treatment of the front facets and the selection of an existing node to generate a new element of ice enables the process to create air pockets in the ice. This is the characteristic of the method which leads to the ice density being a dependent variable. The creation of a pocket is illustrated in Figure 3.6. It happens when the main ice front closes on itself and becomes two distinct fronts :

1. the main ice front, represented by the solid red line;
2. the air pocket front (its boundaries), represented by the dashed red lines.

As shown in Figure 3.5, the creation of air pockets results also from the shadowing effect of the ice front: once created, the droplets can not impinge the boundaries of the pocket since they are behind the main ice front.

3.5 Droplet Trajectory Computations

The computation of the droplet trajectories is required to know the impingement map on the exposed surface, and therefore the order of treatment ice front facets (Section 3.4.2). As the ice grows, the impingement map changes due to the shadowing effect of the accretion. At the macroscopic scale, it can be observed behind ice horns where the droplets can not

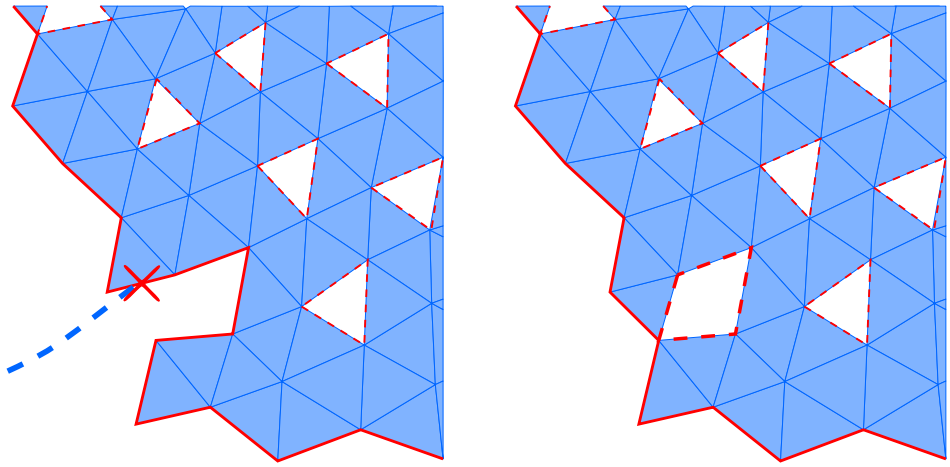

Figure 3.6 Creation of an air pocket

impinge, as illustrated in Figure 3.5. At the mesoscopic scale, the same phenomenon occurs behind ice feathers and roughness elements, leading to a greater accretion rate on the exposed surface of these structures [41]. As previously stated in Section 1.2.1, feathers can lead to more significant and hazardous ice structures, thus showing the need to better model their formations.

Therefore, the proposed methodology aims to take into account little changes of the geometry, generated by the unstructured advancing front technique, on the trajectories. To that end, a Lagrangian framework is proposed in which the clusters of droplets are treated sequentially as distinct elements. It is important to remind that the droplets forming the cluster follow the same evolution. Therefore, the trajectory of the cluster corresponds to the trajectory of a single droplet subject to the same conditions.

The interest in a Lagrangian framework comes from the fact that it allows computing the intersection point between the trajectory and the active front, i.e.,the impingement location. Knowing this, ice can be accreted as discrete elements upon impingement, or downstream of this location if there is runback water.

To obtain the trajectory, the equation of motion of the droplet can be resolved as described in Section 2.1.2. However, in the present framework, the Eulerian droplet solver is used for two reasons :

1. the impingement map on the clean surface is needed to compute the thermodynamic exchanges, required for the stop criterion previously presented (Section 3.4.2);

2. the impingement limits are needed to avoid the computational cost associated with the droplets not impacting the active front.

Therefore, the droplet trajectories are extracted from the Eulerian droplet velocity field, also proposed in [42]. However, here, the method follows the rationale of Rendall and Allen [30], who have proposed a finite volume representation of the flow streamlines and an extension to introduce the droplet equation of motion within their framework. Since the droplet velocity field is already known in the present framework, only the streamlines representation of Rendall and Allen is used: the trajectories are extracted as the streamlines of the Eulerian droplet velocity field.

The process uses the connectivities of the RANS volume mesh and requires the knowledge of the RANS cell in which the droplet is seeded. It does not require the integration of any differential equation, namely the droplet equation of motion [30]. There are two connectivity lists involved: i) cell-to-facets and ii) cell-to-cells defined. They are already computed in the RANS mesh pre-processing for the flow resolution, thus no additional steps are required.

As previously stated, the droplet is inserted at a random position, denoted $P_{d,0}$, within the field and upstream of the studied geometry. Therefore, the initial cell has to be found. To avoid extensive research in the entire computation domain, the cell containing the point $P_{d,0}$ is found using an octree research algorithm [64].

From the insertion of the droplet in the initial cell, the trajectory is extracted according to the following steps [30], illustrated in Figure 3.7:

1. Compute the intersections between the current cell's velocity ray $\vec{u}_d$ passing by the entry point $P_{d,entry}$ and the facets of the cell (Figure 3.7(a)), using the cell-to-facets connectivity list.

    - There are only two intersections possible : the entry point $P_{d,entry}$ and the exit point $P_{d,exit}$. The other facets are not intersected.

2. Select the intersection point in the same direction as the velocity ray :

$$(P_{d,exit} - P_{d,entry}) \cdot \vec{u}_d > 0$$

3. Locate the next cell to be crossed, which is on the other side of the intersected facet, using the cell-to-cells connectivity list.

4. Return to step 1, the exit point in the current cell being the entry point in the next cell (Figure 3.7(b)).

The facet/velocity ray intersection is computed using the parametric form of :

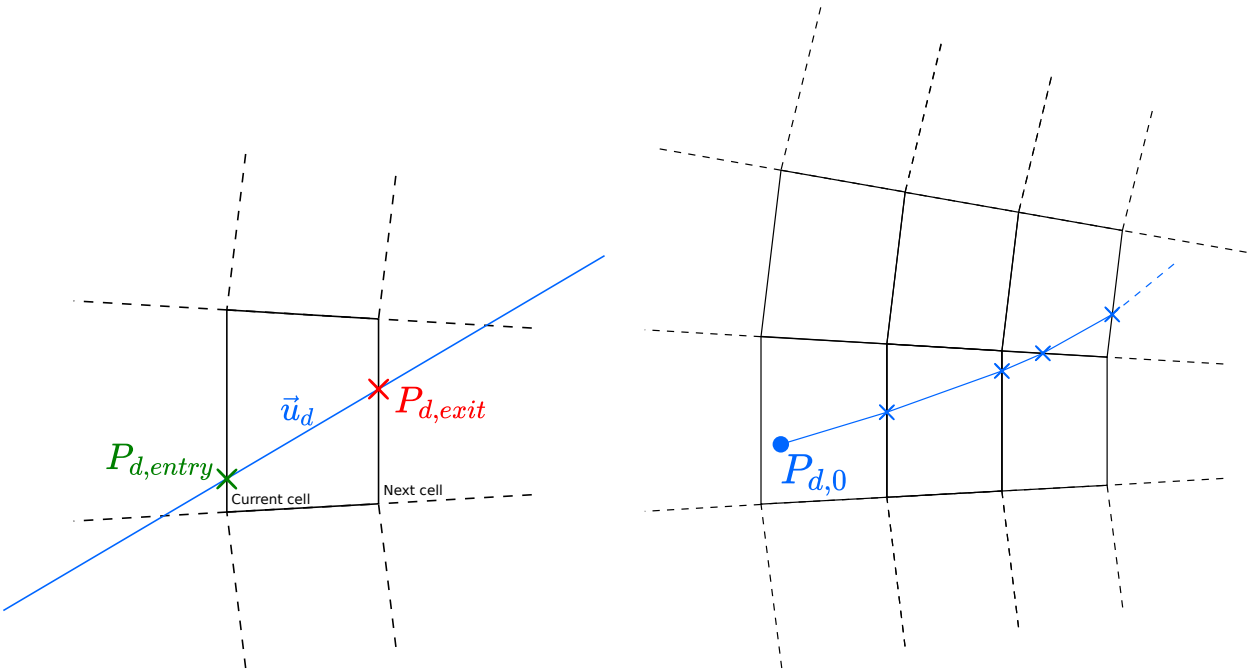

(a) Facet/velocity ray intersection computations in the current cell (in solid black)

(b) Droplet trajectory in the RANS mesh (in solid black)

Figure 3.7 Droplet trajectory computation

- a line segment (the facet) $\rightarrow X(s) = (1-s)P_0 + sP_1$ for $s \in [0,1]$, where P_0 and P_1 are the nodes forming the facet, and
- a ray $\rightarrow Y(t) = Q + t\vec{d}$ for $t \geq 0$, where Q and $\vec{d}$ are respectively the origin of the ray ($Q = P_{d,entry}$ in the present case), and the direction vector ($\vec{d} = \vec{u}_d$).

where s and t are the parametric independent variables. The intersection point, if any, is found solving $X(s) = Y(t)$ [65].

3.5.1 Seeding Process

The droplets are inserted at a random position on a seeding plane. Since the velocity field is already known, there is no minimum distance upstream of the geometry, unlike other Lagrangian approaches requiring a seeding plane sufficiently far so the flow velocity is close to the freestream value [66]. The only requirement is to accommodate the ice growth, i.e.,the droplets can not be inserted behind the ice front. It reduces the cost of trajectory computations.

In the present 2D approach, the seeding plane is a line. To simplify the seeding process, the plane is parallel to the vertical axis (noted y in the present framework) : $x = p_{seed}$ where

p_{seed} is the position of the plane on the x-axis, as presented in Figure 3.8(a). Hence, the initial coordinate of the droplet is : $P_{d,0} = (p_{seed}, y_{d,0}, 0.0)$.

Seeding Limits

To avoid computing unnecessary trajectories that do not impinge, the droplet initial positions are limited to an interval on the seeding plane, as illustrated in Figure 3.8(a). The limits are obtained with the upwind streamlines starting from the impingement limits on the clean surface (RANS surface mesh) [42]. Using the collection efficiency computed by the Eulerian solver, as presented in Section 2.1.2, the two positions on the surface from which $\beta < \epsilon$ are identified, where $\epsilon = 10^{-8}$ for the numerical implementation, as shown in Figure 3.8(b). They are then used as the initial positions for the computation of the upwind streamlines (Figure 3.8(a)).

To compute these streamlines, the same process presented at the beginning of this section is used. The only difference lies within the selection of the exit point (and by doing so, the following entry point). Indeed, the intersection point in the opposite direction of the velocity ray is selected [30], such that:

$$(P_{d,exit} - P_{d,entry}) \cdot \vec{u}_d < 0$$

The process stops when the streamline reaches the seeding plane, that is $P_{d,exit,x} < p_{seed}$, and $P_{d,exit,y}$ is an extremum for the initial position of the droplets. To take into account the growth of significant ice shapes, the interval is extended of at least 50% and is denoted $[y_{d,0,min}, y_{d,0,max}]$.

Pseudo-Random Intial Position

The droplet initial position is then obtained by the generation of a pseudo-random y-coordinate, $y_{d,0}$, to reproduce the stochastic structure of the cloud described in Section 1.2.2. A PRN is generated in the interval $[y_{d,0,min}, y_{d,0,max}]$ following an uniform distribution. Section 3.7 describes in more detail the PRN generator used in this process.

3.5.2 Impingement Location

The process proposed by Rendall and Allen stops when a wall boundary facet is reached [30], easily detected by the size of the cell-to-cells connectivity list of the last cell. However, in the present process, the ice grows (the ice front advances), and therefore the process stops if

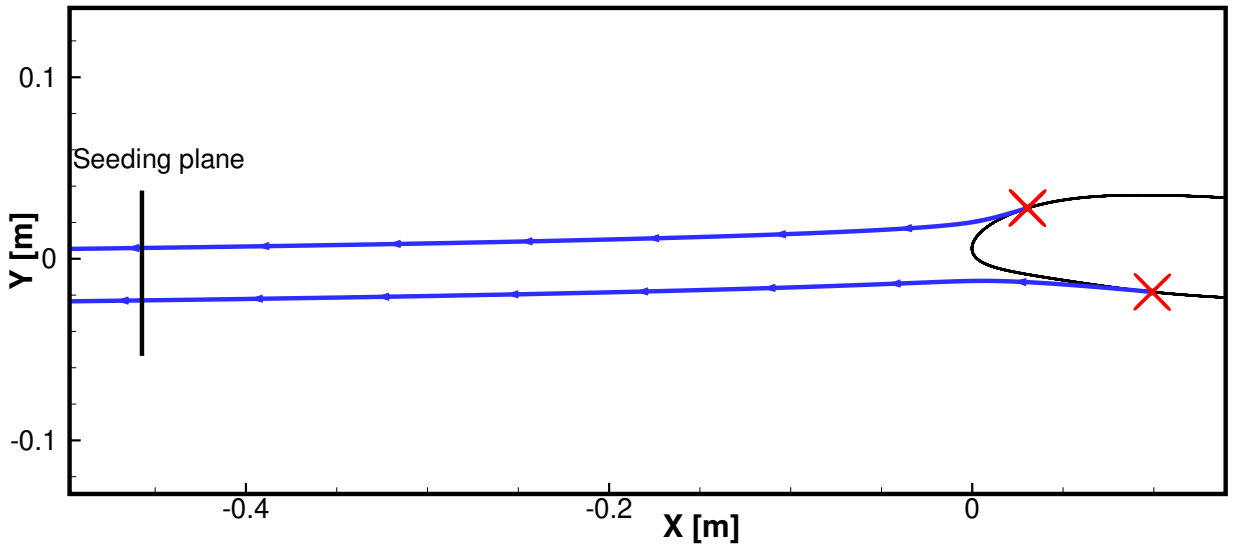

(a) Seeding plane position and limits obtained from the upwind droplet trajectories of the impingement limits (marked by the red 'X's)

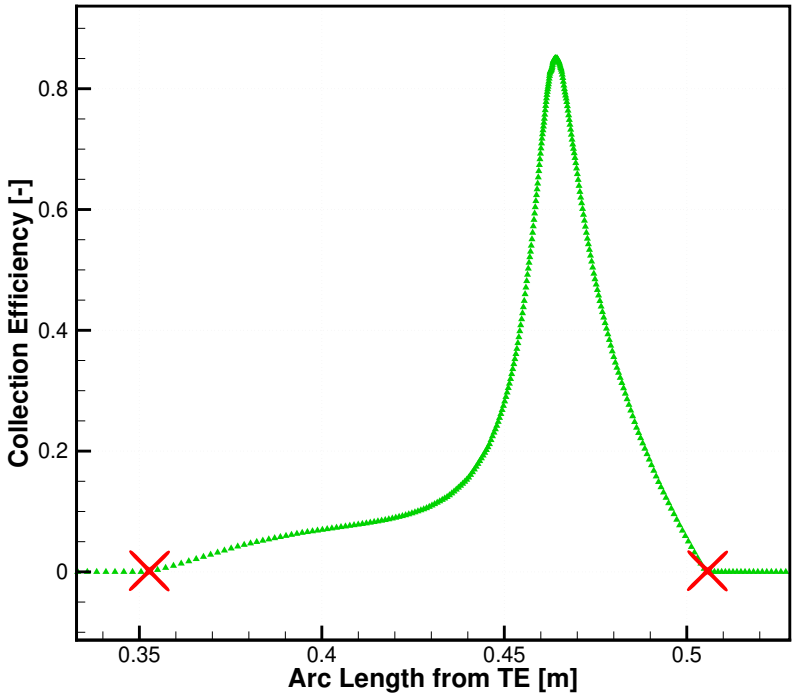

(b) Impingement limits on the clean surface marked by the red 'X's

Figure 3.8 Seeding process

the ice front is intersected.

The intersection between the droplet trajectory and the ice front corresponds to the impingement location illustrated in Figure 3.9. To reduce the computational cost of the intersection

checks between the front facets and the trajectory, only the facets within a disc with a radius of $r = 0.5\ ||P_{d,exit} - P_{d,entry}||$ centered at $P_{d,entry} + r$ are tested, shown in solid red in Figure 3.9(b). An octree is used again to identify those facets.

From there, the intersection between each facet (forming a line segment) and the line segment between the points $P_{d,entry}$ and $P_{d,exit}$ is computed in the same manner as the facet/velocity ray intersection. If none of the identified front facets are intersected, then the process continues to the next RANS cell to be crossed. If there is more than one intersection, the nearest of the point $P_{d,entry}$ is chosen as the impingement location.

3.5.3 Droplet Size Distribution Treatment

For the same initial position, the trajectory and the impingement location change according to the droplet size. The velocity fields and the trajectories for different droplet sizes in the same flow conditions are shown in Figure 3.10. One can note the variations in the impingement limits: the larger droplets tend to impinge further downstream compared to the smaller droplets, due to their inertia. Therefore, it is important to take into account the size distribution to well capture the limits and thickness of the ice. Other non-determinist approaches do not consider it [3, 5, 25, 39].

The droplet size distribution of the cloud is continuous. However, to resolve the droplet field, the distribution is expressed in a discrete form as the cumulative fraction of the LWC versus the droplet diameter. Figure 3.11 compares the continuous and the discrete forms of the Langmuir D distribution, commonly used in the literature when the experimental distribution is not available [4]. In the determinist framework, the droplet velocity field is obtained for each droplet diameter, referred to as bin, using the Eulerian solver and the collection efficiency at the wall is the weighted average of the surface solutions. Since the present framework treats the droplet as individual elements, their size is generated as a random sample that follows the size distribution of the studied case, as described in the following sub-section.

Hence, when a cluster is seeded in the computational domain, its trajectory is computed using the velocity field associated with the randomly sampled droplet diameter. It is important to note that in the proposed model, the element size used in the unstructured advancing front algorithm does not change since it is associated with the cluster size and not the droplet diameter.

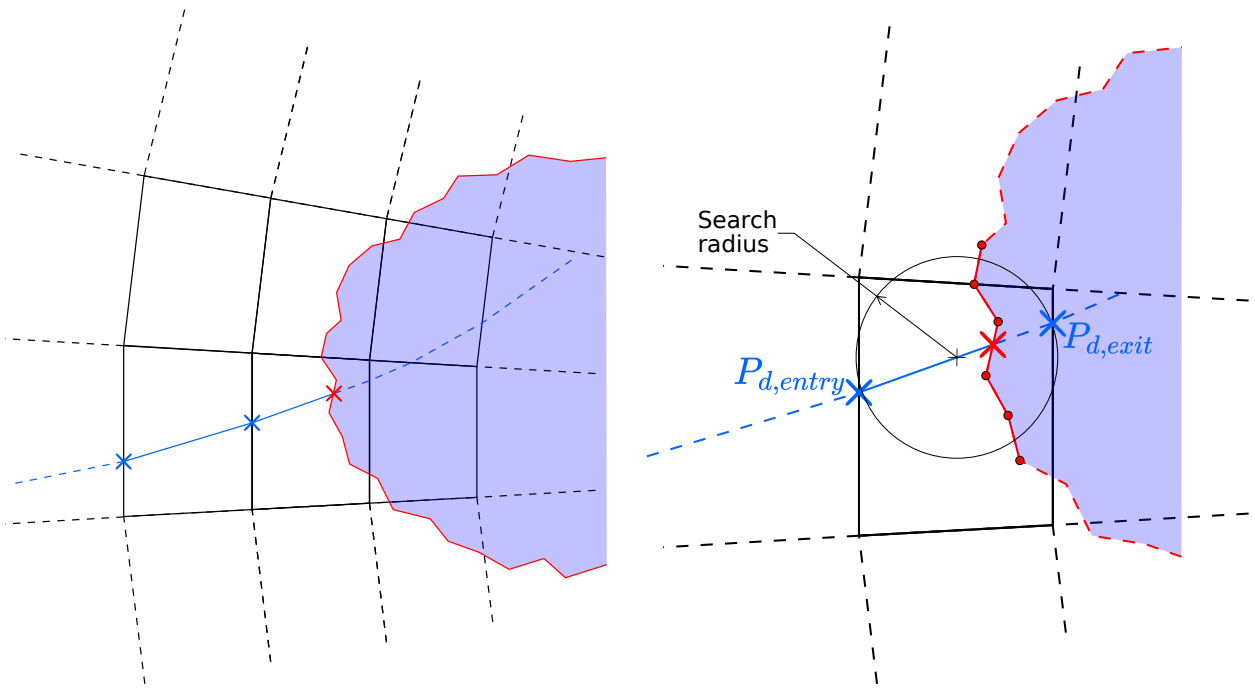

(a) Droplet trajectory intersection with the ice front

(b) Intersection check zoomed

Figure 3.9 Computation of the impingement location, mark by the red "X". The droplet trajectory is in solid blue and the ice front in red delimiting the ice in light blue.

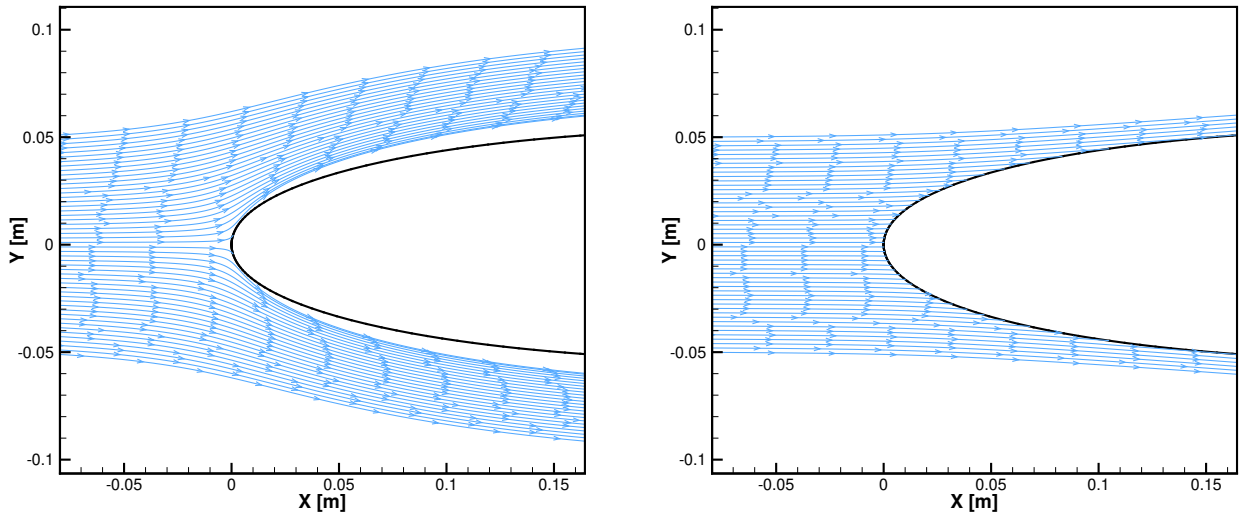

(a) Droplet trajectories for $D_{droplet} = 6.40\mu$m

(b) Droplet trajectories for $D_{droplet} = 99.9\mu$m

Figure 3.10 Comparison of the trajectories for different droplet diameters for case 364 [1]. The droplet trajectories are in solid blue and the geometry in black.

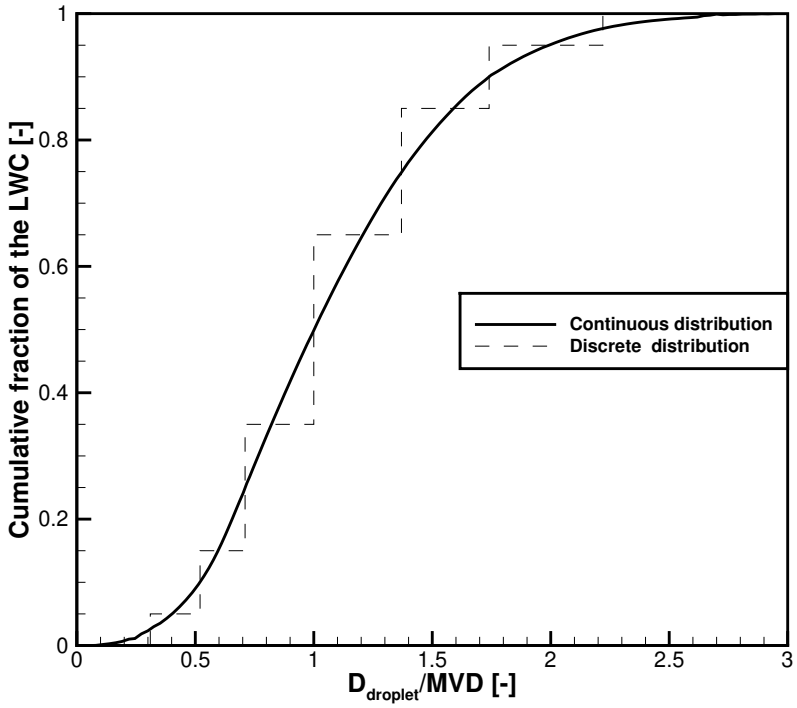

Figure 3.11 Langmuir D distribution. Data extracted from [7].

Sampling Method

The inverse transform sampling generates a random sample of the variable Θ following a given continuous PDF, $p(\Theta)$, using the associated CDF, $F(\Theta)$, and an uniform random variable, $u \in [0, 1]$ [67]. The process associates u to Θ using the inverse of $u = F(\Theta)$, that is $\Theta = F^{-1}(u)$, as illustrated in Figure 3.12(a), and insures that a distribution of n uniform variables u follow $p(\Theta)$.

For discrete PDFs, such as the dropet size distribution, the same rationale is applied, as shown in Figure 3.12(b). In the proposed framework, the size distribution is directly converted to a discrete CDF, and each bin i corresponds to a sub-interval, I_i, of the unit interval $[0, 1]$. The droplet diameter is obtained from the discrete CDF and the process follows these steps:

1. Generate an uniform PRN, $u \in [0, 1]$;
2. Find the interval I_i of the discrete CDF for which $u \in I_i$, where i is the bin;
3. Return the diameter associated to the bin i.

The PRN is generated in the same way as for the initial position, and more details are given at Section 3.7.

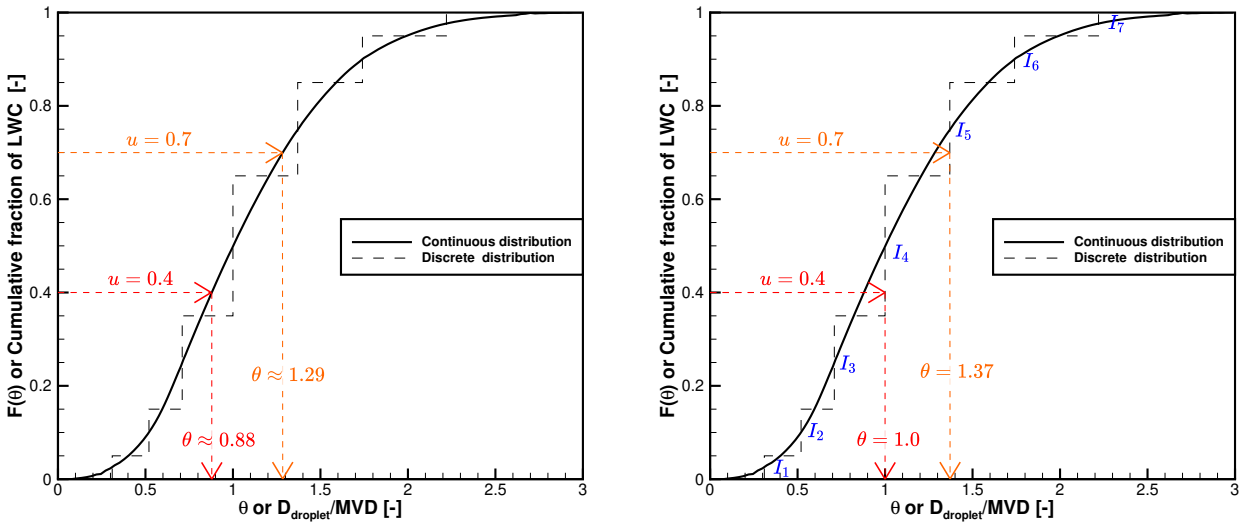

(a) Process for a continuous CDF

(b) Process for a discrete CDF

Figure 3.12 Inverse transform sampling

3.6 Thermodynamic Modeling

As previously stated, upon impingement, the cluster can either freeze or flow downstream according to the thermodynamic state. Its modeling enables the treatment of glaze icing conditions and requires to treat of two main phenomena:

1. the partial freezing of the incoming water, and
2. the water motion on the surface (runback).

The Morphogenetic method uses a random walk model based on Messinger's formulation of the mass and energy balances to compute a local freezing probability, P_{fr}, at each step of the fluid element motion, as presented in Section 2.2.1. This framework enables to successfully model glaze conditions and captures ice horns [18, 41]. Empirical relations for the heat flux and the freezing probability computations are used, simplifying the model and allowing to compute the freezing fraction locally at each visited site [41], to the author understanding. However, given the current icing software requirements of accuracy, empirical relations are not sufficient. Bourgault-Côté thus proposed to use an Iterative Messinger model to compute the freezing probability, posing $P_{fr} = f_{fr}$ [3,5], but glaze icing conditions are not successfully modeled within this framework, as presented in Section 2.2.2.

Leroy proposed to compute a local freezing fraction and the process allows that only the corresponding fraction of the water freezes at each motion of the fluid element [45],as de-

scribed in Section 2.2.3, unlike Szilder's work [25,41]. The local freezing fraction is computed upon impingement based on a modified formulation of the Messinger balances: the rate of incoming water from the runback water is $\dot{m}_{in} = 0.0$. This modification comes from the fact that the model treats the freezing of the fluid elements independently, i.e.,the water film is only formed by the downstream motion of the fluid element currently treated and there is no liquid water remaining from the previously treated elements.

The present method proposes a hybrid method of these previous works:

- the global thermodynamic state is computed before the stochastic process, using the Iterative Messinger model, as Bourgault-Côté, and;
- partial freezing of the clusters is permitted, as Leroy.

3.6.1 Global Process

The thermodynamic process starts after the impingement location computation. Since the freezing fraction is computed on the clean surface, its value at the impingement location is set to the value of the nearest element of the surface RANS mesh (on which the thermodynamic exchanges are computed by the Iterative Messinger solver). This nearest element is denoted as the donor element. It is worth noting that the freezing fraction is constant throughout the process since the thermodynamic solver and the stochastic model are launched sequentially [3, 5]. This allows being consistent with the proposed stop criterion of the entire process, presented in Section 3.4.

Recalling the freezing fraction definition :

$$f_{fr} = \frac{\dot{m}_{ice}}{\dot{m}_{imp} + \dot{m}_{in} - \dot{m}_{es}}$$

Here, the evaporation/sublimation mass rate is neglected, following the work of Leroy [45]. Furthermore, the freezing fraction is expressed in terms of masses (instead of mass rates), since a cluster represents a mass of water in the present framework:

$$f_{fr} = \frac{m_{ice}}{m_{imp} + m_{in}}$$

Therefore, the mass of water to be frozen is obtained using :

$$m_{ice} = f_{fr}(m_{imp} + m_{in}) \tag{3.6}$$

The mass of water remaining forms the runback water and is obtained according to :

$$m_{out} = m_{imp} + m_{in} - m_{ice} \tag{3.7}$$

which represents the mass balance at the surface of the receiving front facet.

The process workflow is illustrated in Figure 3.13. Upon impingement, the rate of incoming water m_{in} is null, as proposed in [45]. This assumption can be interpreted looking at the first treated cluster: there is no water on the surface, and the water running back is entirely frozen at the end of its motion. Since the process treats the clusters individually and sequentially, there is no impingement mass for the subsequent steps of the cluster motion on the front: $m_{imp} = 0.0$.

Then, each front facet downstream of the impinged facet is sequentially treated to compute the mass of water that freezes at this step, according to Equation 3.6. The remaining mass m_{out} (Equation 3.7) flows to the neighbor front facet in the same orientation of the skin friction coefficient $\vec{C}_f$, and corresponds to m_{in} in the next mass balance computation. This front facet is referred to as the receiving facet.

The process stops when the remaining mass of water m_{out} is negligible. The threshold, heuristically chosen, is : $m_{out} \leq 0.01 m_{cluster}$. This happens in two situations:

- the cluster reaches $f_{fr} = 1.0$, or;
- the runback water has run out.

Then, the next cluster is seeded in the computational domain, according to the process described in Section 3.5. Given that, the proposed method is not stochastic for the thermodynamic and runback modeling. The stochasticity is only introduced by the droplet trajectory solver via the random impingement location.

Runback Modeling

At each step of the cluster motion on the surface, only a fraction of the water freezes. However, new elements of ice are not necessarily generated from this fraction of water to ensure that the advancing front algorithm converges by generating mostly regular elements respecting the targetted element size δ.

A new element of ice is generated only when the mass of ice stored on a front facet respects the following heuristic criterion :

$$m_{ice} \geq 0.9 m_{cluster} \tag{3.8}$$

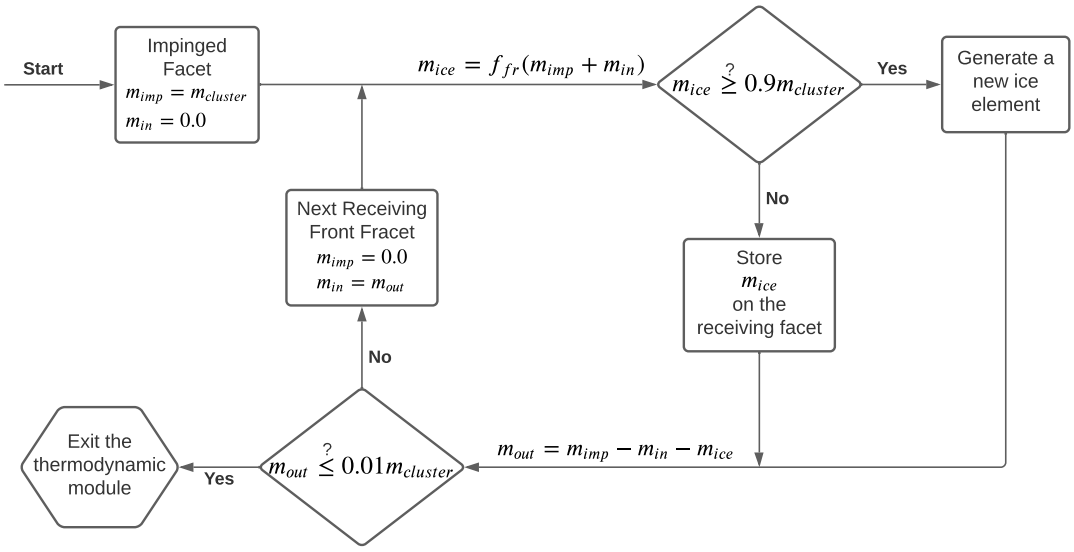

Figure 3.13 Workflow of the thermodynamic model

It is selected to insure the generation of mostly regular elements with the advancing front technique. Figure 3.14 illustrates this process.

If the criterion is not respected, the mass of water to be frozen is stored on the current front facet and the motion continues to the neighbor facet. The next time this front facet is treated, the criterion is checked again, taking into account the ice mass previously stored to determine if a new element of ice is generated.

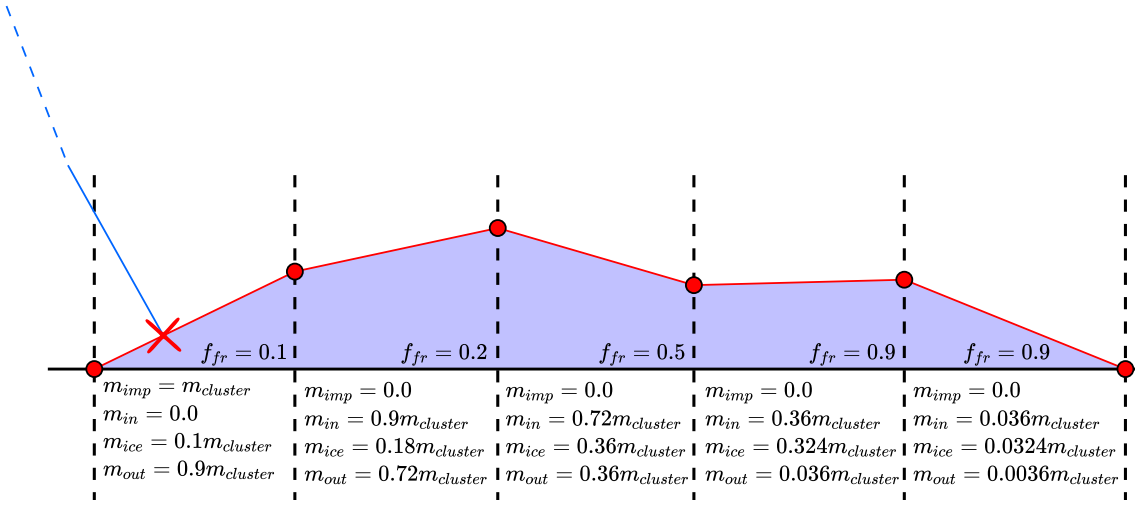

(a) First impingement and cluster mass distribution on the active front

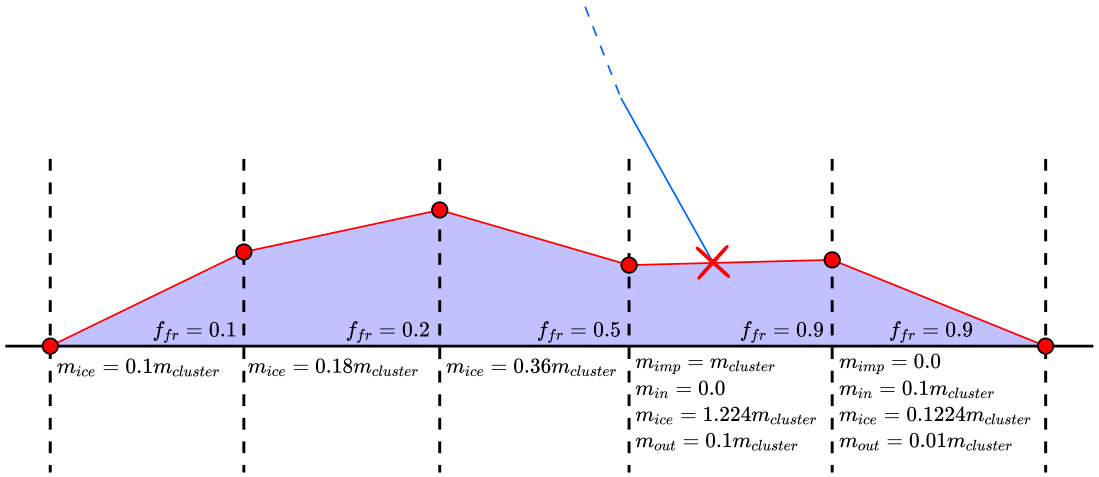

(b) Second impingement

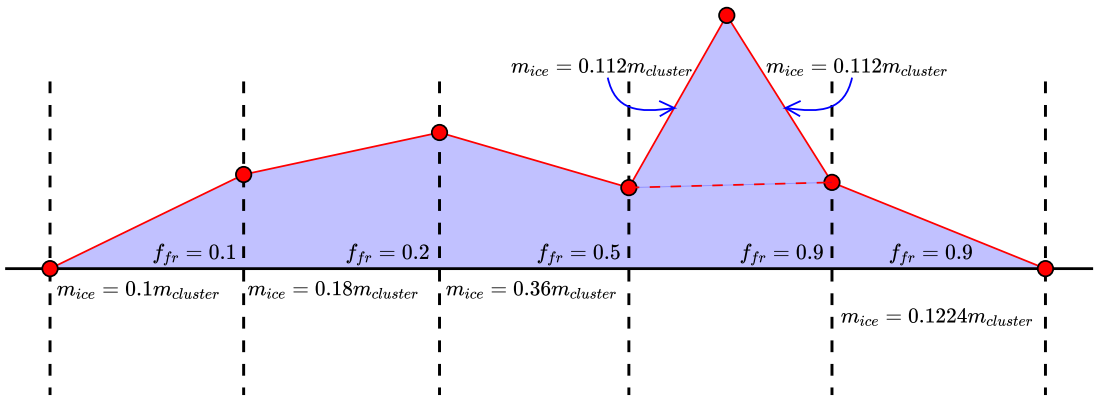

(c) Generation of new ice element from a front facet respecting the criterion of Equation 3.8

Figure 3.14 Cluster motion on the active front

Runback Direction

Two aspects of the motion of the water are modeled in this framework :

1. the shear stress orientation;
2. the selection of the receiving facet.

Shear stress orientation The runback water flows according to the airflow on the surface. In the present framework, the flow field is computed only at the beginning of the process, such as in a single layer approach. Therefore, the effect of the ice growth on the airflow is not taken into account, and the real orientation of the shear stress at the ice front surface is not available.

Two approximations of the runback orientation are considered :

- the skin friction coefficient $\vec{C}_f$ at the nearest cell of the surface RANS mesh;
- the interpolated value of the airflow velocity $\vec{U}_a$ obtained at the initial resolution of the flow field.

The former formulation is selected and Figure 3.15 illustrates this choice: the orientation of $\vec{C}_f$ and $\vec{U}_a$ are compared at a given position on the ice front, marked in red. The black arrows represent the streamlines of the flow field. Knowing that the real orientation of the shear stress is tangential to the ice, depicted by the blue curve, the $\vec{C}_f$ orientation gives a better approximation than $\vec{U}_a$.

This method is limited to streamwise ice shapes. For cases with significant ice horns, this definition quickly becomes false as the horns grow, given their strong effect on the airflow [14].

Selection of the receiving facet Since the stochastic mesh is formed of triangular elements, the ice front is irregular and concavities are formed. For example, if the impingement location is within a concavity, marked in red in Figure 3.16(a), the selection of the next receiving facet is ambiguous, as the two neighbor front facets are in the opposite direction (highlighted by the black arrows) of $\vec{C}_f$.

Therefore, the receiving facet is obtained using the front connectivity. The orientation of the facets in a 1D stencil of N neighbor facets on the left and right sides of the impinged facet is tested, as illustrated in Figure 3.16(b). The side (left or right) for which there are more

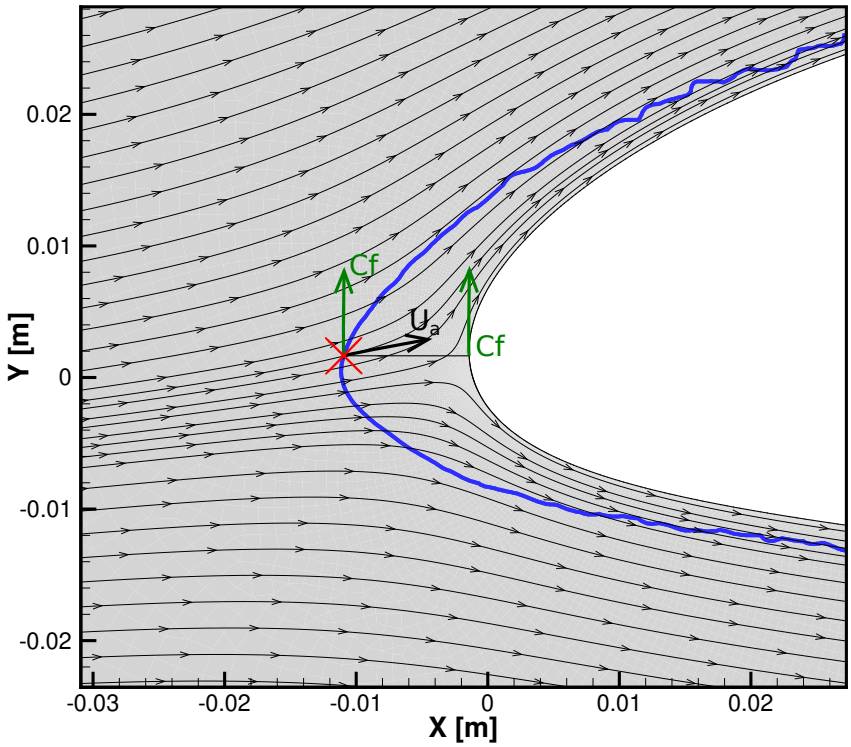

Figure 3.15 Approximation of the runback direction

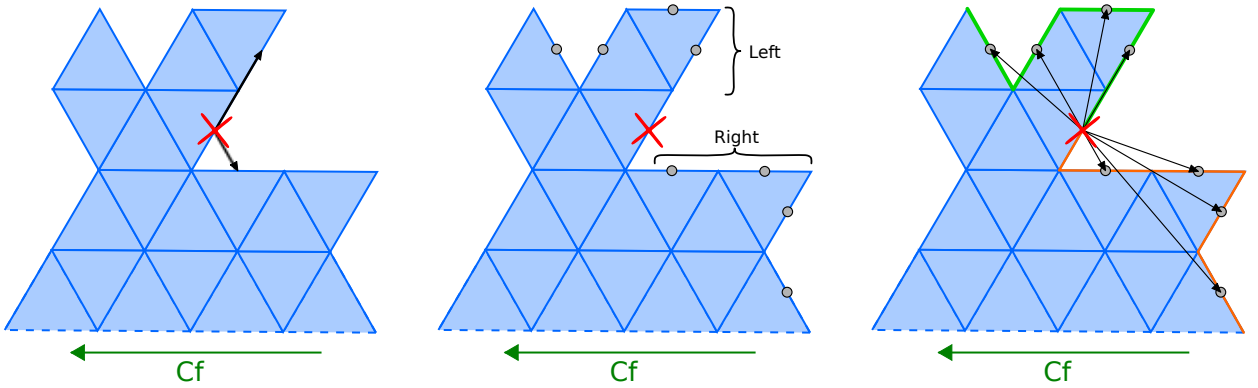

(a) Irregular ice front

(b) Stencil

(c) Selection of the appropriate runback side, in green

Figure 3.16 Selection of the next receiving facet

facets in the same direction of $\vec{C}_f$ is selected as the runback side. A facet is considered to be in the same direction of $\vec{C}_f$ if :

$$(P_{facet,i} - P_{facet,imp}) \cdot \vec{C}_f > 0 \quad \text{for} \quad i \in [1, N]$$

where $P_{facet,i}$ and $P_{facet,imp}$ are respectively the center the ith neighbor facet and the impinged facet. The vector $(P_{facet,i} - P_{facet,imp})$ is represented by the black arrows in Figure 3.16(c). This process is carried out only once, upon impingement, and the subsequent steps of the water motion follow the selected side.

Figure 3.16(c) illustrates this process for a stencil of four facets, but the number is higher (approximately twenty) and user-defined to ensure the robustness of the method.

3.7 Pseudo-Random Number Generator

The Chapel language provides a Permuted Linear Congruential Random Number Generator (PCG), implemented following the work of O'Neil [68]. It is an efficient PRN generation scheme providing good statistical properties (period, uniformity, and predictability) and leading to better quality PRNs (closer to real random numbers). Its key feature is the use of a permutation function to enhance the quality of a medium-quality PRN generator. More details on the PCG are available in [68].

Chapel implementation features the generation of integers and real numbers, and it is verified against statistical test suites used in the original implementation of O'Neil [49,68]. Therefore, the choice of this PRN generator is justified by its convenience (it is a standard library of Chapel) and the statistical quality of the generated PRNs.

3.8 Verification and Initial Results

The following section presents the verification of the developed proposed and initial results. The icing conditions for the selected cases are described in Table 3.1.

3.8.1 Verification of the Collection Efficiency

The collection efficiency obtained is verified to ensure that the stochastic process reproduces the deterministic impingement map. To that end, two cases are selected from the IPW [1]: cases 241 and 364. The collection efficiency is computed only on the initial front and no ice elements are generated to enable a direct comparison to the deterministic results of CHAMPS.

Table 3.1 Rime test cases input parameters

Test Case	Case 241 [1]	Case 364 [1]
Geometry	NACA23012	NACA0012
Chord [m]	0.4572	0.9144
Sweep [°]	0.0	30.0
AoA [°]	2.0	0.0
Mach [-]	0.325	0.354
Temperature [K]	255.2	259.8
Pressure [kPa]	92.5	89.6
LWC [g/m^3]	0.42	0.50
MVD[μm]	30.0	20.5
Icing Time [min]	5.0	17.7
k_s [m]	$1.0 \times 10^{-3}c$	$1.0 \times 10^{-3}c$

The collection efficiency for each front facet, $\beta_{i,stoch}$, is computed following its Lagrangian definition:

$$\beta_{i,stoch} = \frac{n_{i,imp}\, m_{cluster}}{\Delta t_{icing}\, \Delta s_i\, \text{LWC}\, U_{inf}}$$

Where :

- $n_{i,imp}$ is the number of times the front facet i is impinged.
- Δt_{icing} is the icing time in seconds.
- Δs_i is the area of the front facet in m (the length of the facet).
- U_{inf} is the norm of the free stream velocity in m/s.

The results for the two selected cases are presented in respectively Figure 3.17 and Figure 3.18.

The collection efficiency for case 241 is obtained from a monodisperse droplet size distribution where $d_{droplet}$ = MVD. Case 364 is a swept wing case (treated as 2.5D) and the experimental droplet size distribution, which can be found in Appendix A, is used for the presented results.

In both cases, the stochastic collection efficiency reproduces well the deterministic results while keeping its non-deterministic aspect. Furthermore, the agreement between the two frameworks allows verifying the treatment of the droplet size distribution.

However, in case 364, one can note little discrepancies around β_{max}, which are linked to the position of the stagnation point. Since the velocity $\vec{u}_d$ is taken from the RANS mesh cell

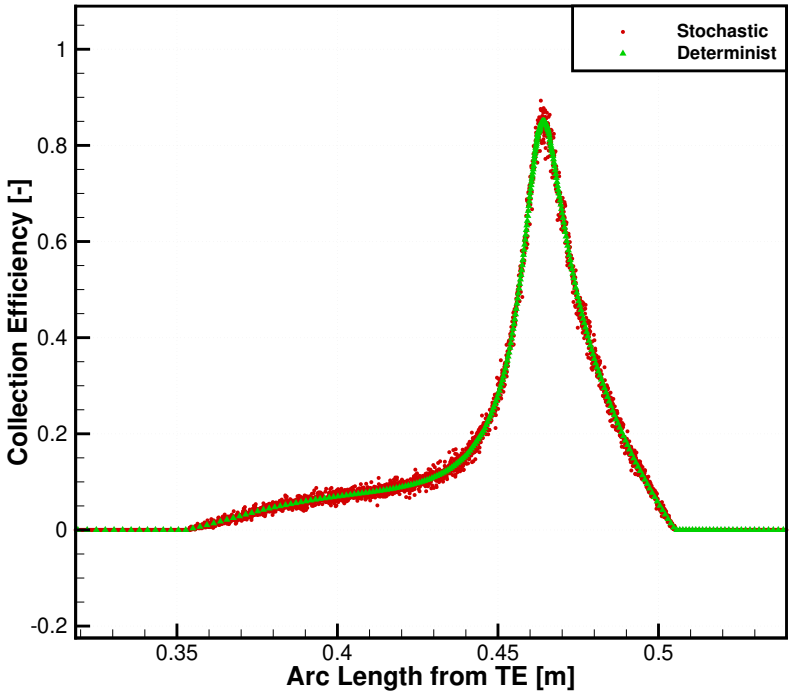

Figure 3.17 Verification of the collection efficiency for case 241. $\delta = 1.25 \times 10^{-4} c$.

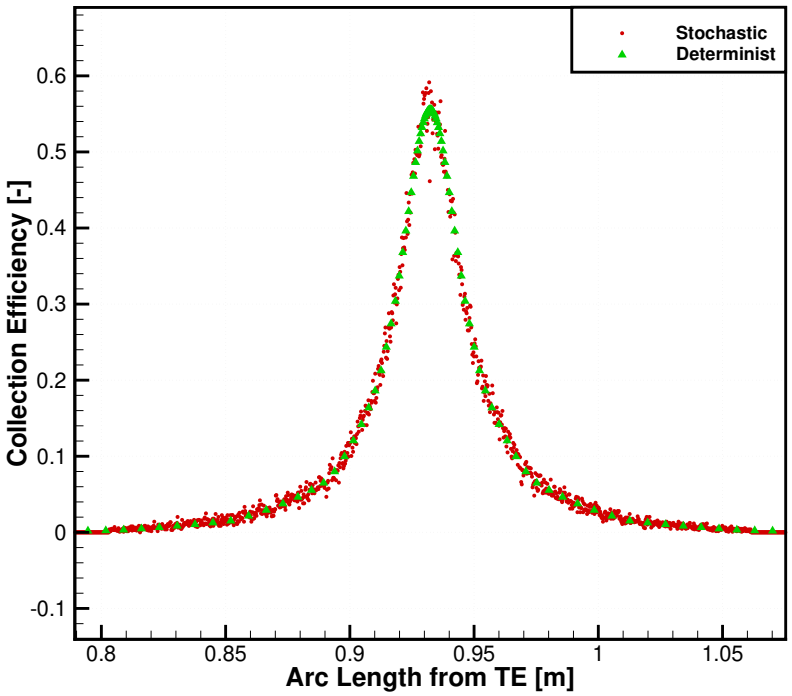

Figure 3.18 Verification of the collection efficiency for case 364. $\delta = 2.5 \times 10^{-3} c$.

that is currently crossed by a given droplet, its value in the neighbor cells is not taken into account. For example, in a symmetric case (as the case 364), on both sides of the stagnation point, the sign of the y-component of $\vec{U_d}$ changes. Therefore, if the RANS mesh is parallel to the streamlines at the stagnation point, i.e.,such as in a structured-type RANS mesh, the trajectory is unstable in this region, and the direction away from the stagnation point is preferred, creating a shadow zone. This situation is illustrated in Figure 3.19. If a front facet is in this shadow zone, it is not impinged by any cluster. It leads to a decrease in the collection efficiency at the stagnation point and an increase in the region on both sides.

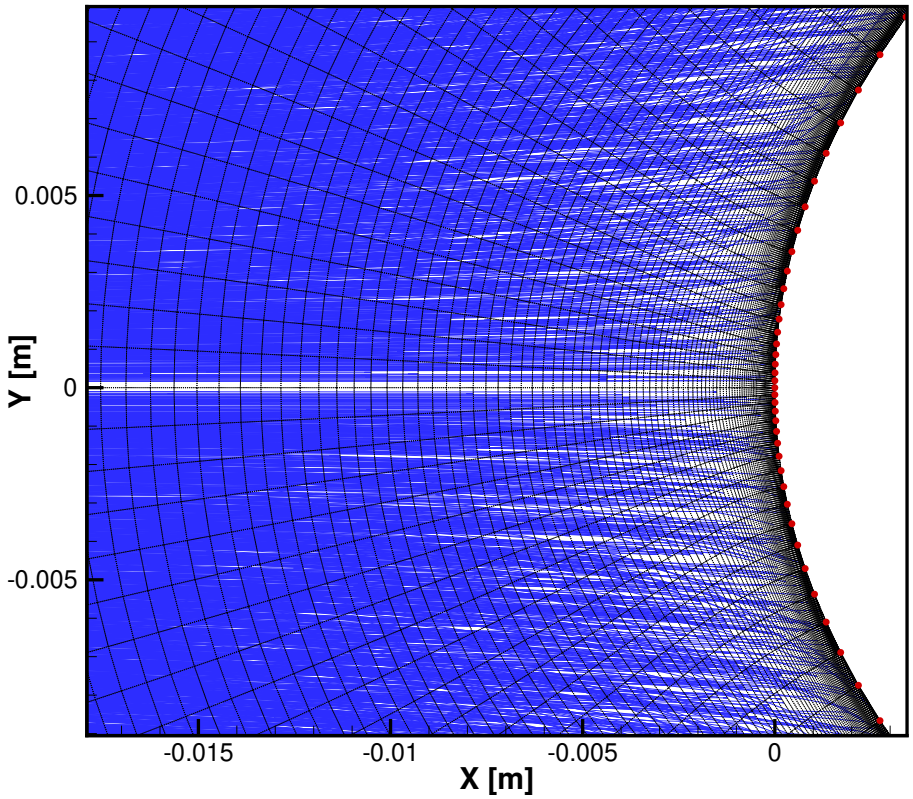

Figure 3.19 Limitation of the droplet trajectory computation. The trajectories are represented by the blue lines.

This corresponds to a limitation of the proposed approach. It can be mitigated with a refinement of the RANS mesh in the stagnation region or by the use of an unstructured mesh.

3.8.2 Element Size Effect

The effects of the element size, and therefore the cluster mass, are presented for case 241. The accretion time Δt_{icing} is set to 2.5 minutes to reduce the computational cost of this study. The convergence of the ice density according to the element size is also presented. The ice density is selected as the study parameter since it is a dependent variable in the framework, as proposed by Bourgault-Côté [3]. Furthermore, a rime ice case is selected because the ice density for glaze ice cases is usually constant at the bulk ice value.

The element size δ varies from $1.0 \times 10^{-3}c$ to $6.25 \times 10^{-5}c$ with a refinement factor of 2, where c is the chord length. The ice shapes obtained from one run for $\delta = 1.0 \times 10^{-3}c$ to $\delta = 1.25 \times 10^{-4}c$ are presented in Figure 3.20.

Ice Density Extraction

The obtained ice mesh is post-processed within Tecplot [69] to reproduce the extraction of a core sample of ice in experimental setups. The process is illustrated in Figure 3.21 and goes as follows:

1. A scalar D is set to 1 for all the ice elements of the stochastic mesh (represented in blue in Figure 3.21);
2. A fine Cartesian mesh of $N \times N$ cells (delimited by the black square in Figure 3.21) is overlaid on the stochastic mesh at the LE, and the scalar is set to 0 for each Cartesian cell (represented in blue in Figure 3.21);
3. The scalar D of the stochastic mesh is interpolated on the Cartesian mesh, using the linear interpolation available in Tecplot:
   - For the ice elements, the scalar in the corresponding cells of Cartesian mesh is 1 (blue in the zoom of Figure 3.21).
   - For the holes in the stochastic mesh, the scalar is not defined. Therefore, the scalar in the corresponding Cartesian cells mesh stays 0 (red in the zoom of Figure 3.21).
4. The sum of the scalar over the Cartesian mesh is computed and the ice density corresponds to :

$$\rho_{ice} = \frac{\sum_{i=1}^{N^2} D_i}{N^2} \cdot \rho_{ice,bulk}$$

Here, $\rho_{ice,bulk}$ is used as the density of a single ice element as described in Section 3.4.

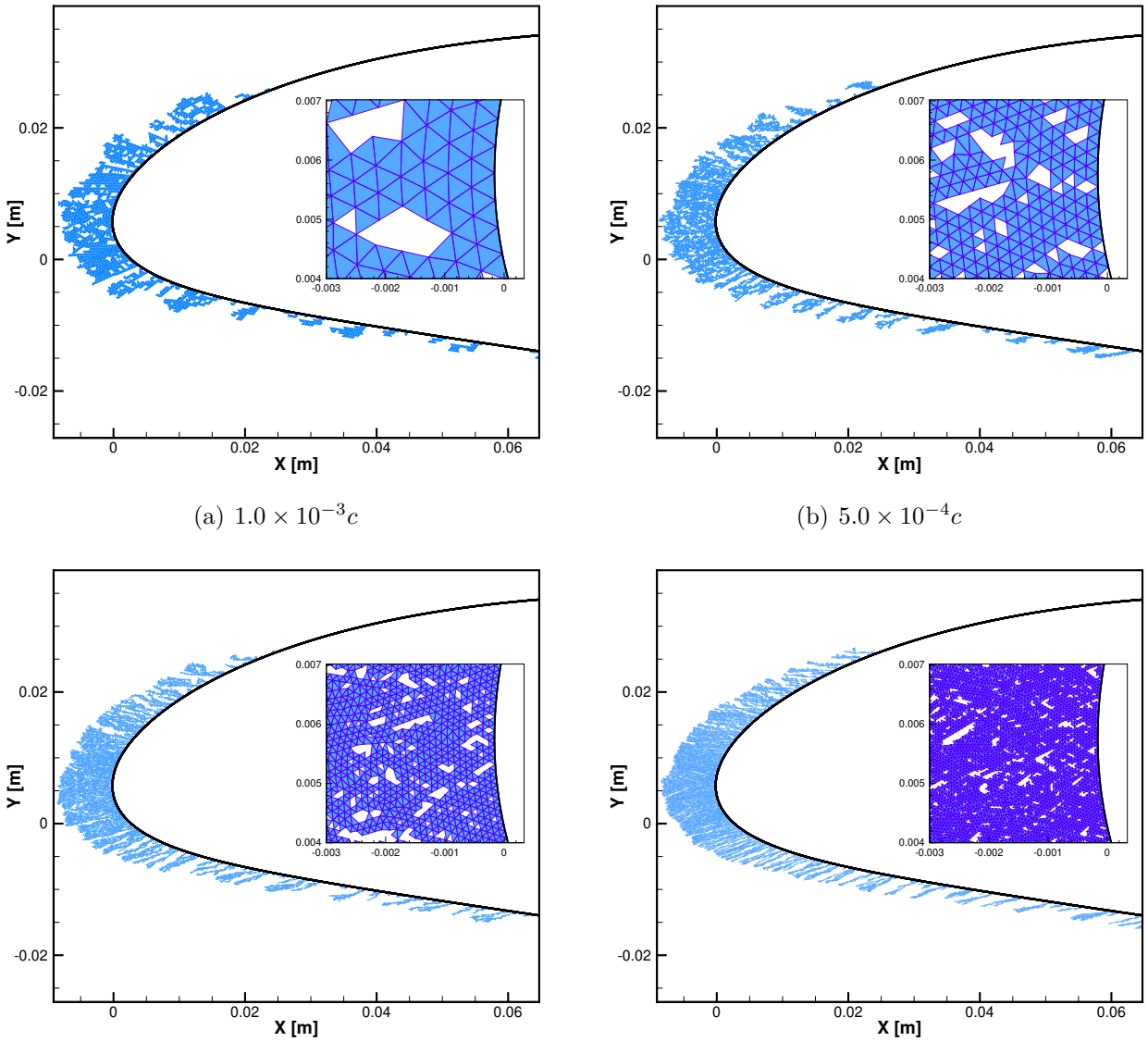

(a) $1.0 \times 10^{-3}c$

(b) $5.0 \times 10^{-4}c$

(c) $2.5 \times 10^{-4}c$

(d) $1.25 \times 10^{-4}c$

Figure 3.20 Element size effect on the ice shape

Ice Density Convergence Study

For each element size, five runs are performed and the average of the ice density is used to study its convergence. Since the exact density for this case is unknown, it is approximated to the ice density obtained from the finer stochastic mesh ($\delta = 6.25 \times 10^{-5}c$) : $\rho^*_{ice} = 753.81$ kg/m^3. The result is presented in Figure 3.22.

The 1st- and 2nd-orders of accuracy are presented in Figure 3.22 only for reference purposes; the observed order of the stochastic model is not of interest since there is no formal order

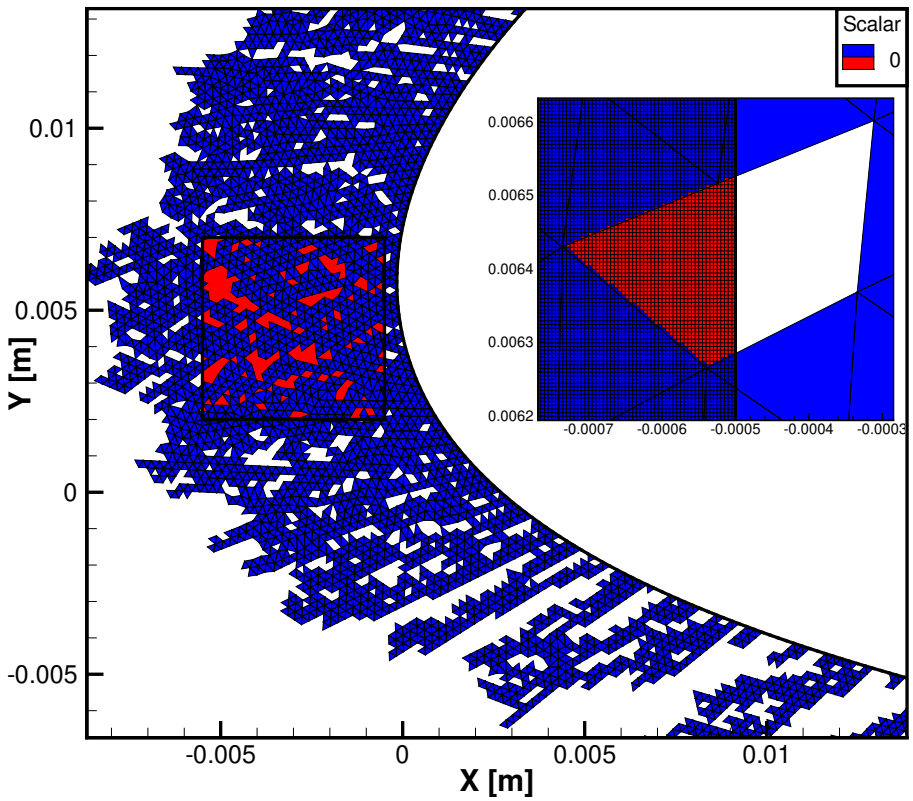

Figure 3.21 Extraction of the ice density from the stochastic mesh. The Cartesian grid is represented by the black square at the LE.

of accuracy for this process. Here, the important outcomes of this study is that the method converges.

3.8.3 Initial Results

Initial results on case 241 for the complete icing time are presented to introduce the following section.

Here, two conclusions are drawn from the comparison to the experimental and deterministic results:

- The ice thickness is overestimated;
- There are fine and long structures resembling ice feathers downstream of the main accretion.

Knowing that the ice density used in CHAMPS for the deterministic result is 820.0 kg/m^3 and

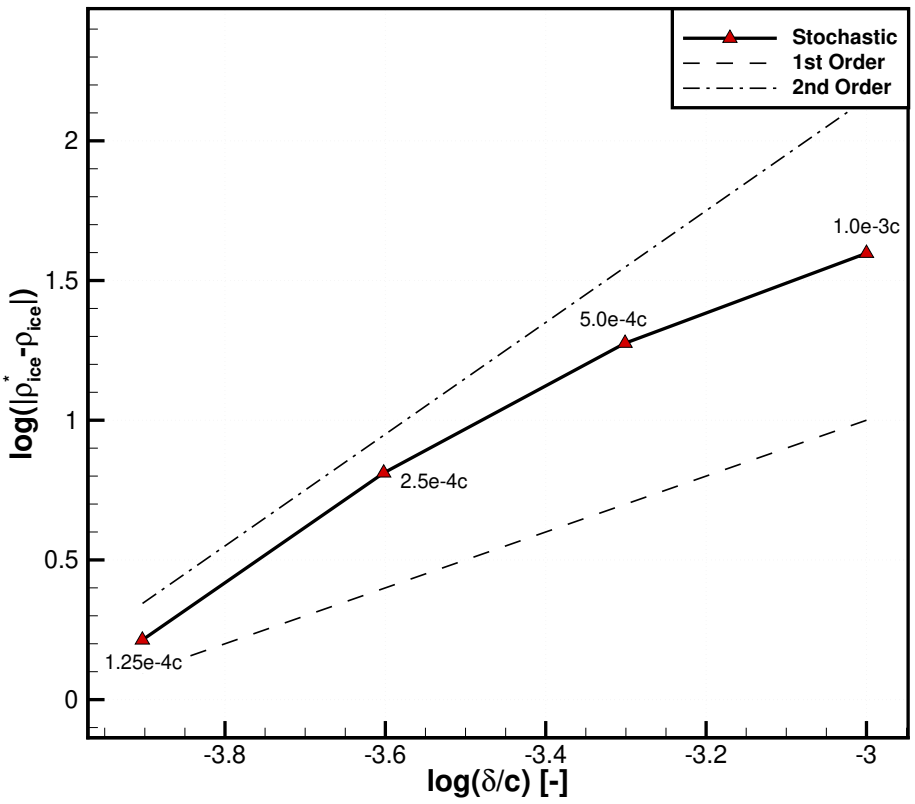

Figure 3.22 Ice density convergence study

that the stochastic ice density converges towards the value of 753.8 kg/m^3, the assumption that the ice density obtained from the stochastic method is too low for this case is raised. The same observation is made for the zones of feathers. In this case, the density is lowered by the void between the feathers. Furthermore, their formation seems to be numerically amplified. This observation is based on the following aspects :

- The feathers are long and thin.
- Once they are created, all the feathers grow at the same angle from the flow field.

While some of these features are expected for ice feathers (constant thickness, small spacing) [2], their general aspect suggests that their final shape and placement is mainly driven by their initialization.

Therefore, an extension of the present method is proposed in the following section to improve the results and complete the validation of the stochastic process.

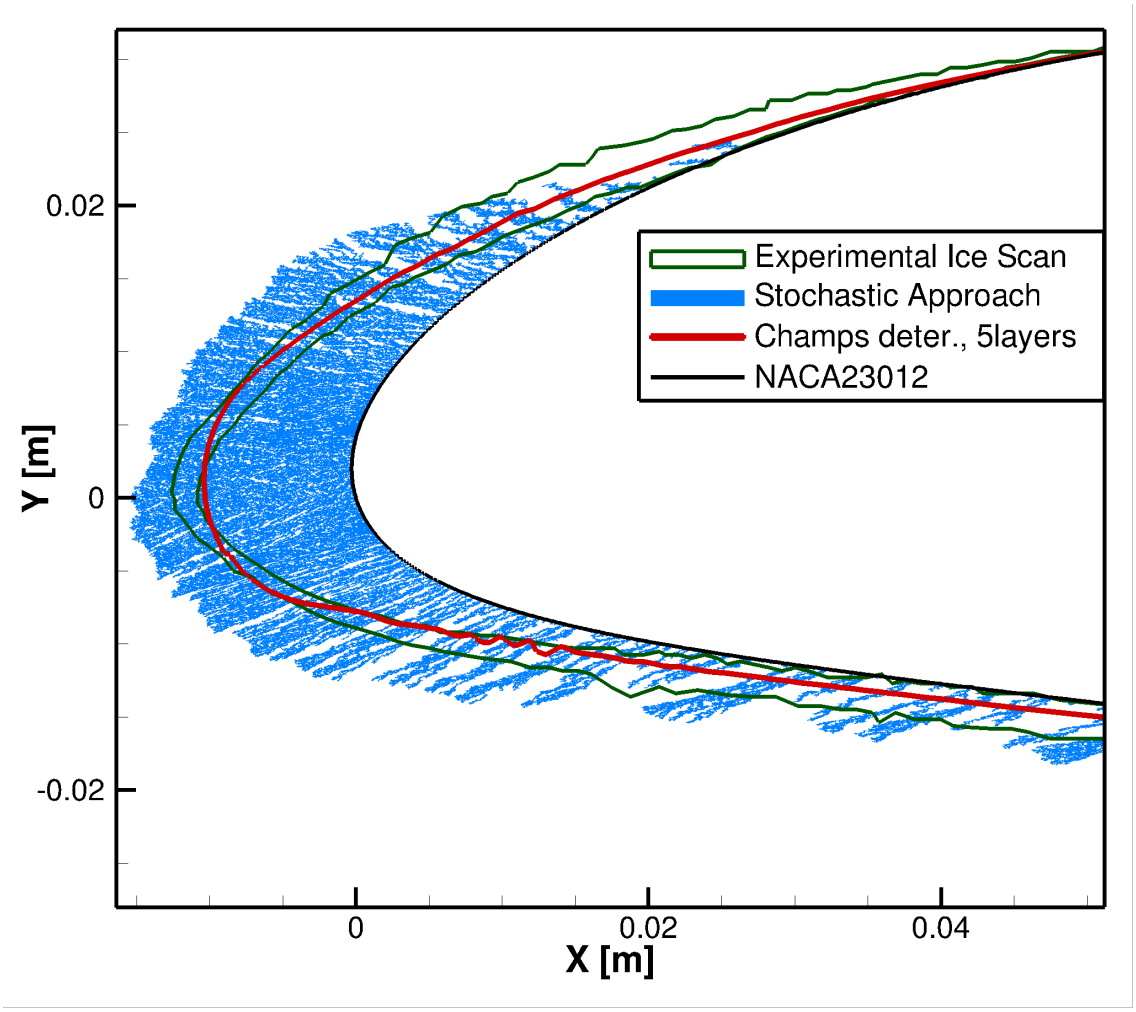

Figure 3.23 Initial results for case 241

3.9 Permeable Ice Front

Similar observations on the lower ice density are raised by Szilder, who proposed the cradle search to fill some of the created air pockets to obtain a denser ice, emulating the tendency of the water to fill gaps due to its surface tension [25, 39] (see Section 2.2.1). Unlike Szilder, the lower ice density obtained in the present method is assumed to be a result of the 2D framework. This assumption is based on the observation of the numerical and experimental ice shapes, mainly in the zones of feathers.

In a 3D reference frame, the ice shape varies within the spanwise axis (here referred to as the z-axis), as shown in Section 1.2.2. Thus, it is assumed that for two droplets seeded at the same position in the xy plane, but at slightly different positions along the spanwise axis, the impingement location can be significantly different.

To model this 3D mechanism in the proposed 2D framework, it is considered that the solution of the stochastic model for a given case is the set of the ice shapes obtained from different runs, referred to as outcomes. The resulting ice shape is therefore the overlay of these outcomes.

In the present framework, the outcomes are interpreted as 2D slices of the ice in the spanwise direction, as illustrated in Figure 3.24.

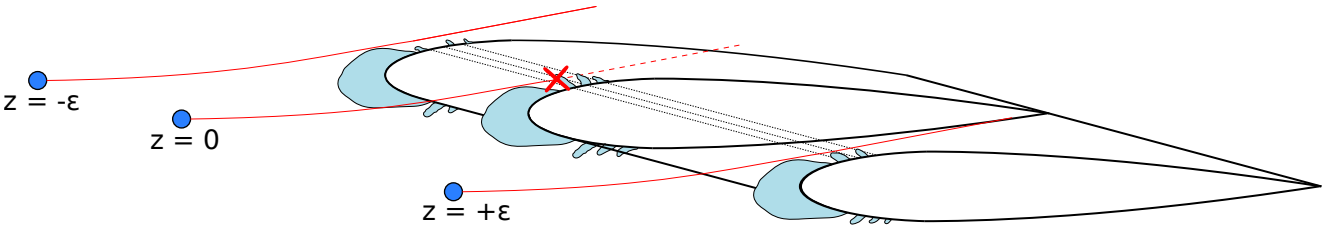

Figure 3.24 Interpretation of the outcomes in the spanwise direction and permeability of the ice front

At $z = 0 \pm \epsilon$ in Figure 3.24, $z = 0$ being the position of the current outcome and ϵ representing a small distance in the spanwise direction, the droplet may pass next to the feather and impinged further downstream on the neighbor outcome at $z = \pm\epsilon$, or shed if there is no other impingement location. Therefore, the concept of a permeable ice front is introduced.

The permeable ice front consists in allowing that a fraction of the clusters impinges behind the main ice front. A given cluster can either :

1. impinge on the main ice front;
2. impinge on an air pocket front;
3. be shed.

The fraction of clusters passing through the front is controlled by a stochastic process.

If the cluster passes through the main front to impinge on an air pocket front or to be shed, it continues its trajectory for a given distance d_{max}. Therefore, from the first intersected front facet, the process is illustrated in Figure 3.25 and goes as follows for each seeded cluster:

1. Compute the distance d between the current intersection and the first intersected front facet and generate a uniform PRN (0 or 1);
2. **If** PRN = 1 and $d \leq d_{max}$, the current facet is the impinged facet. Continue to the thermodynamic module;

3. **Else** if PRN = 0 and:

   - $d \leq d_{max}$, compute the next intersection between the trajectory and a front facet facing upstream ($\vec{n}_{facet} \cdot U_d < 0$), and return to step 1;
   - $d > d_{max}$, the cluster is shed. Break (treat the next cluster).

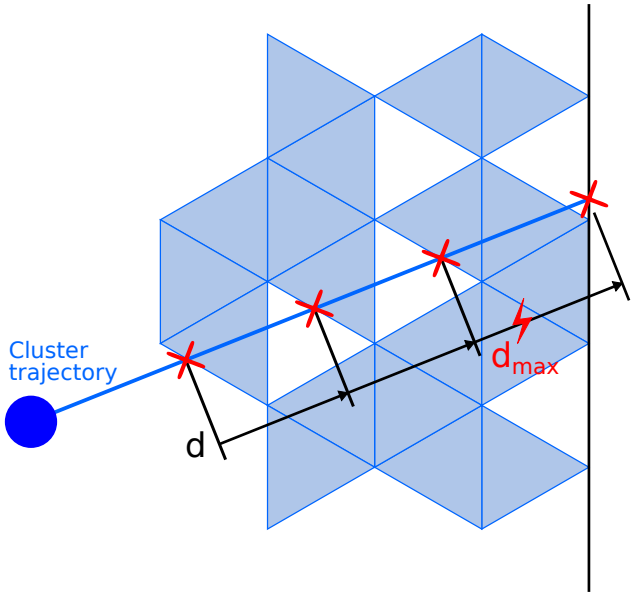

Figure 3.25 Process to emulate the permeability of the ice front

In the event that the cluster is shed, it is considered to be impinged on the neighbor outcome at $z = \pm\epsilon$, and therefore its mass is not taken into account in the stop criterion presented in Section 3.4.2.

Here, the parameter d_{max} is not physically representative and it requires to be calibrated. However, the higher it is, the denser the ice is.

It is important to note that this process needs further developments to ensure the convergence of the process and its validity. However, it is presented here to show that the extension of this stochastic model is required in future works to capture important physical phenomena that are missed in the 2D framework.

CHAPTER 4 ICING RESULTS

This chapter presents the results of the proposed method on four test cases from the literature to assess its capability to model the ice accretion phenomenon. For each case, the numerical ice shapes of multiple runs are compared against the experimental results. Additionally, the comparison to the deterministic approach single- and multi-layer ice shapes for the selected cases is discussed.

4.1 Rime Ice Conditions

The two rime ice cases presented in Table 3.1 for the verification of the implementation are studied in this section. They are selected due to the availability of the experimental ice shape scans [1], which give an insight of the variations of the ice in the spanwise direction and the envelope of the experimental results.

For the NACA23012 geometry (case 241), an unstructured grid is used based on the wind-tunnel geometry provided by the IPW committee [1] with a total of 68000 cells. The airfoil and the wind tunnel walls are respectively discretized with 778 and 198 vertices, as presented in Figure 4.1. For the NACA0012 geometry (case 364), the RANS mesh used is a structured O-type grid and has 385 vertices in the i direction and 257 in the j direction.

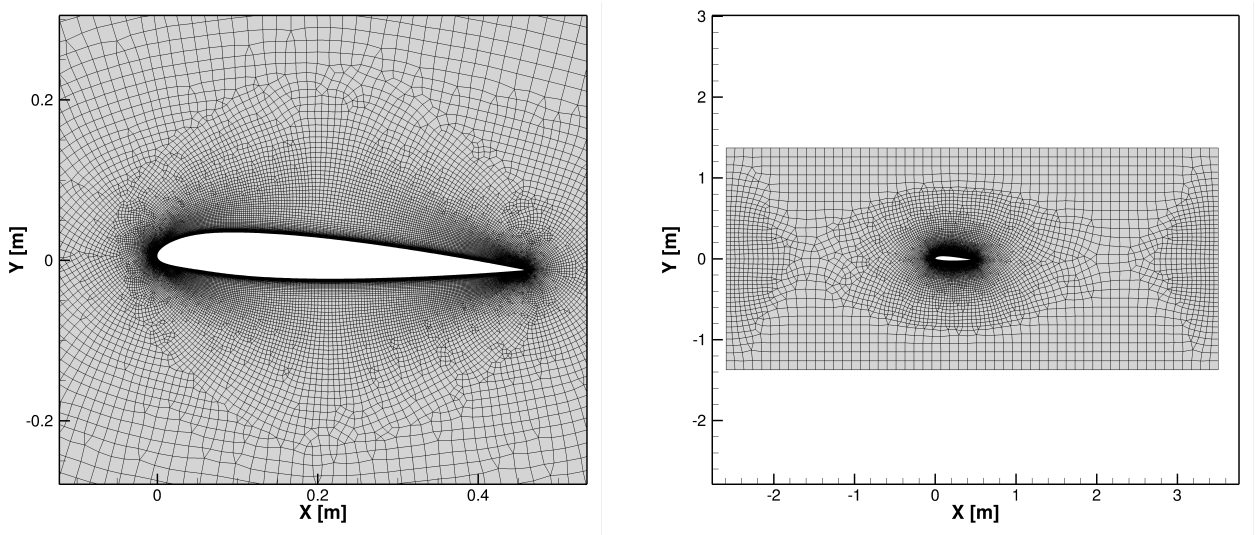

(a) Airfoil discretization

(b) Wind tunnel walls discretization

Figure 4.1 NACA23012 RANS mesh

4.1.1 Case 241

Case 241 [1] is performed for an element size of $\delta = 2.5 \times 10^{-4}c$ and for $d_{max} = 2.0 \times 10^{-3}c$. The experimental droplet size distribution is used, which can be found in Appendix A. The results are shown for five outcomes in Figure 4.2. The outcomes are overlaid and the grayscale represents the likelihood of the results: the darker the area is, the higher the probabilities are to have ice in this region. The grayscale is obtained by setting the opacity of each ice shape to 20% to highlight the zone of higher variability. Note that for clarity purposes, only the ice front for each outcome is presented in Figure 4.2; the air pockets within the ice are not represented. The light blue zone represents the variation of the experimental scan over the entire span, projected in the xy plane.

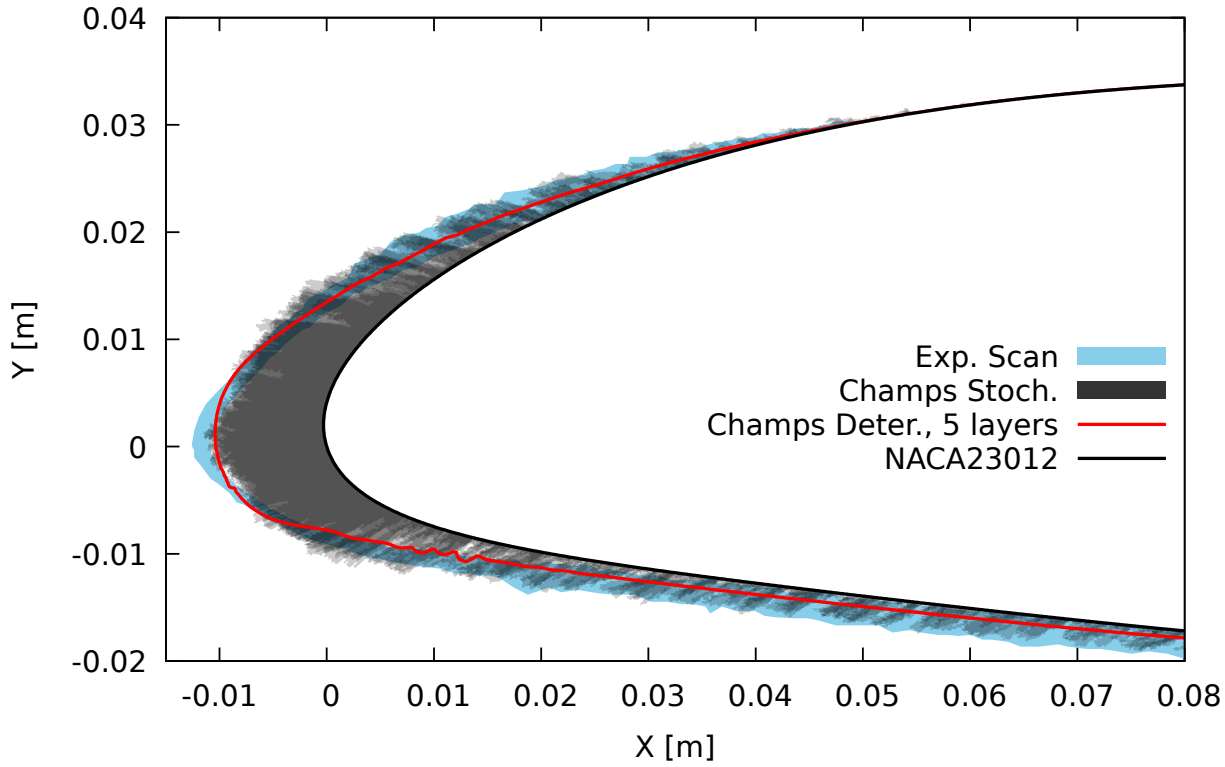

Figure 4.2 Results for case 241

The ice shape obtained with the stochastic method is in good agreement with the expected results. The ice thickness at the LE corresponds to the experimental ice shape, despite a small discrepancy. The stochastic method captures the tapered shape of the scan, while the deterministic 5-layers result of CHAMPS presents a rounder shape.

The ice thickness downstream, on the lower and upper surfaces, corresponds to the experi-

mental envelope, and the ice limits are well respected, as presented in Figure 4.3, where the only one outcome is shown.

Additionally, one can observe more variability on the lower and upper surfaces, in the area where feathers are observed. This is expected since the feathers in experimental setups appear at random positions, behind the main ice accretion [17]. It is also observed in the scan of the experimental ice shape: the scan envelope in Figure 4.2 is thicker, meaning that there is more variability between the maximum and minimum ice heights in the spanwise direction for those zones. Therefore, the stochastic method captures these variations, whereas the deterministic framework mainly leads to a smooth ice shape.

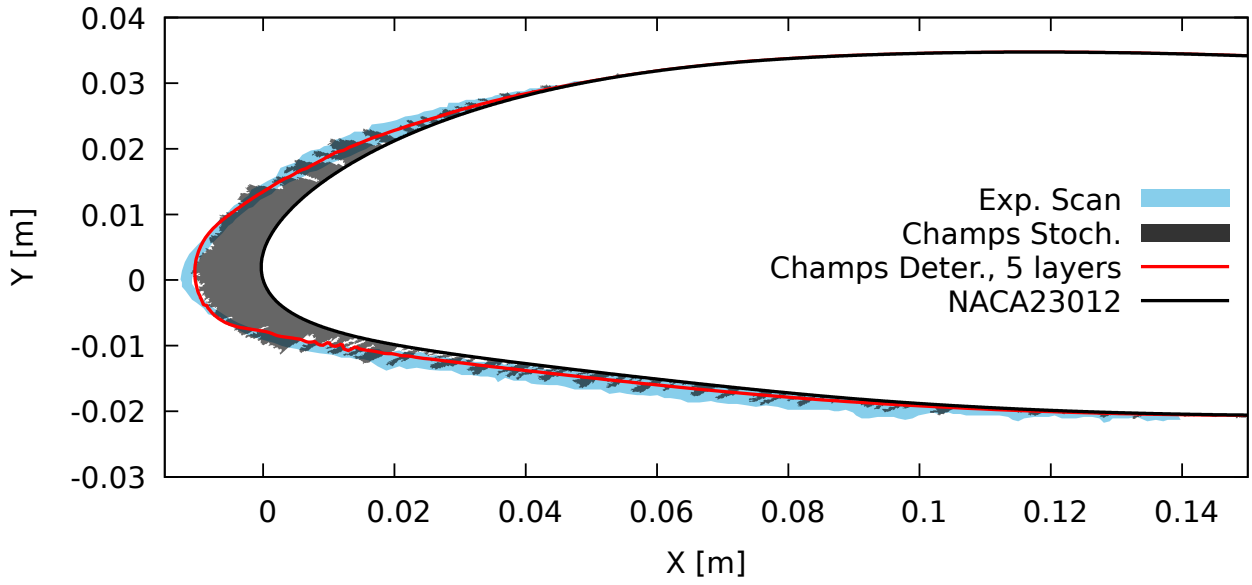

Figure 4.3 Result of one outcome for case 241

Sensibility to d_{max}

The sensibility of the ice shape to d_{max} is presented in Figures 4.4 and 4.5 for case 241. The values tested range from $5.0 \times 10^{-4}c$ to $3.2 \times 10^{-2}c$, with a scaling factor of 2.

The results show that as d_{max} increases, the ice is denser, as expected. Additionally, the feathers observed on the lower and upper surfaces are thicker and shorter for higher values of d_{max}. Furthermore, they grow closer to each other. While most of the studied values lead to ice shapes in the expected range, there is no physical meaning associated with them. For the values of $5.0 \times 10^{-4}c$ to $4.0 \times 10^{-3}c$, the ice thickness at the LE is in better agreement

with the ice scan than for the higher values, and the overall feather shape represents the expected behavior. However, the height of the feathers is in better agreement with the ice envelope for the values of $8.0 \times 10^{-3}c$ to $1.6 \times 10^{-2}c$. It suggests that the proposed extension of the method with the permeable front needs to be properly calibrated. Another avenue is to extend the original framework in 3D to take into account the spanwise component of the ice porosity and the feather formation.

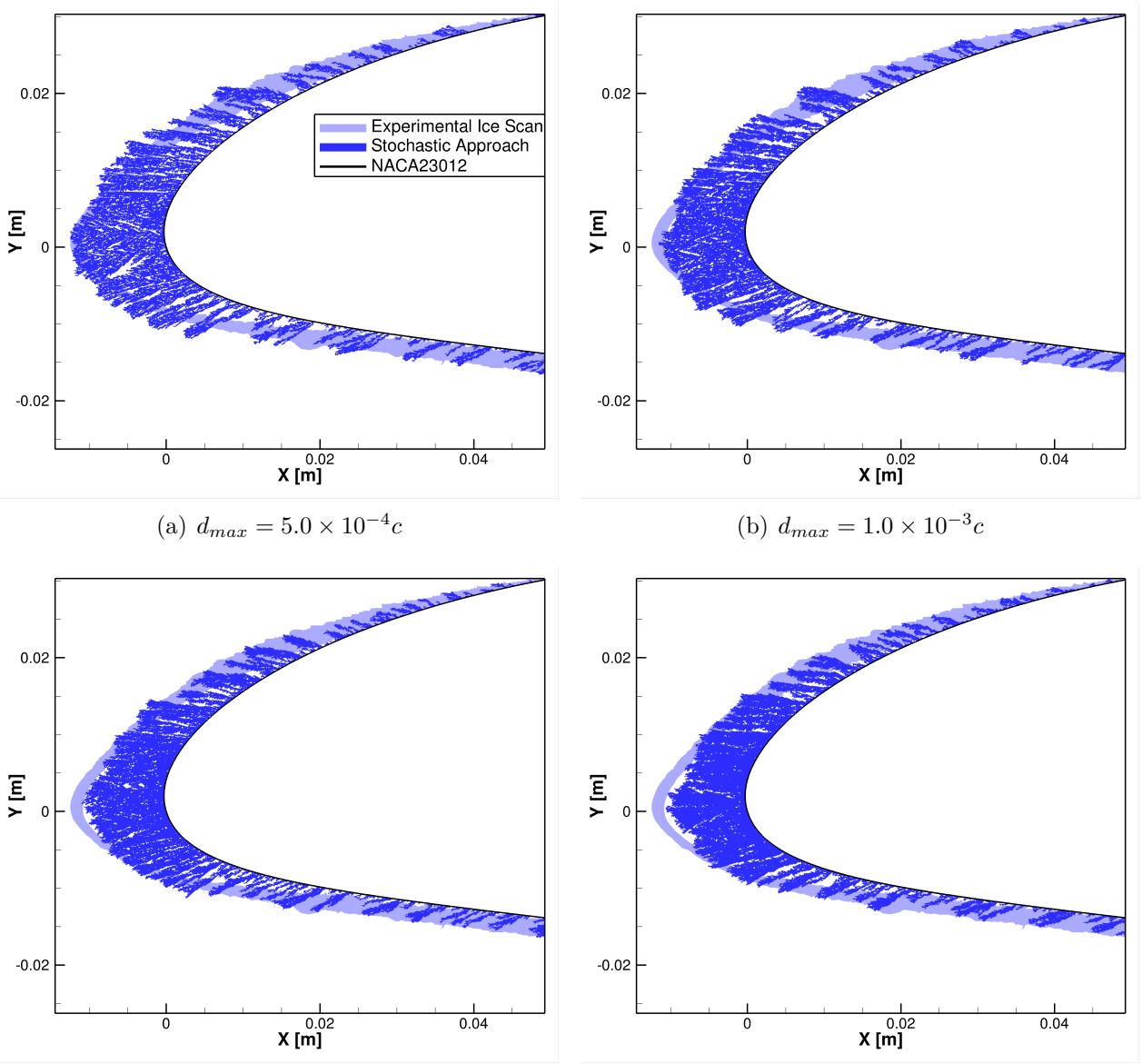

(a) $d_{max} = 5.0 \times 10^{-4}c$

(b) $d_{max} = 1.0 \times 10^{-3}c$

(c) $d_{max} = 2.0 \times 10^{-3}c$

(d) $d_{max} = 4.0 \times 10^{-3}c$

Figure 4.4 Effect of d_{max} on the ice shape

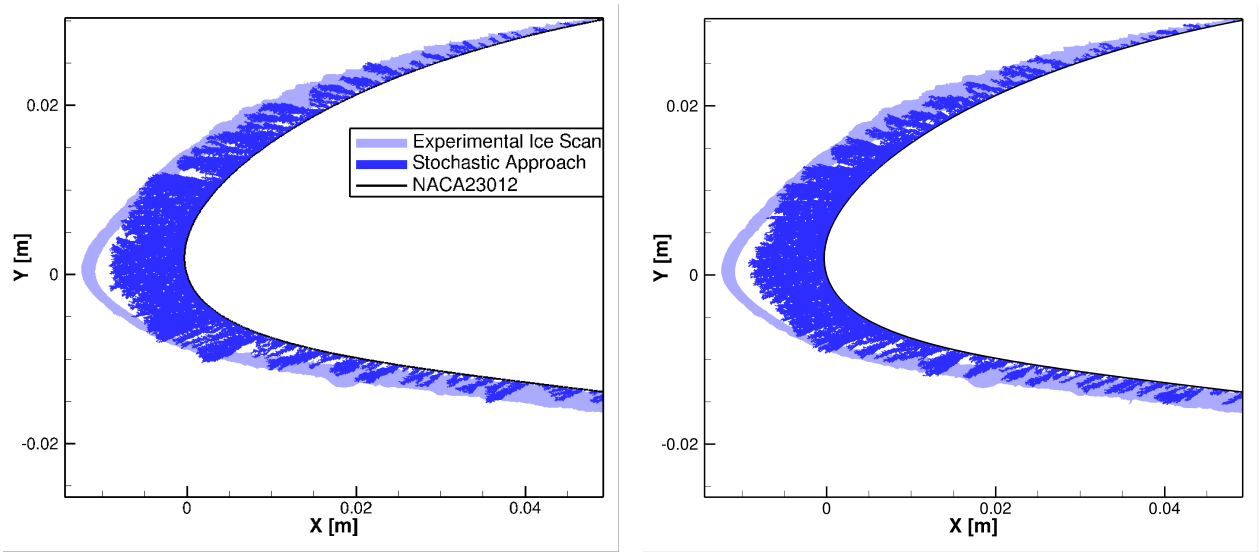

(a) $d_{max} = 8.0 \times 10^{-3}c$

(b) $d_{max} = 1.6 \times 10^{-2}c$

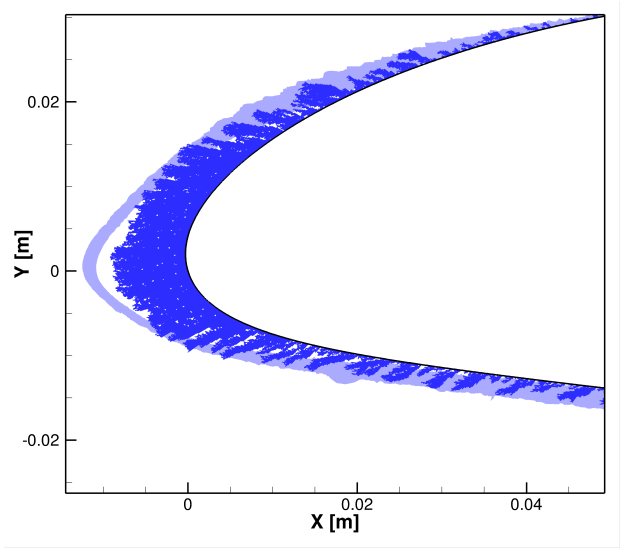

(c) $d_{max} = 3.2 \times 10^{-2}c$

Figure 4.5 Effect of d_{max} on the ice shape (continued)

4.1.2 Case 364, 2.5D

Case 364 [1] is a swept wing case and is performed for an element size of $\delta = 2.5 \times 10^{-4}c$ and for $d_{max} = 1.0 \times 10^{-3}c$. The experimental droplet size distribution is used, which can be found in Appendix A. The flow and droplet fields are resolved using the 2.5D approach implemented in CHAMPS, as described in [4]. The results for five outcomes are presented in Figure 4.6.

The variability in the feather zone, downstream of the main ice accretion, observed in the

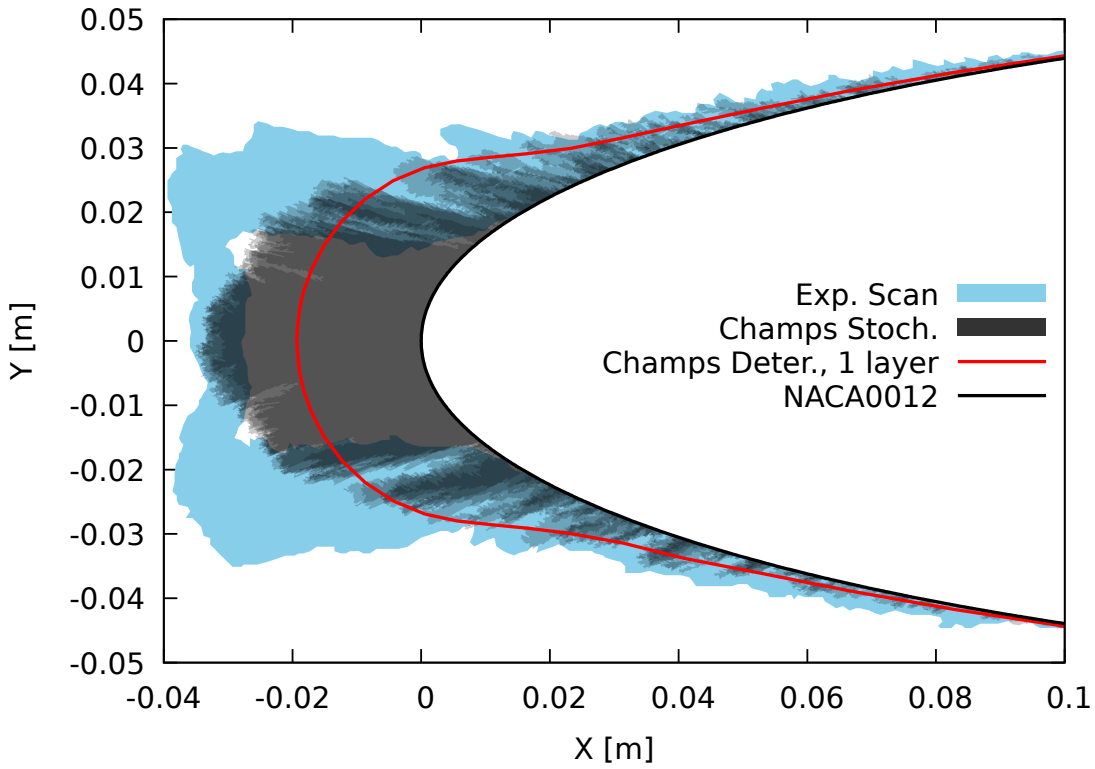

Figure 4.6 Results for case 364

experimental ice scan, is well captured by the stochastic approach, as well as the ice limits. Individual feathers are obtained, as observed in the experimental scan, while the deterministic approach results in a smooth ice shape.

Figure 4.7 shows the ice shape for only one run. The angle at which the main ice accretion grows corresponds to the scan envelope. Furthermore, the ice height at the LE is in good agreement with the experimental shape. However, the horn-like structures are not captured. It suggests that there is runback water not captured by the Iterative Messinger model in a single-layer framework.

While the stochastic approach does not capture properly the entire ice shape, it is in better agreement with the expected range compared to the deterministic single-layer result of CHAMPS.

Additionally, Figure 4.7 depicts well the geometry of the feathers generated by the stochastic approach. As expected, they appear at discrete and random locations [17]. Their height is also variable and respects the experimental envelope. The prediction of such discrete structures is in agreement with the experimental observation [2] and enables to further the

numerical investigations of their formation and effects, where the deterministic and continuous frameworks fail. It is important to remind that the results of the stochastic method are obtained from only one resolution of the flow and droplet fields, showing an advantage of the piecewise accretion framework compared to the deterministic and continuous single layer approaches.

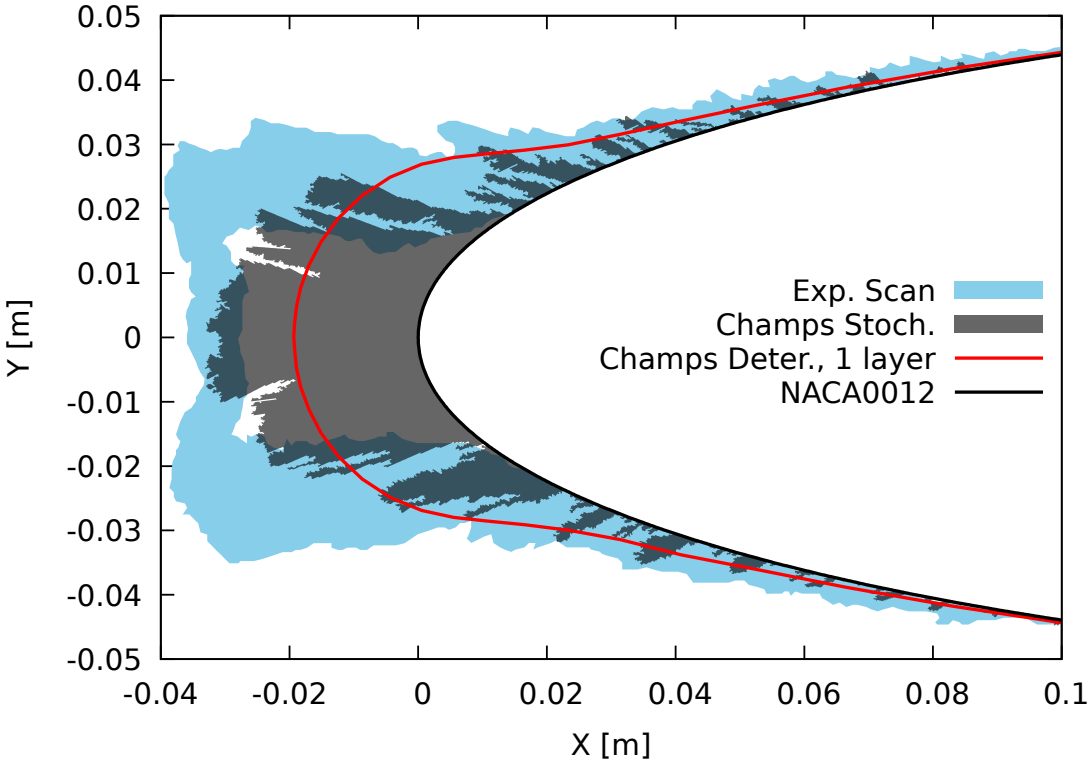

Figure 4.7 Result of one outcome for case 364

4.2 Glaze Ice Conditions

This section presents two glaze ice cases. The icing conditions are described in Table 4.1. The RANS meshes presented in Section 4.1 are re-used for these cases.

4.2.1 Case 04 Trontin, Glaze

Case 04, presented by Trontin et al. [6], is performed for an element size of $\delta = 2.5 \times 10^{-4} c$ and for $d_{max} = 8.0 \times 10^{-3} c$. A monodisperse droplet size distribution is used for the droplet trajectory computations since the experimental data is not available. The results of five outcomes

Table 4.1 Glaze test cases input parameters

Test Case	Case 04 [6]	Case 242 [1]
Geometry	NACA0012	NACA23012
Chord [m]	0.5334	0.4572
Sweep [°]	0.0	0.0
AoA [°]	4.0	2.0
Mach [-]	0.314	0.310
Temperature [K]	262.3	265.7
Pressure [kPa]	101.3	92.9
LWC [g/m^3]	0.6	0.75
MVD[μm]	15.0	15.4
Icing Time [min]	6.4	5.0
k_s [m]	$1.0 \times 10^{-3}c$	$1.0 \times 10^{-3}c$

are presented in Figure 4.8 and compared to two deterministic approaches : CHAMPS and IGLOO2D [6]. The results of the latter are obtained from its predictor/corrector framework.

The height and angle of the upper horn are well captured by the stochastic method, as well as the ice limits. However, the lower horn is not predicted. Additionally, the ice thickness at the LE is overestimated.

As the horn position and thickness are mainly controlled by the runback water, it is assumed that the Iterative Messinger model does not well predict the water film behavior on the lower surface. This observation is confirmed by the deterministic ice shape obtained from CHAMPS in single layer (represented by the red curve in Figure 4.8): while there is a horn-like structure developed on the upper surface, it misses the horn on the lower surface. It suggests that an extension of the stochastic method to enable multi-layer simulations is required to better predict the zone where there is runback water. Care must be taken looking at the ice shape of the predictor step of IGLOO2D since a variable ice density model is used.

Finally, the variability of the ice shape is observed mainly on the lower surface and near the ice limit on the upper surface. Again, feather structures are observed, which are also expected for glaze ice cases [2].

4.2.2 Case 242 IPW, Glaze

Case 242 presented at the IPW [1] is performed for an element size of $\delta = 2.5 \times 10^{-4}c$ and for $d_{max} = 8.0 \times 10^{-3}c$. The result of a single outcome is represented in Figure 4.9 by the solid blue curve and compared to the same five experimental trials presented in Figure 1.3.

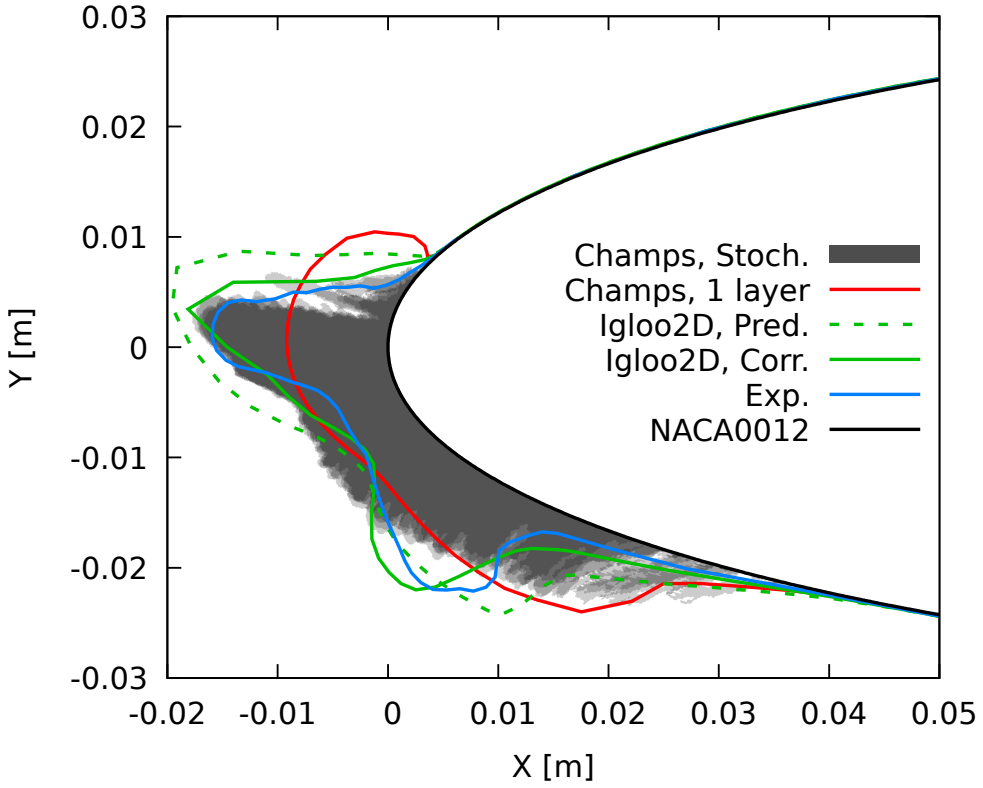

Figure 4.8 Results for case 04

These results are overlaid and the blue-scale depicts their likelihood.

Here, only one outcome is presented since no significant variation of the obtained ice shapes is observed within the different runs performed. However, the experimental results show great variations in the shape of the horns, as presented in Figures 1.3 and 4.9. It suggests that the variability observed in the icing phenomenon does not only come from the stochastic structure of the cloud and the investigation of other sources of randomness, such as the stochastic nucleation, the distribution of surface imperfections, and the experimental uncertainty is required to assess their effect on the numerical ice shapes.

Despite the observed experimental variability, the position and angle of the horns, as well as the ice limits follow the same trends. Additionally, the ice thickness in the stagnation region is mainly constant. Therefore, these parameters are used for the following analysis of the numerical results.

The two horns are well captured, as for their position and angle. However, their height is underestimated, as well as the accreted ice mass. The ice limits and the ice thickness in the stagnation region are in the expected range.

Figure 4.10 compares the obtained ice shape to the results presented by the other participants of the IPW [1]. The solvers used by the participants are deterministic and continuous frameworks with multi-layer or predictor/corrector capacities to take into account the growth of the ice. The ice shapes obtained for case 242 are the most scattered results of the workshop. In addition to the ice limits being further downstream of the experimental limits, the horns are mainly under-developed and there is a significant offset in their position. Care must be taken when looking at individual results, as some participants used tuned variable density or surface roughness models.

Interestingly, the stochastic method succeeds at once to capture the ice limits and the position of the horns, while only resolving once the flow and droplet field, as well as the thermodynamic exchanges. This suggests that for this case, the small differences in the geometry at the beginning of the icing time have a great effect on the final ice shape.

The stochastic method is able to capture these small differences because it captures a smaller time scale of the phenomenon by accumulating the ice one element at a time. Therefore, the Lagrangian framework can be interpreted as a smaller time step compare to the multi-

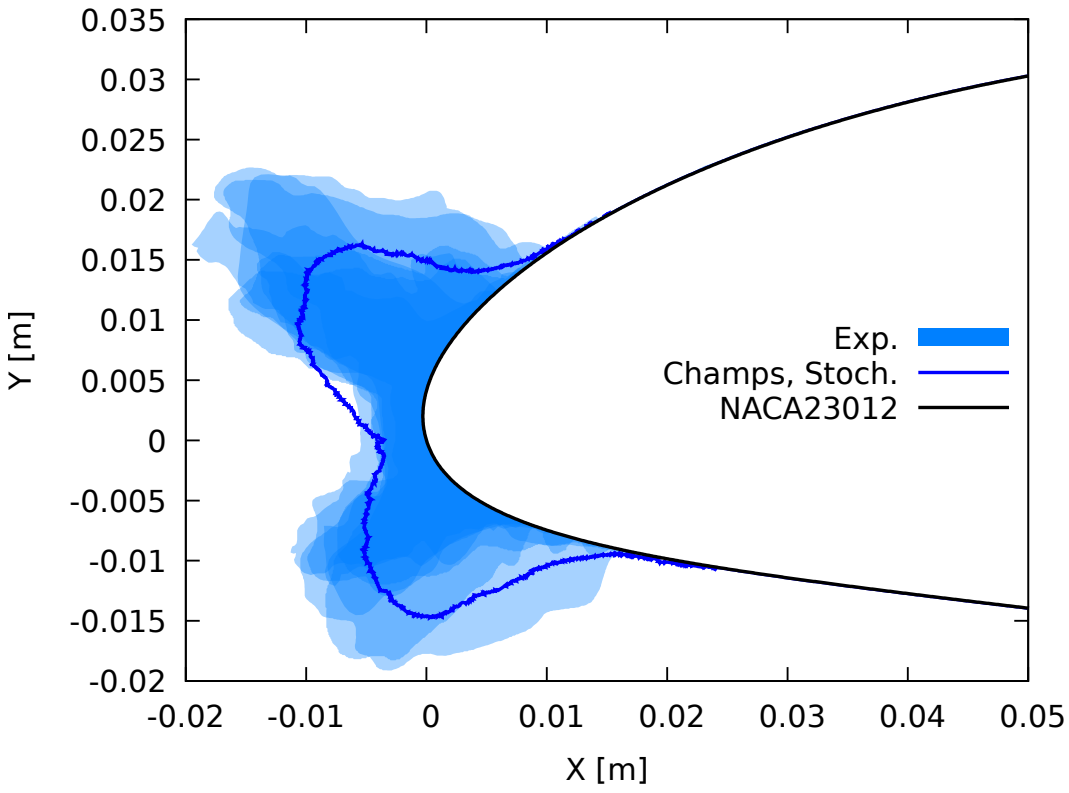

Figure 4.9 Results for case 242

layer continuous methods. This allows to model the associated shadow zone and predict the right limits of ice, while the multi-layer frameworks miss them. It can be assumed that if a sufficiently small time step is used at the beginning of the icing time in the multi-layer frameworks, this phenomenon could be accurately captured, but it could also lead to greater computational costs.

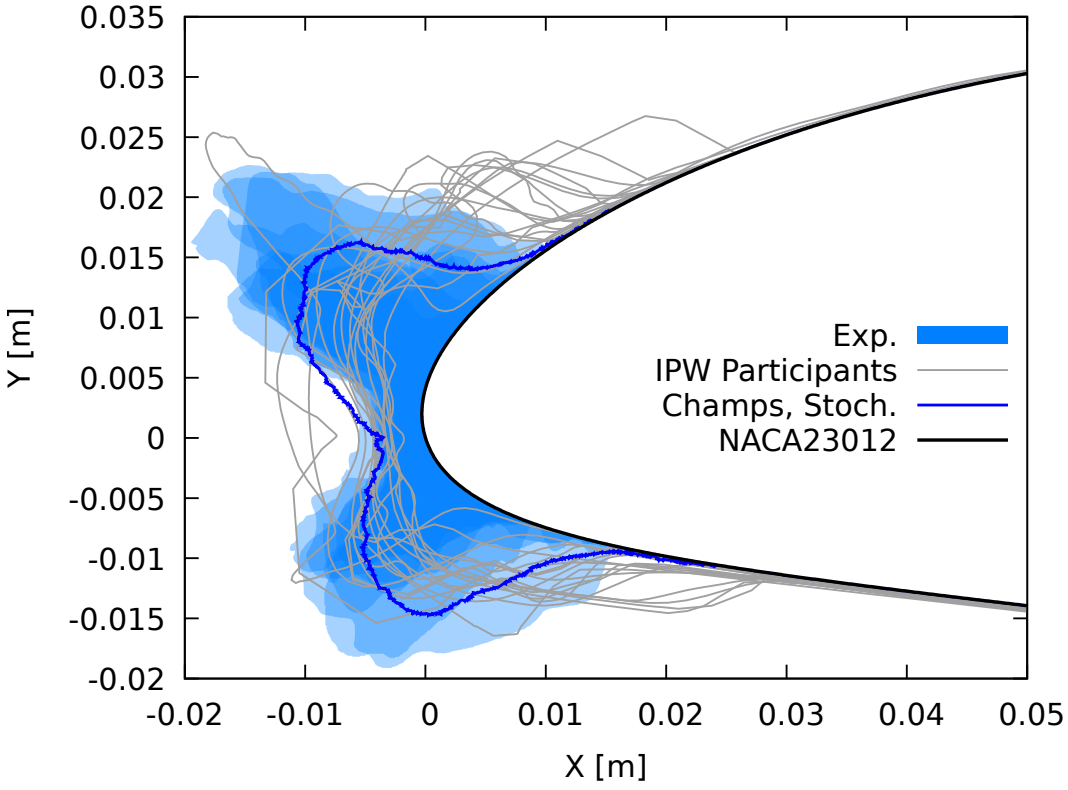

Figure 4.10 Results for case 242 compared to the participants of the IPW [1]

CHAPTER 5 CONCLUSION

5.1 Summary of Works

The overarching objective of the present research project is to model stochastic ice shapes and discrete ice structures by developing a non-deterministic 2D framework for numerical simulations of the in-flight ice accretion phenomenon.

The first sub-objective is to model rime and glaze icing conditions. An unstructured advancing front mesh generator is proposed to model the ice growth, enabling a body-conforming method. The developments are implemented in the new CFD solver CHAMPS. The framework is Lagrangian: the water droplets, gathered in clusters, are treated sequentially, from their injection in the computational domain to their freezing on the studied geometry. The trajectory of each cluster is computed using the extraction of its streamline from the droplet velocity field obtained with an Eulerian droplet solver. The intersection between the trajectory and the ice front corresponds to the impingement location. Upon impact, the droplet either freezes or flows on the front to freeze further downstream, depending on the thermodynamic state obtained from an Iterative Messinger model. The orientation of runback water is obtained from the shear stress direction of the nearest RANS surface cell. When the cluster freezes, a new element of ice is generated with the unstructured advancing front mesh algorithm. Partial freezing of the cluster is allowed in the case of glaze ice conditions, leading to the prediction of ice horns in this single-layer framework. The ice shapes obtained for two glaze ice cases are presented and compared against the experimental and deterministic results. The position and angle of the horns are well captured, while some discrepancy in the height is observed for one case. The stochastic model is also validated against two rime ice cases for 2D and 2.5D geometries. The predicted ice thickness at the LE corresponds to the experimental shape, as well as the ice limits, and the overall ice shape is within the expected range for both cases.

The second sub-objective is to capture the variability within the ice shape for multiple trials of the same conditions. Stochasticity is introduced in two modules of the process: i) in the droplet trajectory computations and ii) in the permeable front technique. The initial position of the droplet is randomly generated on a seeding plane using a uniform PRN. The droplet size is randomly obtained with the inverse transform sampling method, using the experimental droplet size distribution. The variation of the ice shape in the spanwise direction is taken into account using an original technique, allowing the droplets to randomly cross the ice front over a given distance. For three test cases out of the four presented, five

trials are performed, and the variability in the ice shape is obtained, mainly in the zones where feathers are observed, corresponding to the experimental envelope.

The third sub-objective is to capture variable ice density and discrete ice structures. The ice density variation according to the element size is studied within the verification of the model. Additionally, stochastic and discrete ice structures, referred to as feathers, are observed in the stochastic ice shapes of the presented test cases and are in good agreement with the experimental results.

5.2 Limitations

The limitation identified throughout the previous chapters are listed below:

- The droplet trajectory computations lead to a diminution of the collection efficiency in the stagnation point region when the RANS mesh is parallel to the streamlines in this zone. This limitation results in an impossibility to impinge the facets of the active front in this region.
- The proposed method corresponds to a single-layer framework. Although the ice growth is taken into account in the impingement location computations, the flow field is not updated as the geometry evolves. This limitation has two main effects :
    1. The changes in the HTC and the associated thermodynamic exchanges are not computed. As a result, ice horns could be not captured due to a wrong prediction of the thermodynamic state (rime or glaze).
    2. The shear stress is kept constant at the clean geometry value, leading to a wrong approximation of the runback water direction, mainly at the tip of the horns.
- The stochasticity is mainly introduced through the droplet trajectory computations. However, the variations in the overall geometry of the horns observed in experimental results are not captured by the stochastic model. The ice shape variability obtained is limited to the zones where feathers are observed.
- The extension of the model with the permeable front technique is based on the observations made from the initial results. The assessment of its validity is limited to the predicted ice shapes being in the expected range.
- The model is limited to 2D or 2.5D geometries. Highly 3D ice structures can not be obtained with the proposed method, such as scallops presenting significant variability in the spanwise direction.

5.3 Future Research

In light of the presented limits of the model, the following research topics are suggested to enhance the icing phenomenon understanding:

- An extension of the model to a multi-layer framework represents the main recommendation. This leads to the need for an ice front extraction and treatment to enable the generation of a valid volume mesh. It could include the local surface irregularities as the surface roughness in the subsequent ice layer computations to take into account the observed ice shape variability.
- The effects of other sources of stochasticity could be introduced to enable the prediction of variable horn shapes. In particular, the freezing process could be extended to be non-deterministic by studying the impact of the local irregularities of the ice front on the thermodynamic exchanges.
- Furthermore, a local model to better capture the way the water droplets impinge and fill the porous ice front could be added to the permeable front technique, leading to physical foundations for the proposed extension instead of the presented heuristic thinking.
- Finally, a 3D extension is also proposed to better model the spanwise variation of the ice shape and porosity, as suggested by the results obtained from the permeable front technique.

REFERENCES

[1] AIAA. 1st Ice Prediction Workshop. Last accessed: 2022-01-13. [Online]. Available: https://icepredictionworkshop.wordpress.com/

[2] M. Vargas, J.-C. Tsao, and A. Rothmayer, "Review of role of icing feathers in ice accretion formation," in *2007 SAE Aircraft and Engine Icing International Conference*. SAE International, sep 2007. [Online]. Available: https://doi.org/10.4271/2007-01-3294

[3] S. Bourgault-Côté, "Ice interface evolution modelling algorithms for aircraft icing," Ph.D. dissertation, Polytechnique Montreal, Montreal, Feb. 2019.

[4] P. Lavoie, "A numerical model simulating thin water films on swept wings in icing condition," Master's thesis, Polytechnique Montréal, Apr. 2017.

[5] H. P. Laroche, S. Bourgault-Cote, and E. Laurendeau, *Multi-Layer Stochastic Ice Accretion Model for Aircraft Icing*. [Online]. Available: https://arc.aiaa.org/doi/abs/10.2514/6.2021-2629

[6] P. Trontin, G. Blanchard, A. Kontogiannis, and P. Villedieu, "Description and assessment of the new ONERA 2D icing suite IGLOO2D," in *9^{th} AIAA Atmospheric and Space Environments Conference*. AIAA Paper 2017-3417, Jun. 2017.

[7] M. Papadakis, S.-C. Wong, A. Rachman, K. E. Hung, G. T. Vu, and C. S. Bidwell, "Large and small droplet impingement data on airfoils and two simulated ice shapes," NASA, Tech. Rep., Aug. 2007. [Online]. Available: https://ntrs.nasa.gov/api/citations/20070034950/downloads/20070034950.pdf

[8] M. Schremb, "Hydrodynamics and thermodynamics of ice accretion through impact of supercooled large droplets: Experiments, simulations and theory," Ph.D. dissertation, Technischen Universität Darmstadt, Darmstadt, 2018.

[9] V. Charton, "Modélisation de l'accrétion de glace dans les turboréacteurs en condition cristaux," Ph.D. dissertation, Université de Toulouse, Toulouse, 2020.

[10] Federal Aviation Administration. Eletronic Code of Federal Regulations, Appendix C to Part 25. Last accessed: 2018-08-16. [Online]. Available: https://www.ecfr.gov/cgi-bin/text-idx?SID=bbf24e9c782b2057583037ed7c2efe26&mc=true&node=pt14.1.25&rgn=div5#ap14.1.25.0000_0nbspnbspnbsp.c

[11] ——. Eletronic Code of Federal Regulations, Appendix O to Part 25. Last accessed: 2018-08-16. [Online]. Available: https://www.ecfr.gov/cgi-bin/text-idx?SID=bbf24e9c782b2057583037ed7c2efe26&mc=true&node=pt14.1.25&rgn=div5#ap14.1.25.0000_0nbspnbspnbsp.o

[12] ——. Eletronic Code of Federal Regulations, Appendix D to Part 33. Last accessed: 2018-08-16. [Online]. Available: https://www.ecfr.gov/cgi-bin/text-idx?SID=bbf24e9c782b2057583037ed7c2efe26&mc=true&node=pt14.1.33#ap14.1.33.0000_0nbspnbspnbsp.d

[13] B. "Arizmendi, M. Morelli, G. Parma, M. Zocca, G. Quaranta, and A. Guardone, *"In-flight Icing: Modeling, Prediction, and Uncertainty"*. Cham: Springer International Publishing, 2021, pp. 455–506.

[14] M. B. Bragg, A. P. Broeren, and L. A. Blumenthal, "Iced-airfoil aerodynamics," *Progress in Aerospace Sciences*, vol. 41, no. 5, pp. 323–362, 2005.

[15] D. N. Anderson and J.-C. Tsao, "Characterization of ice roughness from simulated icing encounters," NASA, Tech. Rep., 1997.

[16] Y. Kuwata, "Direct numerical simulation of turbulent heat transfer on the reynolds analogy over irregular rough surfaces," *International Journal of Heat and Fluid Flow*, vol. 92, p. 108859, 2021. [Online]. Available: https://www.sciencedirect.com/science/article/pii/S0142727X21000898

[17] D. N. Anderson and J.-C. Tsao, "Ice shape scaling for aircraft in sld conditions," NASA, Tech. Rep., 2008. [Online]. Available: https://www.tc.faa.gov/its/worldpac/techrpt/ar0755.pdf

[18] K. Szilder and E. P. Lozowski, "Comparing experimental ice accretions on a swept wing with 3d morphogenetic simulations," *Journal of Aircraft*, vol. 0, no. 0, pp. 0–0, Jul. 2018, article in advance.

[19] M. Vargas and E. Reshotko, *Parametric experimental study of the formation of glaze ice shapes on swept wings*. [Online]. Available: https://arc.aiaa.org/doi/abs/10.2514/6.1999-94

[20] C. S. Bidwell, "Icing analysis of a swept naca 0012 wing using lewice3d version 3.48," in *6th AIAA Atmospheric and Space Environments Conference*. [Online]. Available: https://arc.aiaa.org/doi/abs/10.2514/6.2014-2200

[21] A. B. Kostinski and A. R. Jameson, "On the spatial distribution of cloud particles," *Journal of the Atmospheric Sciences*, vol. 57, no. 7, pp. 901 – 915, 2000. [Online]. Available: https://journals.ametsoc.org/view/journals/atsc/57/7/1520-0469_2000_057_0901_otsdoc_2.0.co_2.xml

[22] R. Shaw, A. Kostinski, and M. Larsen, "Towards quantifying droplet clustering in clouds," *Quarterly Journal of the Royal Meteorological Society*, vol. 128, pp. 1043 – 1057, 04 2002.

[23] M. G. Potapczuk and J.-C. Tsao, *Bimodal SLD Ice Accretion on Swept NACA 0012 Airfoil Models*. [Online]. Available: https://arc.aiaa.org/doi/abs/10.2514/6.2020-2814

[24] Y. Bourgault, W. G. Habashi, J. Dompierre, and G. S. Baruzzi, "A finite element method study of eulerian droplets impingement models," *International Journal for Numerical Methods in Fluids*, vol. 29, pp. 429–449, 1999.

[25] K. Szilder and E. P. Lozowski, "Novel two-dimensional modeling approach for aircraft icing," *Journal of Aircraft*, vol. 41, no. 4, pp. 854–861, Jul. 2004.

[26] S. E. Bansmer, *Aircraft Icing: A Challenging Problem of Fluid Mechanics*. Cuvillier Verlag, 2019.

[27] H. Beaugendre, "A PDE-based 3D approach to in-flight ice accretion," Ph.D. dissertation, McGill University, Montreal, Jun. 2003.

[28] E. Radenac, A. Kontogiannis, C. Bayeux, and P. Villedieu, "An extended rough-wall model for an integral boundary layer model intended for ice accretion calculations," in *2018 Atmospheric and Space Environments Conference*. AIAA Paper 2018-2858, Jun. 2018.

[29] E. Montreuil, A. Chazottes, D. Guffond *et al.*, "ECLIPPS: 1. three-dimensional CFD prediction of the ice accretion," in *1st AIAA Atmospheric and Space Environments Conference*. AIAA Paper 2009-3969, Jun. 2009.

[30] T. Rendall and C. Allen, "Finite-volume droplet trajectories for icing simulation," *International Journal of Multiphase Flow*, vol. 58, pp. 185–194, jan 2014.

[31] S. Bourgault-Côté and E. Laurendeau, "Two-dimensional/infinite swept wing ice accretion model," in *53rd AIAA Aerospace Sciences Meeting*. AIAA Paper 2015-535, Jan. 2015.

[32] B. Messinger, "Equilibrium temperature of an unheated icing surface as a function of airspeed," *Journal of the Aeronautical Sciences*, vol. 1, no. 20, pp. 29–42, Jan. 1953.

[33] P. Lavoie, S. Bourgault-Côté, and E. Laurendeau, "Numerical algorithms for infinite swept wing ice accretion," *Computers & Fluids*, vol. 161, pp. 189–198, Jan. 2018.

[34] C. Zhu, B. Fu, Z. Sun, and C. Zhu, "3D ice accretion simulation for complex configuration basing on improved messinger model," in *International Journal of Modern Physics: Conference Series*, vol. 19. World Scientific, Jun. 2012, pp. 341–350.

[35] T. G. Myers, "Extension to the messinger model for aircraft icing," *AIAA Journal*, vol. 39, no. 2, pp. 211–218, 2001.

[36] Y. Bourgault, H. Beaugendre, and W. G. Habashi, "Development of a shallow-water icing model in FENSAP-ICE," *Journal of Aircraft*, vol. 37, no. 4, pp. 640–646, 2000.

[37] J. Garcia Pérez, "Lattice boltzmann approach for the modeling and simulation of water droplets impact and freezing," Master's thesis, Polytechnique Montréal, Montréal, 2020.

[38] Y. Cao and M. Xin, "Numerical simulation of supercooled large droplet icing phenomenon: A review," *Archives of Computational Methods in Engineering*, 2019.

[39] K. Szilder, "Morphogenetic modelling of in-flight icing," Patent CA 2 430 823, Jun. 04, 2003. [Online]. Available: https://www.ic.gc.ca/opic-cipo/cpd/eng/patent/2430823/summary.html.

[40] K. Szilder, E. P. Lozowski, and G. Reuter, "A Study of Ice Accretion Shape on Cables Under Freezing Rain Conditions ," *Journal of Offshore Mechanics and Arctic Engineering*, vol. 124, no. 3, pp. 162–168, 08 2002. [Online]. Available: https://doi.org/10.1115/1.1488932

[41] K. Szilder and W. Yuan, "The influence of ice accretion on the aerodynamic performance of a UAS airfoil," in *53rd AIAA Aerospace Sciences Meeting*. AIAA Paper 2015-536, Jan. 2015.

[42] M. Butnarasu, W. G. Habashi, and M. Fossati, "Optimization of the morphogenetic approach for in-flight icing," in *53rd AIAA Aerospace Sciences Meeting*. Jan.: AIAA Paper 2015-34, 2015.

[43] M. Butnarasu, "An extension to the morphogenetic model for three-dimensional glaze and rime ice," Master's thesis, McGill University, Montréal, 2014.

[44] S. Bourgault-Côté, J. Docampo-Sànchez, and E. Laurendeau, "Multi-layer airfoil ice accretion simulations using a level-set method with B-Spline representation," *AIAA Journal*, no. 8, pp. 524–537, 2019.

[45] A. Leroy, "Étude expérimentale et numérique des dépôts de givre discontinus sur les voilures en flèche d'aéronefs," Ph.D. dissertation, Université Blaise Pascal, Clermont-Ferrand, Nov. 2004.

[46] S. Koshizuka, K. Shibata, M. Kondo, and T. Matsunaga. Academic Press, 2018.

[47] K. Yuki and M. Yamamoto, "Sld icing simulation on naca airfoil using mps method," in *The Proceedings of The Computational Mechanics Conference*, ser. The Computational Mechanics Conference. The Japan Society of Mechanical Engineers, Nov. 2014.

[48] D. Toba, K. Fukudome, H. Mamori, N. Fukushima, and M. Yamamoto, "Proposal of novel icing simulation using a hybrid grid- and particle-based method," *Journal of Mechanics*, vol. 36, no. 5, p. 699–706, 2020.

[49] Chapel. The Chapel Programming Language. Last accessed: 2022-02-17. [Online]. Available: https://chapel-lang.org/

[50] M. Parenteau, S. Bourgault-Cote, F. Plante, E. Kayraklioglu, and E. Laurendeau, *Development of Parallel CFD Applications with the Chapel Programming Language*. [Online]. Available: https://arc.aiaa.org/doi/abs/10.2514/6.2021-0749

[51] P. R. Spalart and S. R. Allmaras, "A one-equation turbulence model for aerodynamic flows," *Recherche Aerospatiale*, vol. 94, no. 1, pp. 5–21, 1994.

[52] ——, "A one-equation turbulence model for aerodynamic flows," in *30th Aerospace Sciences Meeting and Exhibit*. AIAA Paper 1992-439, Jan. 1992.

[53] F. R. Menter, "Improved Two-Equation k-omega Turbulence Models for Aerodynamic Flows," NASA TM 103975, Tech. Rep., Oct. 1992.

[54] P. Roe, "Approximate riemann solvers, parameter vectors, and difference schemes," *Journal of Computational Physics*, vol. 43, no. 2, pp. 357–372, 1981.

[55] J. Blazek, *Computational Fluid Dynamics: Principles and Application*, 3rd ed. Elsevier, 2015.

[56] T. J. Barth and J. D. C., "The design and application of upwind schemes on unstructured meshes," in *27th Aerospace Sciences Meeting*. AIAA Paper 1989-0366, 1989.

[57] V. Venkatakrishnan, "Convergence to steady state solutions of the euler equations on unstructured grids with limiters," *Journal of Computational Physics*, vol. 118, no. 1, 1995.

[58] D. J. Mavriplis and A. Jameson, "Multigrid solution of the Navier-Stokes equations on triangular meshes," *AIAA Journal*, vol. 28, no. 8, pp. 1415–1425, 1990.

[59] W. M. Chan, "Hyperbolic methods for surface and field grid generation," in *Handbook of Grid Generation*, 1st ed., J. F. Thompson, B. K. Soni, and N. P. Weatherill, Eds. CRC Press, 1999.

[60] R. Löhner and P. Parikh, "Generation of three-dimensional unstructured grids by the advancing-front method," *International Journal for Numerical Methods in Fluids*, vol. 8, no. 10, pp. 1135–1149, 1988. [Online]. Available: https://onlinelibrary.wiley.com/doi/abs/10.1002/fld.1650081003

[61] J. Peraire, J. Peiró, and K. Morgan, "Adaptive remeshing for three-dimensional compressible flow computations," *Journal of Computational Physics*, vol. 103, no. 2, pp. 269–285, 1992. [Online]. Available: https://www.sciencedirect.com/science/article/pii/002199919290401J

[62] H. Jin and R. I. Tanner, "Generation of unstructured tetrahedral meshes by advancing front technique," *International Journal for Numerical Methods in Engineering*, vol. 36, no. 11, pp. 1805–1823, 1993. [Online]. Available: https://onlinelibrary.wiley.com/doi/abs/10.1002/nme.1620361103

[63] Helene Papillon Laroche and Simon Bourgault-Cote and Eric Laurendeau. Development of an Aircraft Aero-Icing Suite Using ChapelProgramming Language. Last accessed: 2022-01-24. [Online]. Available: https://casi.ca/resources/Documents/AERO/2021/Full%20Papers/Development%20of%20an%20Aircraft%20Aero-Icing%20Suite%20Using%20Chapel.pdf

[64] W. H. "Press, S. A. Teukolsky, W. T. Vetterling, and B. P. Flannery. Cambridge University Press, 2007.

[65] P. J. SCHNEIDER and D. H. EBERLY, "Chapter 7 - intersection in 2d," in *Geometric Tools for Computer Graphics*, ser. The Morgan Kaufmann Series in Computer Graphics, P. J. SCHNEIDER and D. H. EBERLY, Eds. San Francisco: Morgan Kaufmann, 2003, pp. 241–284. [Online]. Available: https://www.sciencedirect.com/science/article/pii/B9781558605947500102

[66] T. Erhan, C. Murat, and O. Serkan, "Parallel computing applied to three-dimensional droplet trajectory simulation in lagrangian approach," in *SAE 2011 International Conference on Aircraft and Engine Icing and Ground Deicing*. SAE International, jun 2011. [Online]. Available: https://doi.org/10.4271/2011-38-0106

[67] M. Sugiyama, "Chapter 19 - numerical approximation of predictive distribution," in *Introduction to Statistical Machine Learning*, M. Sugiyama, Ed. Boston: Morgan Kaufmann, 2016, pp. 205–220. [Online]. Available: https://www.sciencedirect.com/science/article/pii/B9780128021217000303

[68] M. E. O'Neill, "Pcg : A family of simple fast space-efficient statistically good algorithms for random number generation," 2014.

[69] I. Tecplot. Tecplot. Last accessed: 2022-02-17. [Online]. Available: https://www.tecplot.com/

APPENDIX A EXPERIMENTAL DROPLET SIZE DISTRIBUTION

This appendix contains the experimental droplet size distributions used for the computations of cases 241 and 364.

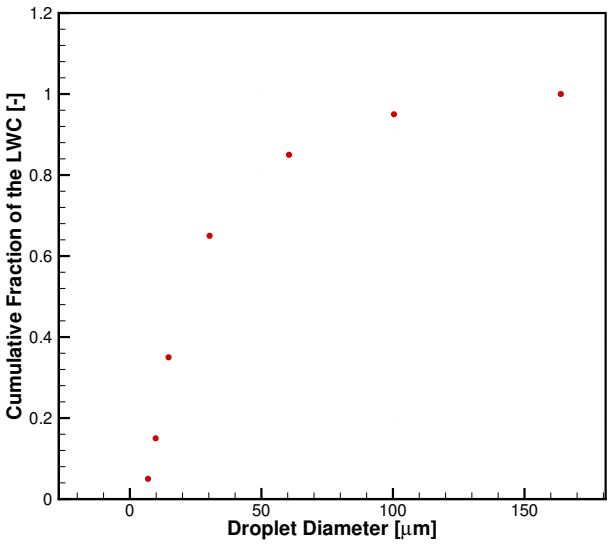

Figure A.1 Experimental droplet size distribution for case 241 [1]

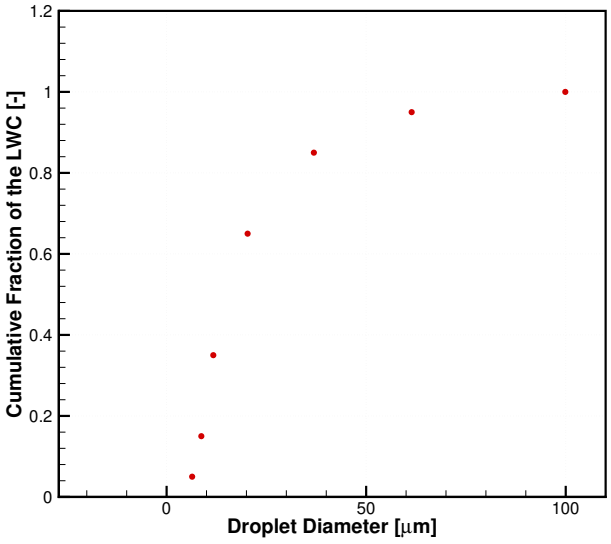

Figure A.2 Experimental droplet size distribution for case 364 [1]